Electromechanical Coupling of Graphene With Cells

by

Ravindra Kempaiah

A thesis

presented to the University of Waterloo

in fulfillment of the

thesis requirement for the degree of

Master of Science

in

Chemistry - Nanotechnology

Waterloo, Ontario, Canada, 2011

Author's Declaration

I hereby declare that I am the sole author of this thesis. This is a true copy of the thesis, including any required final revisions, as accepted by my examiners.

I understand that my thesis may be made electronically available to the public.

Ravindra Kempaiah

Abstract

Nanomaterials have been studied extensively in the last decade in the context of many applications such as polymer composites, energy harvesting systems, sensors, 'transparent'-like materials, field-effect transistors (FETs), spintronic devices, gas sensors and biomedical applications. Graphene, a recently discovered two-dimensional form of carbon has captured the interest of material scientists, and physicists alike due to its excellent electrical, mechanical and thermal properties. Graphene has also kindled a tremendous interest among chemists and cell biologists to create cellular-electronic interface in the context of bio-electronic devices as it can enable fabricating devices with enhanced potential as compared to conventional bio-electronics. Graphene's unique electronic properties and sizes comparable with biological structures involved in cellular communication makes it a promising nanostructure for establishing active interfaces with biological systems. In the recent past Field effect transistors (FETs) have been successfully fabricated using carbon nanotubes (CNTs) and nanowires (NWs) and electrical characterization of these FETs were done by interfacing them with various cell cultures, tissues and muscle cells. In these cases, exceptionally high surface area to thickness ratio of FETs provides high percentage of collectible signals and the cells that are used for the study are typically placed on the FET. In this thesis, we examine a different approach towards forming bio-electronic interfaces by covering the graphene oxide (reduced) sheets on the yeast cells. Graphene oxide and reduced graphene oxide sheets as two-dimensional electronic materials have very high charge carrier mobility, extremely high surface area to thickness ratio, mechanical modulus and elasticity. We report the synthesis of graphene oxide using wet chemistry method, reduction of graphene oxide using different reducing agents and electrical characterization of graphene oxide's conductivity. Micro-meter sized graphene sheets are used to encapsulate the yeast cells with the aid of calcium and gold nanoparticle chains. We also demonstrate that graphene sheets form electrically conductive layers on the yeast cells and developing an electromechanical coupling with the cell. The mechanical and electrical characteristics of graphene sheets are highly dependent on the cell volume and structure which are in turn related to the environment around the cell. Furthermore, using the same principle of electromechanical coupling we study the dynamics of cell surface stresses and cell volume modification, which are of importance in processes such as cell growth, division, and response to physiological factors such as osmotic stresses.

iii

Acknowledgements

I am honored by the fact that I have been a member and research student at the University of Waterloo for the past two years. I am immensely benefitted by the research expertise that abounds the reputed labs of this university.

As I move forward in my academic career, I would like to thank a few people who have played a pivotal role in my research so far and have helped me shape this thesis:

Prof. Dr. Vivek Maheshwari, my supervisor, for accepting me into his research group, the support and responsibility of my Master's thesis and for giving me orientation in experimental research by devoting his time and resources. I am inspired by his focused and meticulous work.

Prof. Dr. Tong Leung, my committee advisor, for guiding me through this work, for allowing me to work in his lab even after the office hours and for giving me an opportunity to learn FESEM, AFM and Raman spectroscopy.

Prof. Dr. Juewen Liu, my committee advisor, for proofreading my work and always encouraging me. Dr Liu has been a very inspiring person and I have immensely benefitted by collaboration with his research team.

My fellow lab mates Shehan Salgado, Alfred Chung, Jinlong Fu and Long Pu for their assistance in the lab and fruitful discussions leading to successful experimental results.

Contents

List of Figures

viii

ix

List of Equations

List of Tables

List of Abbreviations

AFM: Atomic force microscopy.

APTES: (3-Aminopropyl) Triethoxysilane.

Au-chip: Gold patterned electrodes on silicon chip

Ca-Au: Calcium - Gold nanoparticle system.

Ca-Au-GO: Calcium–Gold–graphene oxide system.

CNT: Carbon nanotubes.

CVD: Chemical vapor deposition.

FESEM: Field emission scanning electron microscopy.

FET: Field effect transistor.

GNR: Graphene nano ribbons.

GNS: Graphene nano sheets.

GO: Graphene oxide.

HPG: Highly oriented pyrolytic graphite.

HRGO: Hydrazine reduced graphene oxide.

PAH: Poly (allylamine hydrochloride).

NEMS: Nanoelectromechanical systems.

NW: Nanowires.

RGO: Reduced graphene oxide.

SaC: Saccharomyces cerevisiae's (Yeast cell)

UV-Vis: Ultraviolet-visible spectroscopy

VRH: Variable range hopping.

YPD: Yeast-peptone-dextrose.

2-D, 3-D: Two dimensional, three dimensional.

Chapter 1

Introduction

Carbon is one of the fundamental building blocks of life on this planet. Carbon is found in both pure and alloyed forms. Pure form of carbon exhibits allotropic nature i.e., diamond and graphite are two forms that are very different in terms of properties even though they only differ by the arrangement of atoms. While diamond is insulating and very hard, graphite is conducting and is a lubricant. In 1985 the first artificial pure carbon material, the spherical molecule called "fullerene", was found, since then an intense research on other pure carbon materials began. In 1991, carbon was produced in the form of quasi one-dimensional nanotubes. Later, in 2004, a single sheet of carbon, named graphene was experimentally discovered. [1] The strictly two-dimensional graphene can be seen as the basic building block for the other graphite materials, having different dimensionalities. The fullerenes can be seen as zero-dimensional wrapped up graphene, the nanotubes as one-dimensional rolled graphene, and graphite as three-dimensional stacked graphene (see Figure 1-1).

Fullerenes (C_{60})
0D - 1985

Carbon Nanotubes
1D - 1991

Graphene
2D - 2004

Graphite
3D
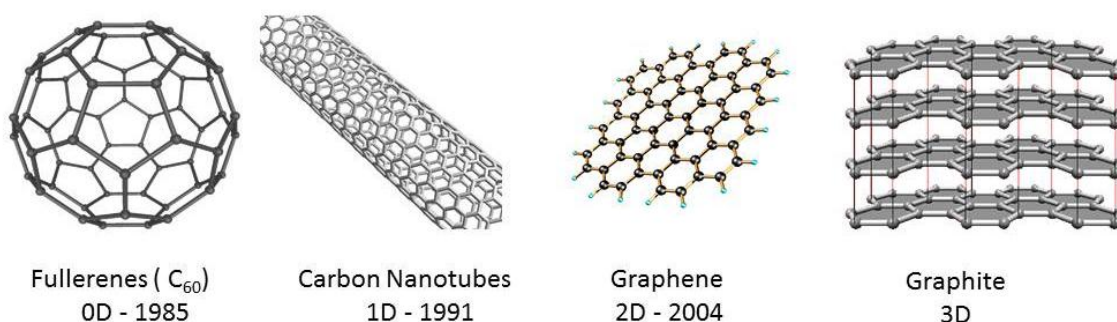
Figure 1-1 : Forms of pure carbon and the year of invention. (Courtesy: http://nanohub.org/)

Graphene, which was recently discovered in the year 2004 and known as "The thinnest material in our universe" is a single-atom-thick sheet (2-dimensional) of hexagonally arrayed, sp2-hybridized carbon atoms (see Figure 1-2). It is one of the most exciting materials for the present-day researchers in the fields of materials science and condensed matter physics. Graphene provides a lot more interesting physics in addition to being a purely two-dimensional crystal of only one atomic layer thickness. With versatile adaptability to implement it in practical applications, graphene science is set to progress at a relentless pace over the next few years.

Geim et al., who have been awarded the Nobel Prize in physics for their discovery of graphene describes the phenomenon of graphene as follows,

> **"Wonder material of the 21st century - it is a zero band gap semiconductor with high intrinsic mobility. Graphene can endure current densities five orders of magnitude higher than silver. Graphene is chemically inert and has a harmony between its brittleness and ductility. Electron transport in graphene is quite unique and is described by Dirac like equation for relativistic particles rather than Schrödinger equation. The strange electronic behavior allows the study of relativistic quantum phenomena at room temperatures."[2]**
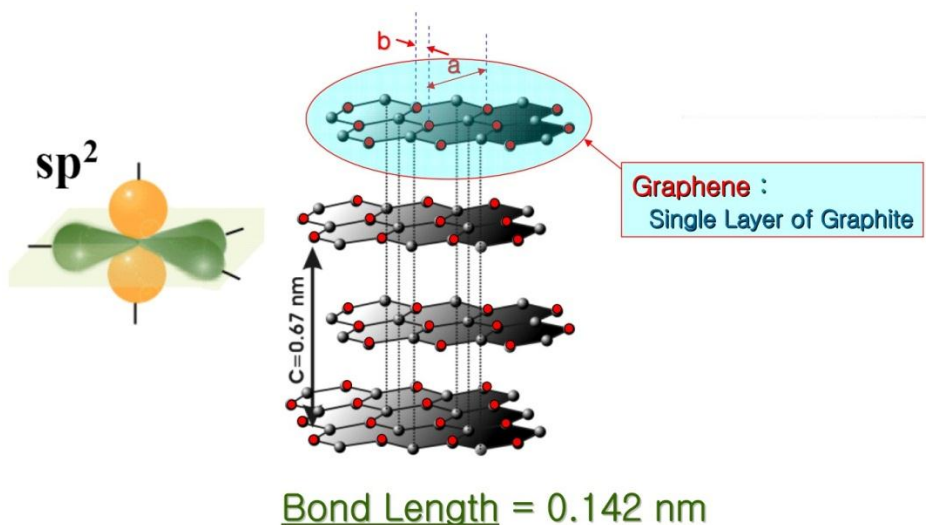
Figure 1-2: Hexagonal array of sp^2 carbon in graphene.

The research conducted here at the Department of Chemistry and the Waterloo Institute for Nanotechnology (WIN), University of Waterloo is aimed at exploring the feasibility of using graphene as a possible nano-electronic interface material for creating sensing devices. We have explored different chemical exfoliation methods for the synthesis of graphene oxide (GO), reduction of graphene oxide (RGO) using various reducing agents like hydrazine (N_2H_4), Sodium borohydride ($NaBH_4$), and glucose ($C_6H_{12}O_6$). Characterization of graphene oxide's electrical properties was done after depositing them on a specially patterned electrode. Yeast cells were used as the biological interface to achieve electromechanical coupling.

Introduction

We delve into the following aspects of graphene in the succeeding chapters: Structure, physics, synthesis methods, reduction methods, electronic transport, mechanical properties, electromechanical coupling and intended application in our research project.

In chapter 2, we will provide a brief description of the lattice structure of two-dimensional graphene, followed by electronic band structure of graphene and charge carrier transport phenomenon. We also mention the modifications in structure when different synthesis routes are used. Chapter 3 elucidates the chemical experimental methods and characterization of GO or RGO. Producing experimental samples of nanometer-scale thick samples and coupling it with live cells is an extremely delicate process and we discuss the critical interpretation of the system and its behavior. In chapter 4, we discuss the electromechanical coupling in detail and provide the results from FESEM, AFM, Raman spectroscopy, TEM and live/dead tests employed for the examination of electromechanical coupling with cells. Conclusions are summarized in chapter 5.

Chapter 2

Fundamentals of Graphene

Pure graphitic forms of carbon (CNT, graphite) were known to scientists for a long time and hence researchers had theoretically deduced the possibility of pure two-dimensional material i.e., graphene even though it was only discovered in 2004. However, for a long time it was assumed that graphene in the free- state can never be found in nature. The thermodynamic stability of 2-D graphene was thought of to be an uncertainty and this assumption was augmented by Landau and Peierls.[3] The thermodynamic stability of 2-D crystals was assumed to be poor because of thermal fluctuations that were comparable to interatomic distances in magnitude at any finite temperature. In 2004, Geim et al. not only synthesized a free standing 2-D graphene sheet they also found that it is a continuous sheet with a high degree of crystal quality.[4]

2.1 Carbon Atom Electronic Configuration

Graphene is made of carbon atoms; each carbon atom has six electrons with an electronic configuration of $1s^2$, $2s^2$ and $2p^2$. Electrons in the $1s^2$ orbital are strongly bonded and form the core group of electrons while the other 4 electrons form the valence group of electrons that are delocalized in orbitals. Electrons in $2s^2$ and $2p^2$ orbitals undergo hybridization wherein the wavefunction of these electrons undergo amalgamation to give rise to more stable structure (see Figure 2-1). Per each atom, the orbitals (sp2) represented in green are called σ (Sigma) and they lie in XY-plane forming an angle of 120° with each other and form covalent bonds with the neighboring atoms to form hexagonal lattice structure of graphene. The orbitals (p_z) in blue along the Z-direction are called π (pi) orbitals and they are responsible for hosting the mobile carriers in the XY-plane of the lattice. Electrons in the π state are weakly bonded and they can easily hop around the neighboring atoms in the XY-plane making it crucial for the transport properties; this fact was established by the fact that electrons in graphene move ballistically over thousands of interatomic distances without scattering.[2] When a huge number of sp^2 hybridized carbon atoms come together to form an hexagonal lattice as in the case of graphene, their wave functions merge to form a normalized band structure.[5]
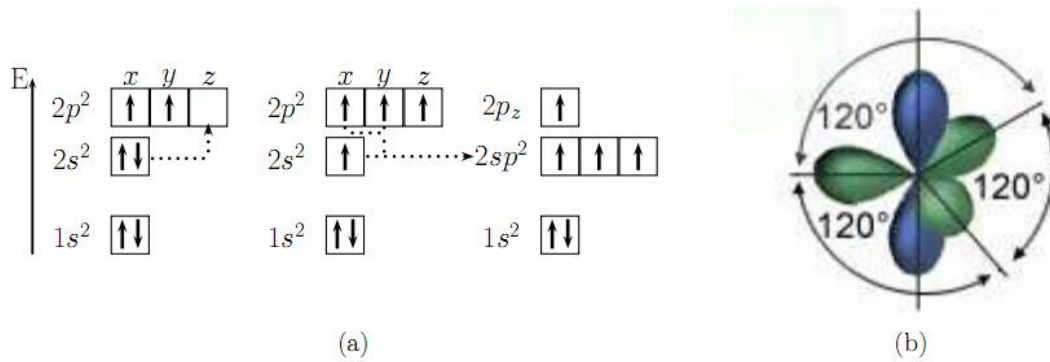
Figure 2-1: sp² hybridization in graphene. (a) Occupation of atomic orbitals in the hybridization process. (b) Orbital structure after the hybridization.

2.2 Hexagonal Lattice and Brillouin Zone

Carbon atoms in graphene occupy the regular hexagon edge points and this structure is often referred to as the "Honeycomb lattice". Honeycomb lattice cannot be constructed by the repetition of any of the Bravais lattices, therefore from the crystallographic point of view it has to be constructed using a rhomboid shaped Bravais lattice with two-atom (atoms A and B) basis.[6] The lattice can be described using two basis vectors a_1 and a_2 (see Figure 2-2). In terms of Cartesian coordinate system these two vectors are given by,

$$a_1 = \sqrt{3}a\, e_x \text{ and } a_2 = \frac{\sqrt{3}}{2}ae_x + \frac{3}{2}a\, e_y$$

Equation 2-1

In Figure 2-2, a=1.42 Å is the interatomic distance of carbon atoms in the graphene layer, the lattice constant $a_o = \sqrt{3}\, a = 2.46$ Å, while e_x and e_y are the unit vectors. The reciprocal lattice is shown in Figure 2-2 (b) and given by

$$b_1 = \frac{2\pi}{\sqrt{3}a}\left(e_x - \frac{1}{\sqrt{3}}e_y\right) \text{ and } b_2 = \frac{4\pi}{3a}e_y$$

Equation 2-2

The reciprocal space shown in Figure 2-2 (b) has a basic Brillouin zone with six edges out of which two are inequivalent that are called Dirac points (K and K'). (Courtesy: Petra Dietl, University of Karlsruhe)

5
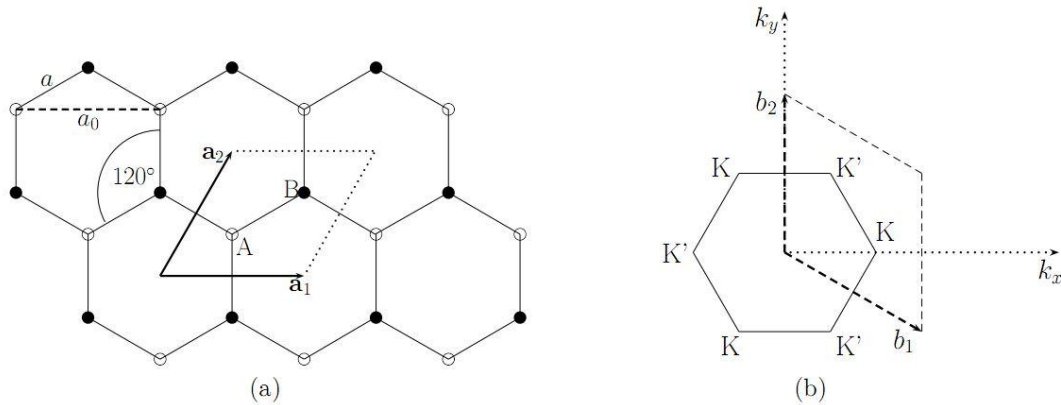
Figure 2-2: (a) lattice structure of graphene in real space, (b) Brillouin zone in reciprocal space.

2.3 Band Structure

Graphene is different from most conventional three-dimensional materials. Intrinsic graphene is a semi-metal or zero-gap semiconductor. Its uniqueness lies in the electronic structure which gives rise to an unconventional band gap and causes the charge carriers to behave like relativistic particles. It was realized early on that the energy-momentum relation (E-k) is linear for low energies near the six corners of the two-dimensional hexagonal Brillouin zone, leading to zero effective mass for electrons and holes. Due to this linear (or "conical") dispersion relation at low energies, electrons and holes near these six points, two of which are inequivalent, behave like relativistic particles described by the Dirac equation (Equation 2-3) for spin 1/2 particles. Hence, the electrons and holes are called Dirac fermions, and the six corners of the Brillouin zone are called the Dirac points.[7, 8]

The unbound valence electrons that exist in P_z orbitals in hexagonal lattice develop into delocalized π and π^* states that form the highest occupied valence band and lowest unoccupied conduction band. The π and π^* states of graphene degenerate at the corner (K point) of the hexagonal Brillouin zone. This degeneracy occurs at the so-called Dirac crossing energy (E_D), which at the normal half-filling condition coincide with the Fermi energy level (E_F). The hybridized electrons interact with the periodic field of the hexagonal crystal lattice and form Dirac fermions, described by cone-like energy bands.[9]
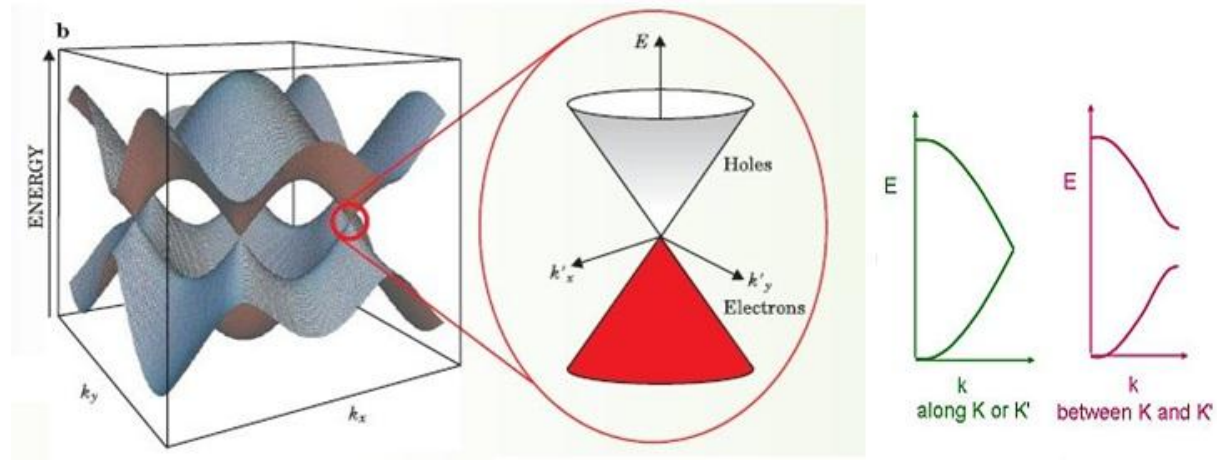
Figure 2-3: Band structure between and at Dirac points

$$i\hbar \frac{\partial \Psi}{\partial t} = \frac{\hbar c}{i}\left(\alpha_1 \frac{\partial \Psi}{\partial x^1} + \alpha_2 \frac{\partial \Psi}{\partial x^2} + \alpha_3 \frac{\partial \Psi}{\partial x^3}\right) + \alpha_4 mc^2 \Psi$$

Equation 2-3: Dirac equation for relativistic particles

In the Equation 2-3, $\hbar = h/2\pi$ is the reduced Planck constant, c= speed of light, m= mass of the particle, α_i are the Dirac matrices (Hermitian), Ψ is the four component wavefunction. The charge carriers in graphene are governed by an equation which is analogous to 2-D Dirac equation and they behave like massless relativistic particles and travel with a Fermi velocity $V_F \approx 1{\times}10^6$ m/s. In the Figure 2-4 $\vec{\sigma}$ is the Pauli matrix and $\hat{p}$ is the momentum operator.

As the number of layers in graphene increases, the electronic structure becomes increasingly complex. Under normal circumstances the purity of a graphene sheet is highly dependent on the synthesis route and the doping concentration. The optical absorbance of graphene has been measured at 2.3% making it invisible for naked eye.[10] One of the most important steps towards isolating single layer graphene was finding a way to spot atomically thin carbon sheet. A.K Geim's team at the University of Manchester made use of interference effect at a specially chosen thickness (300 nm) of SiO2 on Si substrate to enhance the optical contrast under white light illumination and imaged it using an optical microscope.[11] Figure 2-5 (a) shows an image of layers of graphene oxide deposited on a gold patterned chip, (b) is the image of mechanically exfoliated graphene layer on a Silicon substrate. (Courtesy: A K Geim group, University of Manchester).

7
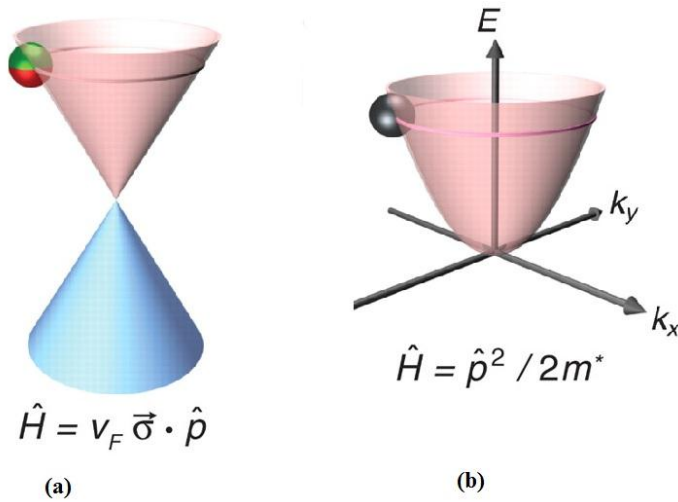
Figure 2-4: (a) Massless Dirac fermions in graphene, (b) Schrödinger equation for Quasi-particles with effective mass m*.

Electrons propagating through honeycomb lattice completely lose their effective mass making them behave like Dirac-fermions and these electron waves travel within a layer that is only one atom thick making them highly sensitive and receptive to scanning probes like STM.[12]
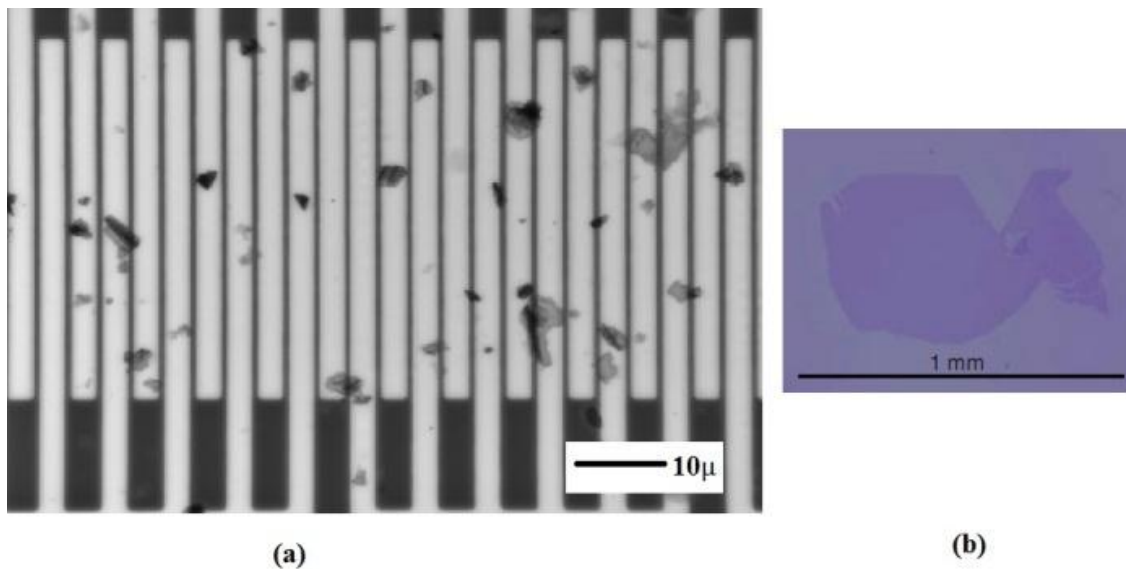
Figure 2-5: Graphene oxide / graphene imaged using optical microscope.

8

Graphene being a derivative of graphite exhibits a very high degree of crystalline nature. Pure graphene is rare to be found in nature and it is a poly crystalline material under typical conditions. Experimental studies involve synthesis of graphene using methods like chemical vapor deposition (CVD) that involve materials like methane (CH4).[13] Mechanical exfoliation e.g., scotch-tape method produces high quality graphene but is limited by size and the labor intensive nature of the process. Most of the chemical methods except CVD produces oxidized form of graphene i.e., graphene oxide (GO) and in our project we used GO and reduced graphene oxide (RGO) for the purpose of coupling it with cells.

Synthesis methods like CVD or mechanical exfoliation has limitations when it comes to maintaining the final product thickness, solubility in water (graphene is hydrophobic) and purity. Chemically derived graphene generally has attached carboxylic or phenolic groups, which not only makes the graphene sheet to carry a net negative charge making it solution friendly, but also increase the band gap in the electronic structure of graphene.[14,15] Figure 2-6 (a) shows the atomic structure of graphene single layer as imaged using STM, (b) shows the STM image of graphene oxide (GO) monolayer deposited on a HOPG substrate, taken under ambient conditions and oxidized regions are marked by green colors.[16]
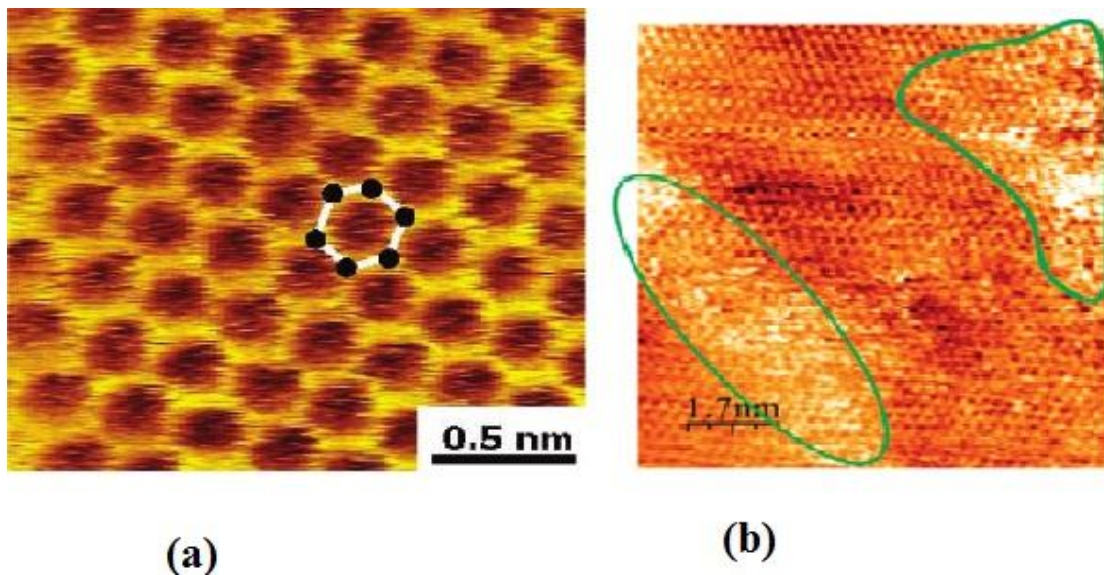
Figure 2-6: STM images (a) graphene monolayer, (b) graphene oxide.

Chemical exfoliation of graphite involves severe oxidation of graphite flakes using strong oxidizing agents to reduce the bulk to few layers and then finally to single layer graphene oxide. Graphite contains localized defects in its π-structure that may serve as the seed for oxidation.[8, 16]

2.4 Structure of Graphene Oxide

There has not been a single comprehensive model for the structure of graphene so far and the reason can be attributed to the complexity of the material i.e., amorphous, nonstoichiometric atomic composition and sample-to-sample variability. Considerable amount of work has been done to decipher the structure of graphene oxide and many models have been proposed to account for the many reactive functional groups found in graphene oxide. Majority of the earlier models i.e., Hofmann, Ruess, Scholz – Boehm and Nakajima – Matuso (Figure 2-7) were based on the premise that GO is made of regular lattice structure joined in a discreet way with functional groups forming the bridges.[18, 19]

Hofmann   **Ruess**

Scholz - Boehm   **Nakajima-Matsuo**
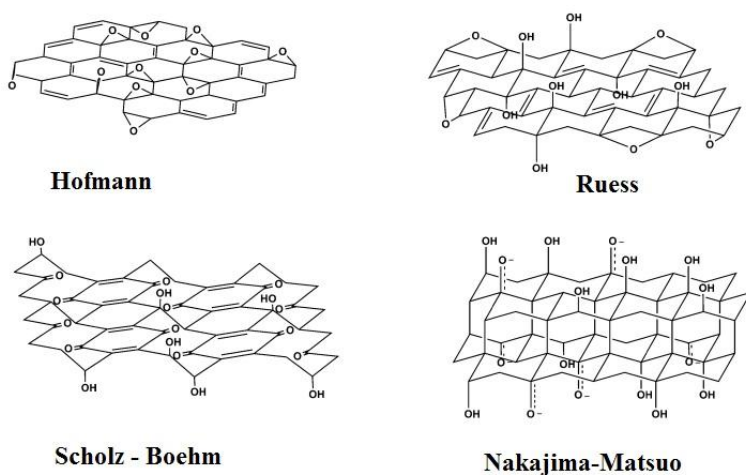
Figure 2-7: Attempted models of GO.[18]

In spite of the short-comings of these models to describe the structure of GO, they had one thing in common i.e., a strong C-C bond through the sp^2 hybridization in the form of cyclohexane / cyclohexyl network. The position of epoxy groups, carboxyl group (COOH) and hydroxyl group was not established. In the recent times, the most widely cited and well-known model is Lerf-Klinowski model.[20] Earlier models of GO relied mainly on the elemental composition and the X-ray diffraction studies, whereas Lerf et al., employed a series of GO derivatives that have different reactivity and conducted solid state nuclear magnetic resonance (NMR). As a result of this study, Lerf and Klinowski model underwent further

refinement to incorporate the observed nature of conjugated double bonds and they also established that carboxylic acid groups are mainly present in very small quantities at the edges of the basal plane. Epoxy groups are found to be in the middle of the sheets with hydroxyl groups. The hydrophilic nature of GO depends on the polarity of the surface and the extent of functionalization imparted during oxidation. Dispersability of GO in water is a very crucial criterion for the further processing of GO with other nanomaterials or composites, towards this direction Lerf and Klinowski proposed a model (Figure 2-8) for the binding of water molecules with GO.[20,21]

Lerf-Klinowski model for GO

(a)

H2 bonding between
GO and H2O molecules

(b)
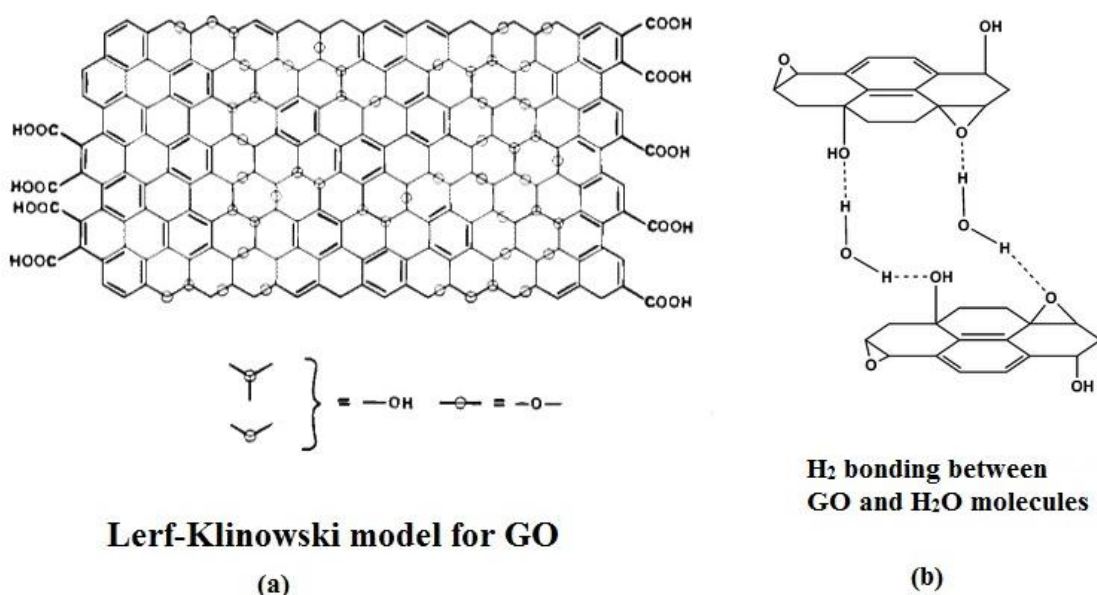
Figure 2-8: (a) Lerf-Klinowski model for GO, (b) Interaction of GO and H₂O

2.5 Mechanical and Thermal Properties

GO or graphene sheets have Young's moduli that can rival specialized class of steels (~1.0 TPa). The enhanced flexibility of graphene sheets despite their high Young's modulus has been attributed to the change in curvature given by reversible elongation of sp² C-C bonds. Single layer graphene is reported to have Young's modulus in the range 0.694-0.714 TPa and with a Poisson's ratio of 0.149. Combination of graphene's electrical conductivity, mechanical strength can lead to graphene based strain sensors.[22] Graphene is particularly promising as a thermal management material because its superior thermal conductivity is supplemented by plane geometry and effective yet tunable integration with silicon. Thermal conductivity of graphene can reach up to 5500 $W/(m*K)$ enabling it to be an ideal candidate

for super capacitors, interconnects, cloaking surfaces and field emitters. Carbon nanotubes have a typical thermal conductivity range of 3000 to 3500 $W/(m*K)$. Diamond, another form of carbon, comes in between 1000 and 2200$W/(m*K)$.[23] The single-layer graphene studied by the researchers at the University of California displayed a thermal conductivity as high as 5300 $W/(m*K)$ near room temperature.[24] Graphene oxide on the other hand will differ in these values as it contains defects (hetero-atomic), localized structural artifacts and dislocations that shape the grain boundaries in the polycrystalline lattice of GO or graphene. We tabulate the general physical properties of graphene in Table 1.

Table 1: Properties of Graphene

Parameter	Value	Observations
Mobility	40,000 cm^2 V^{-1} s^{-1}	Intrinsic mobility 200,000 cm^2 V^{-1} s^{-1} (RT)
Mean free path (ballistic transport)	›400 nm	At room temperature
Fermi Velocity	c/300 = 1,000,000 m/s	At room temperature
Electron effective mass	0.06 m$_e$	At room temperature
Hole effective mass	0.03 m$_e$	At room temperature
Thermal Conductivity	5000 $W/(m*K)$	Better conductivity than in most crystals
Young Modulus (Graphene) Young Modulus (GO)	Max 1.05 TPa Max 0.25 TPa	Ten times greater than steel

Graphene sheets have been used for making fluid-based sensor for detection of pH, DNA hybridization and antibody-antigen binding.[25] Graphene has been found to be an ideal material for green energy and has been employed in Li-ion batteries; it is also successfully used in capacitors.[26] One of the biggest uses of graphene has been in flexible electronics that can use very thin, semi-transparent, low resistance and high optical transmittance sheets. Recently, 30-inch ultra-thin roll-to-roll production of graphene has been accomplished.[27]

Chapter 3
Synthesis and Characterization

Graphene was chosen to be used as an electronic interface for the electromechanical coupling with the yeast cells, so it was necessary to produce solution friendly graphene. We decided to prepare graphene oxide as it is very solution friendly, stable and is amenable for further processing with other nano particles. Graphene produced by other methods like CVD or exfoliation may have high crystalline nature but it is hydrophobic and will be expensive to prepare on a day-to-day basis. We decided to synthesize GO using modified Hummers method (wet chemistry method), characterize it for electrical conduction and then proceed with the reduction of GO for further processes.[28] Mechanical exfoliation of 3-D graphite renders it in the form of layers and if it is pushed to its limit then we get single layer graphene (SLG). Here, instead of using mechanical means we are using rigorous oxidation process to exfoliate the layers of graphite to form solution dispersible few layer graphene (FLG) or SLG.[29]

3.1 Synthesis of Graphene Oxide

The chemical oxidation of graphite to form GO was done in two steps, the first step is (1) pre-oxidation of graphite and the second step (2) is the oxidation of pre-oxidized graphite to GO followed by osmotic dialysis and filtration.

3.1.1 Pre-oxidation of Graphite

Graphene oxide was synthesized via the modified Hummers method. Graphite flakes (~ 325 mesh size, Alfa Aesar) were oxidized using a combination of powerful reagents i.e., concentrated sulphuric acid (H_2SO_4), potassium per sulphate ($K_2S_2O_8$), phosphorous pentoxide (P_2O_5). 3 grams of graphite flakes were first dissolved in 50 mL of H_2SO_4 in a glass beaker; oxidizing agents $K_2S_2O_8$ and P_2O_5 were added to the mixture of graphite and sulphuric acid and stirred at 90℃ on a hot plate till the flakes were completely dissolved. The stirring continued for 4 more hours at 80℃ and the solution was then diluted with 500 mL of Milli-Q Millipore™ water (Ultrapure water > 16MΩ). After the dilution, the solution was stirred overnight, filtered, washed with de-ionized (DI) water and then dried to get the powdered form of pre-oxidized graphene oxide.[29, 30]

3.1.2 Final Oxidation and Osmotic Dialysis

Pre-oxidized GO powder was then subjected to further oxidation with 125 mL of H_2SO_4 and 15 g of Potassium permanganate ($KMnO_4$) in an ice bath where the solution was stirred for 2 more hours. 130 mL of Milli-Q Millipore™ water was added to the mixture and this caused the temperature to rise to 95℃. After 15 minutes, 15 mL of hydrogen peroxide (H_2O_2) was added to reduce the manganese in the solution to manganese sulphate (Mn→MnSO4) and this makes the solution to turn bright yellow from dark brown color. Finally, the solution was diluted with 400 mL of Milli-Q Millipore™ water and resultant yellow suspension was stirred overnight. The mixture was filtered and washed with 1:10 HCl aqueous solution (1L) to remove metal ions followed by 1L of DI water to remove the acid. The resulting solid was dried in air and diluted to make a GO dispersion (2% w/w). Finally, it was purified by dialysis for one week to remove the remaining metal species. GO was filtered and washed till the rinsed water pH was found to be approximately 7.[17, 31]

(a)   (b)   (c)
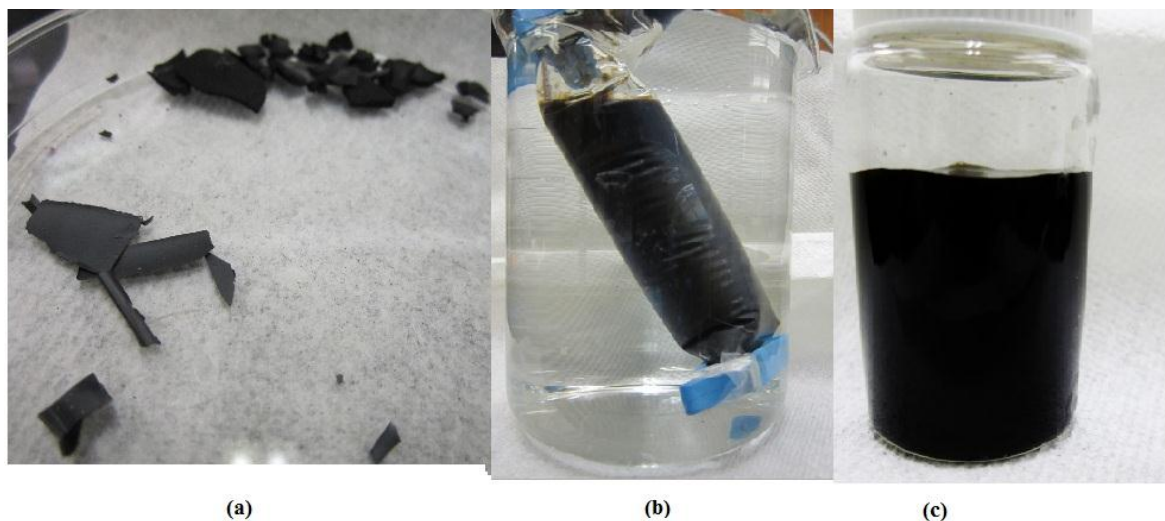
Figure 3-1: Stages of GO synthesis.

Figure 3-1: (a) Dried flakes of GO; (b) Dried powder was then dissolved in Milli-Q Millipore™ water (2% w/w) and made to undergo reverse osmosis in a molecular-porous membrane tubing which is encased in a water filled container. The difference in the ionic concentration within the membrane as compared to the outer surface creates a diffusion gradient and drives the ions to seep through the membrane pores thereby neutralizing the GO dispersion; (c) 2% GO dispersion was sonicated for 30 minutes to ensure that particles do not agglomerate to form aggregates, centrifuged for 3 minutes at 500

rpm and the resultant suspension was found to be stable for several months. Even though we follow the modified Hummers process, we must note that variations in the degree of oxidation caused by differences in starting materials (principally the graphite source) or oxidation protocol can cause substantial variation in the structure and properties of GO.[32] The distribution of oxide functional groups on the surface of GO is strongly dependent on the coverage. The ratio of epoxides to alcohols indicates the degree of oxidation. The dispersibility of GO depends on the degree of oxidation, polarity of the surface functional groups as a result of oxidation and the solvent. Extensive oxidation results in well polarized surface and it is found that sonication helps near-complete exfoliation of the dispersed GO platelets.[18]

Once GO was synthesized, it was important to study its properties before coupling it with cells. To study the electrical conduction of the synthesized GO sheets, its physical dimension, regularity and distribution of the sheets, it was necessary to deposit the GO on a substrate. The electrical conduction i.e., the phonon gas transport in the lattice is strongly influenced by the interaction between the GO and the substrate on which it is deposited. On an oxygen rich substrate, it behaves as semiconducting while on the hydrogen rich substrate, it behaves like a metallic sheet. Initially microscope slides were used for quick verification of the efficiency of deposition.[33] For electrical measurements, a custom designed Gold-Silicon chip was used. The chips had a SiO_2 layer of thickness 200 nm on top of which the gold electrodes were patterned (see Appendix A).

3.1.3 Surface Functionalization

Surface functionalization of the Au-electrode chips was found to play a vital role in the adhesion of GO sheets on the electrode pads. For this purpose, Silicon chips patterned with gold electrodes were washed with 2-propanol and Milli-Q Millipore™ water and subsequently sonicated in 50:50 by volume solution of 2-propanol and Milli-Q Millipore™ water to remove any residual particles on the surface. Their surface was then hydroxylated by placing them in "piranha" solution (7:3 concentrated H_2SO_4: 30% H_2O_2) (CAUTION: piranha solution reacts violently with organic compounds!). This treatment ensured the elimination of excess organic compounds and induced hydrophilic nature on the surface of the chips. To remove any excess piranha solution, the chips were mildly washed with Millipore™ water. Thus treated chips were placed in a container having surface primer (PAH / APTES) for 10 minutes and then taken out, washed with Millipore™ water and then used for the purpose of deposition.[34]

15

3.1.4 Deposition of GO on PAH Treated Chip

To find the right kind of surface primer for surface functionalization was very important, thus PAH was initially tested as a potential surface primer. Microscopic slides were washed according the procedure mentioned above, surface-functionalized with PAH and then GO was deposited by the process of adsorption (Figure 3-2).

Deposition of GO on a glass slide functionalized with PAH. Mag : 40 x, Optical Microscope.	Chemical structure of PAH
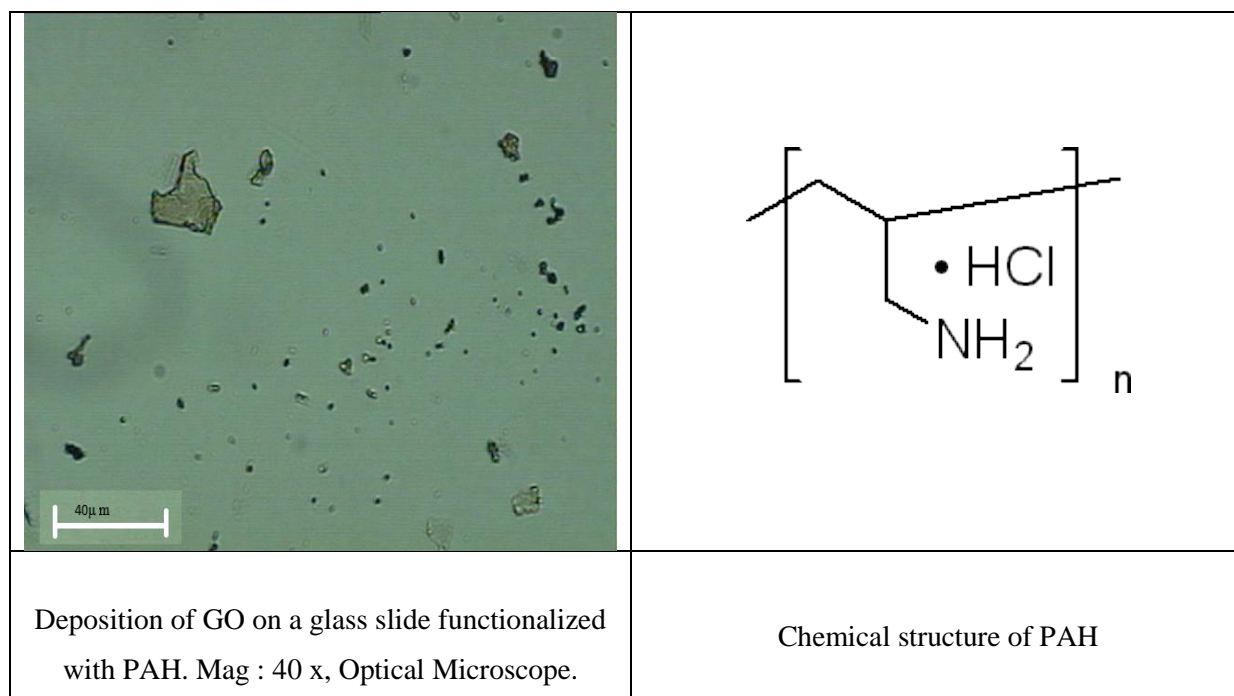
Figure 3-2: GO sheets on a PAH treated chip.

3.1.5 Deposition of GO on APTES Treated Chip

Next, (3- Aminopropyl)triethoxysilane (APTES) was tested as a surface primer for the deposition of GO. A 10 mL solution containing 100 μL of APTES was used as the standard for chip functionalization. The procedure for using the APTES was the same as that of PAH except that chips were annealed at 120°C after the adsorption in the APTES solution for 30 minutes (Figure 3-3). We found that annealing the slides/chips for 30 minutes enhanced the adhesion of GO and eliminated the unwanted presence of moisture or other organic molecules. The surface prepared in this manner is highly hydrophobic.[35]
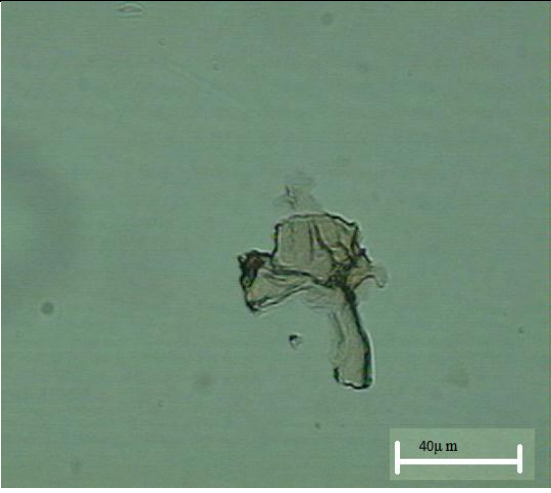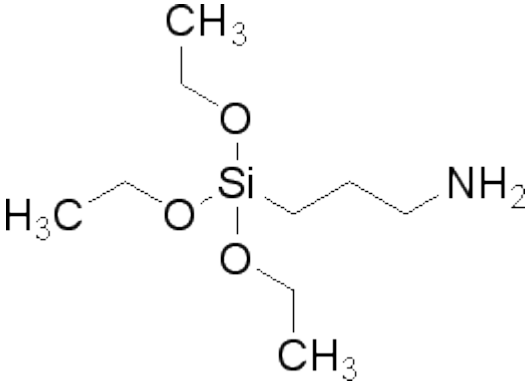
Deposition of GO on a microscopic slide treated with APTES. Mag : 40 x, Optical Microscope.	Chemical structure of (3-Aminopropyl)triethoxysilane

Figure 3-3: GO sheets on an APTES treated chip.

The method that employs APTES shows deposition of bigger graphene sheets and it is evident that there are wrinkles on the GO sheet. The darker regions of the sheet represent sections in which the graphene is not one-atom thick/monolayer. The larger single layer sheet of graphene is important when depositing graphene onto the patterned electrode chips. The reason is that in order to analyze the electrical and thermal properties of graphene, the graphene sheet must be large enough to fill the gaps between the electrode padding on the chip.[29, 36]

3.1.6 GO Deposition on a Patterned Chip

We used a custom designed and specially patterned Gold-Silicon chip for the electrical characterization i.e., Current-voltage measurements (I-V). Custom designed chips were fabricated using a SiO_2 substrate that had Cr_2O_3 coating beneath the patterned gold electrodes. GO was thus deposited on patterned chips that were washed, treated with piranha solution, dried and then surface functionalized with PAH / APTES by dipping them in a solution of GO (0.5 mg/mL) for 3 minutes. The chips were then taken out and annealed for 30 minutes at 120℃ to enhance the adhesion between GO and electrodes.[37]

3.2 Atomic Force Microscopy of Plain GO

Once GO was synthesized and successfully deposited on SiO_2 substrate and Au-chips, we wanted to validate the size and thickness of as produced GO sheets. GO was deposited on a surface functionalized Silicon chips (SiO_2 substrate) and atomic force microscopy (AFM) was performed on this sample. AFM analyses revealed that GO sheets had lateral dimensions in the range 200-4000 nm with the height of the monolayer ranging between 1.1±0.4 nm (Figure 3-4). This value is slightly higher than the theoretical value of 0.8 nm and this slightly higher value of thickness can be attributed to GO monolayers bearing many oxygen rich functional groups like epoxy, hydroxyl, and carboxylic groups.[15, 20, 32]
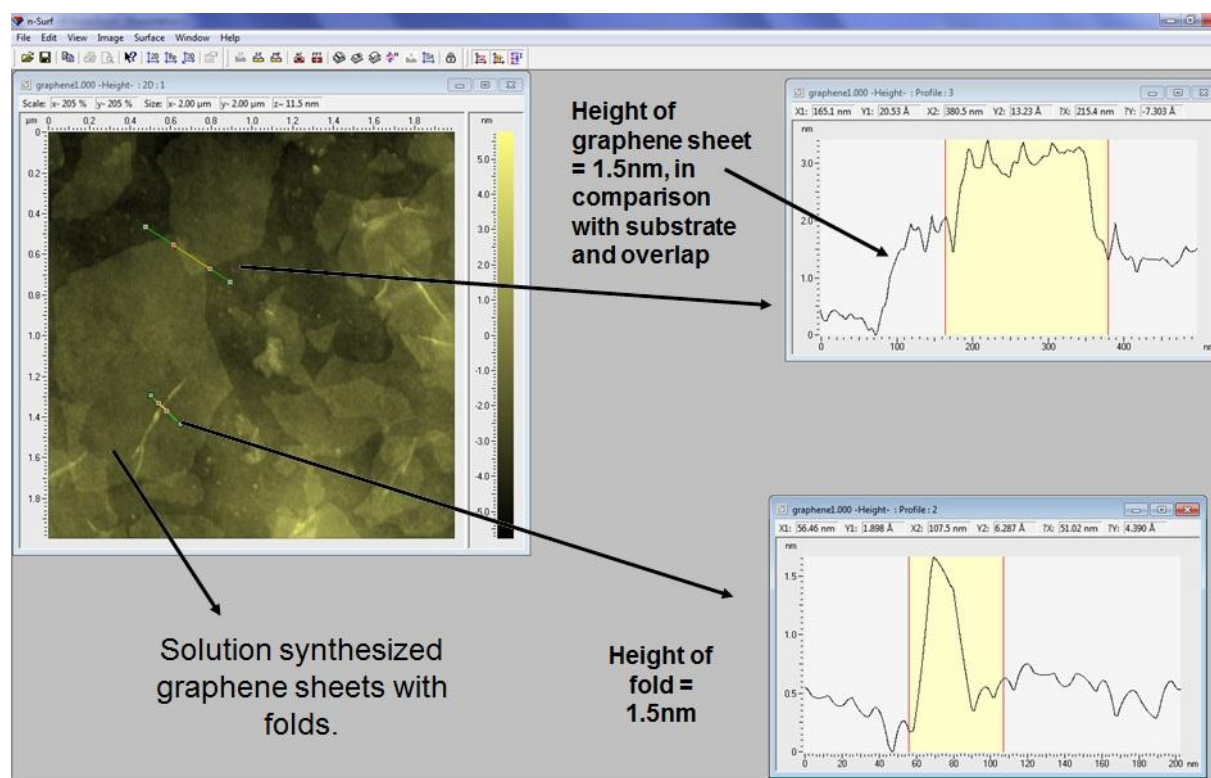
Figure 3-4: AFM image of GO monolayer.

Figure 3-4 illustrates the AFM image analysis of GO sheets. In the Figure 3-4, we can notice GO monolayers, wrinkles or folds and the overlapping of GO sheets. The inset of the image shows a pronounced surface roughness which can be ascribed to sp^3 centers, oxygen-rich functional groups and point defects in the honeycomb lattice that cause wrinkling of the sheets on the sub-nano meter scale.[18]

3.3 Electrical Characterization

To measure the electrical current, we used a custom built I-V setup that used SPM probes as the I-V leads.

Current (I) Measurement   Voltage (V) Measurement   (a)

(b)   SPM Probe tips
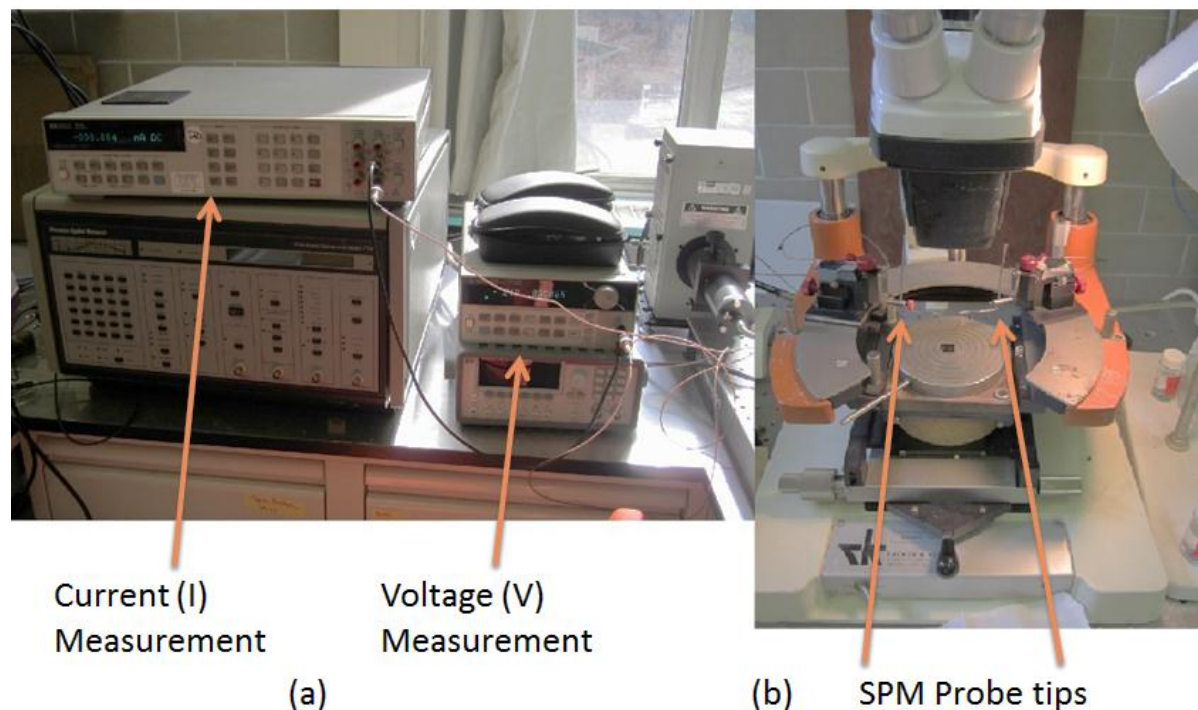
Figure 3-5 : Custom built I-V setup

Design of the custom I-V setup is made up of a Hewlett Packard multimeter-3458A that monitors the current (I) and an Agilent 6614C DC power supply monitoring the voltage input. These two apparatus were controlled virtually by a computer that is configured to LabVIEW interface and all the readings were recorded this way in all other experiments (Figure 3-5). Characterization of GO's electrical conductivity was done by running I-V measurements on the Au-chips that were surface functionalized either by PAH or APTES and had annealed GO deposited on them. The voltage was set to vary from 0 V to 20 V in a cyclical fashion for finite number of cycles and in an incremental step of 0.4 V. The resultant current flowing across the gap was measured and recorded. Figure 3-6 elucidates the way GO was deposited on Au electrodes on a patterned Au-chip. The inset in the Figure 3-6 explains the effects of annealing i.e., enhanced adhesion of GO to the Au electrode pads. The consequential I-V curves resulting from the

measurements were used to understand the electrical conductivity, the charge carrier transport models and we compare these results with the existing models which are in unison with the observed implications.
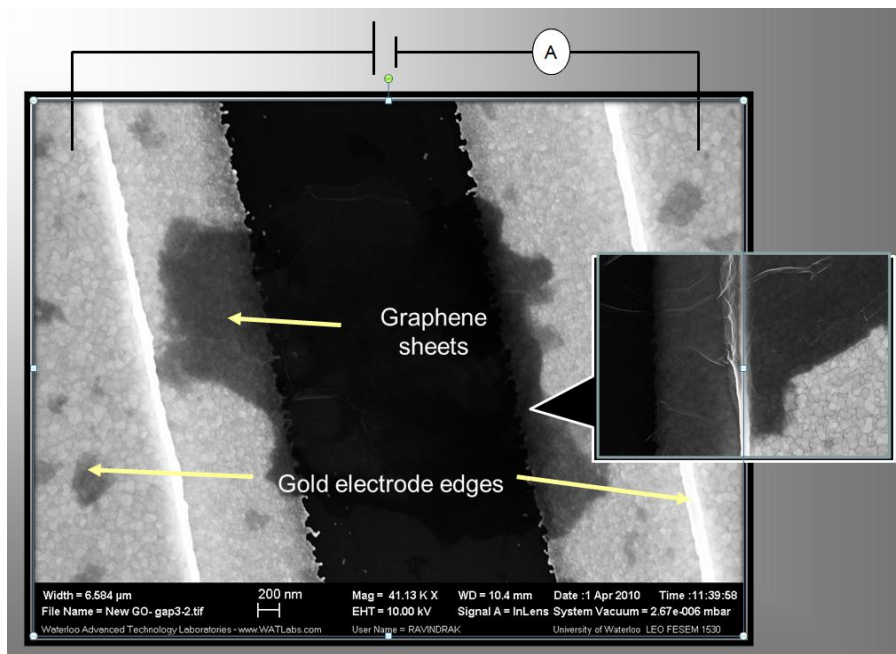
Figure 3-6: GO sheet on an Au-chip: I-V measurement.

3.3.1 I-V measurements
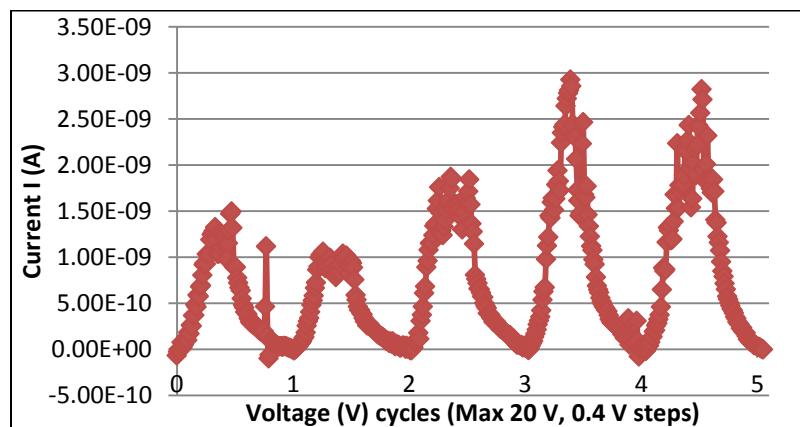
Figure 3-7: I-V results on a PAH treated Au-chip.

Electrical characterization of graphene deposited on chips is an important factor which decides its functionality as a sensor. Figure 3-7 shows the I-V curve for GO deposited on a PAH functionalized chip. The noise in the I-V curve can be attributed to arise from the hydrophilic nature of PAH and adsorption of moisture. Figure 3-8 shows GO sheet on a PAH treated Au-chip.
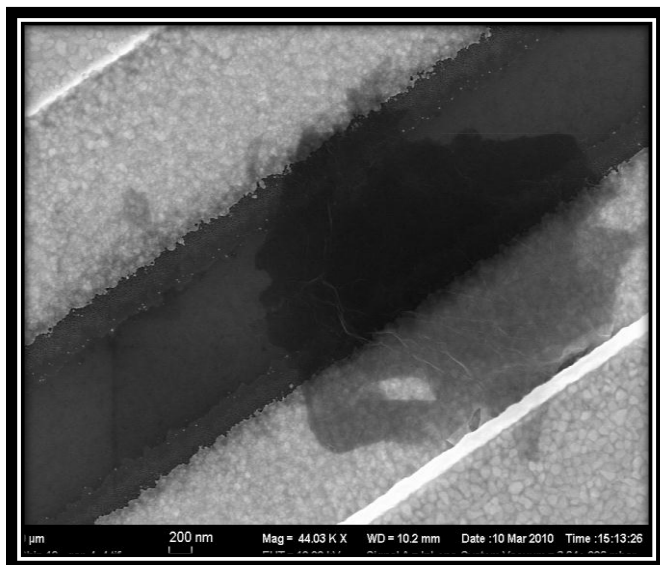
Figure 3-8: GO sheet on a PAH treated Au-chip
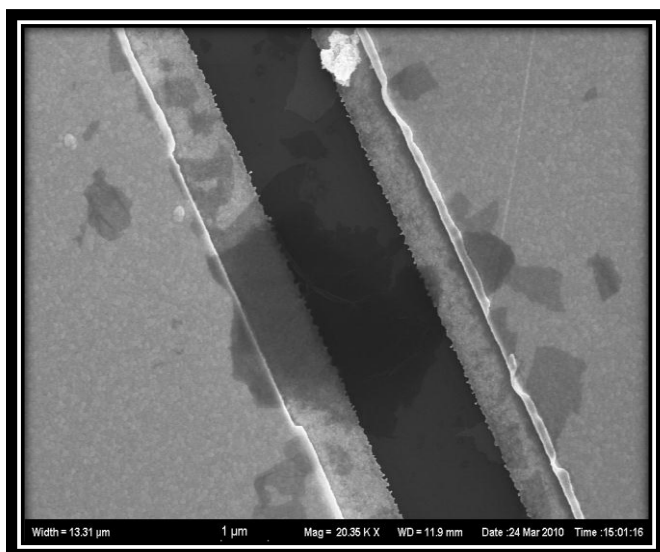
Figure 3-9: GO sheets on an APTES treated Au-chip

21
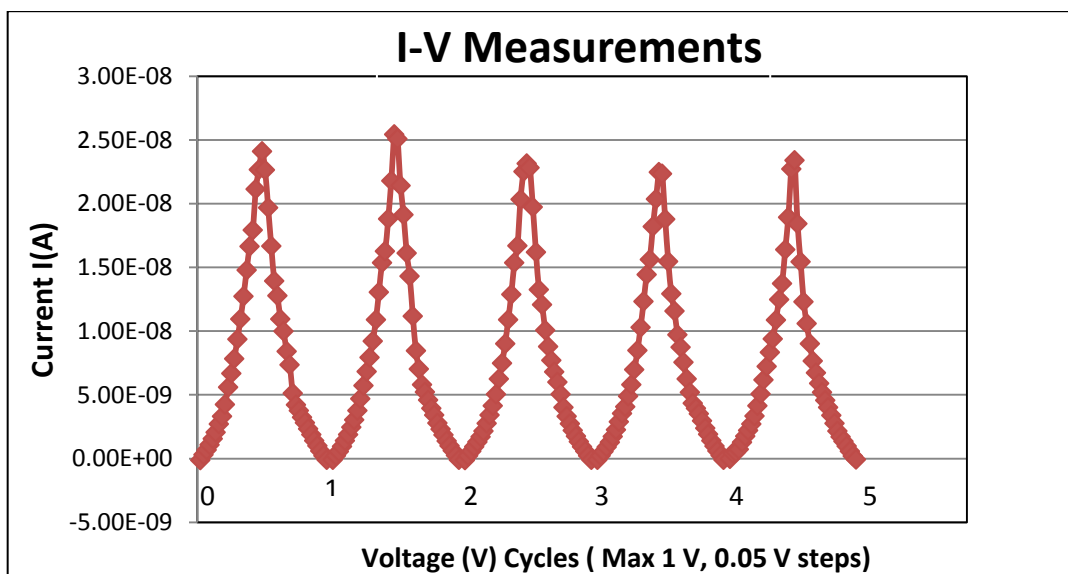
Figure 3-10: I-V results on an APTES treated Au-chip

Au-chips that were functionalized with APTES constantly proved to maintain less noise and steady currents during I-V measurements and hence APTES was chosen as the surface primer for all future experiments. During the measurement direct current (I) was flowed between the Au electrodes bridged by GO sheets. The current was ramped from zero to a fixed upper value and then back to zero. During the ramping cycle, at every instance five readings were taken and averaged to a single value as denoted by the I-V plot. The voltage variation across the Au electrodes of each of the four main gaps on the Au-chip shows a quadratic dependence on the current (I) flowing through the GO sheets as described by the Equation 3-1.

$$V = a_3I^3 + a_2I^2 + a_1I + a_0$$

Equation 3-1: Dependence of I on V

The exponential trend of current (I) during the ramping cycle can be attributed to the way in which charge carriers move under the application voltage. The Voltage drop can be fitted using a third order polynomial and in this instance (Figure 3-11) the polynomial quotients are very small but the curve fits very well with the observed values.[23, 38]

The chart shows Current (A) plotted against Voltage (V), with the polynomial fit:

$$y = 3E\text{-}08x^3 - 1E\text{-}08x^2 + 1E\text{-}08x - 1E\text{-}10$$
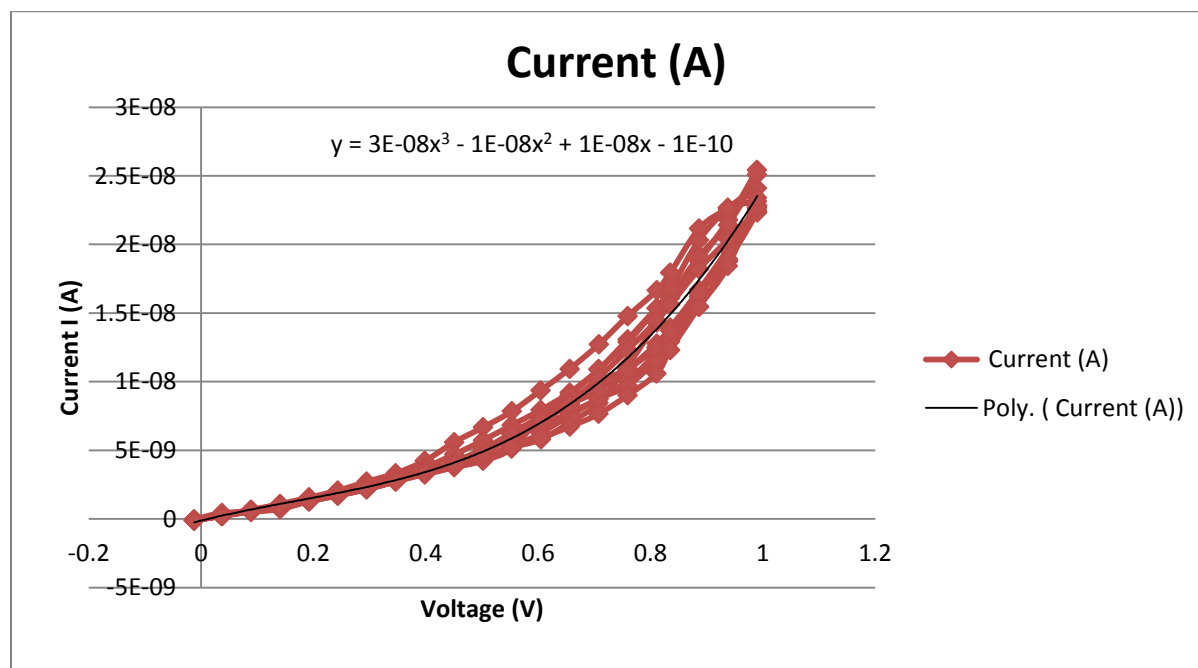
Figure 3-11: Quadratic dependence of Current (I) on voltage (V)

Experimental results from transport measurements show that graphene has remarkably high electron mobility at room temperature with reported values in excess of 200,000 $cm^2V^{-1}s^{-1}$. The symmetry of the experimentally measured conductance indicates that the mobilities for holes and electrons should be nearly the same (also see Figure 4-17). However, for graphene on SiO_2 substrates, scattering of electrons by optical phonons of the substrate is a larger effect at room temperature than scattering by graphene's own phonons, and limits the mobility to 40,000 $cm^2V^{-1}s^{-1}$.[2, 12, 39]

3.3.2 Dependence of Current (I) on Temperature

To understand the charge transport in graphene, it was necessary to determine the effect of temperature on the electrical conductivity. Au-chips were deposited with GO and then currents were measured upon the application of bias voltage (V_B). A maximum of 1.0 V in steps of 0.05 V was applied in a cyclical fashion (3 cycles) and the resultant currents for different temperatures i.e., room temperature ~ 24℃, 40℃, 80℃, 120℃ and 160℃ were measured. From the Figure 3-12 we can observe that current (I) shows an exponential rising trend with the increase in temperature which is a characteristic of one of the proposed models for the charge carrier transport in GO i.e., Two-dimensional (2-D) Variable Range

Hopping (VRH). As the temperature increases, the thermodynamic fluctuations on the surface of GO escalates making room for enhanced conduction pathways. The long range scattering of charge carriers without dropping the kinetic energy at elevated temperatures is discussed in the following section.

3.3.3 Variable Range Hopping Conduction

VRH involves consecutive inelastic tunneling processes between two localized states and has been frequently observed in disordered systems, including amorphous carbon. Hopping presumably occurs between the intact crystalline graphene regions that are separated by clusters of point defects or grain boundaries.[40]
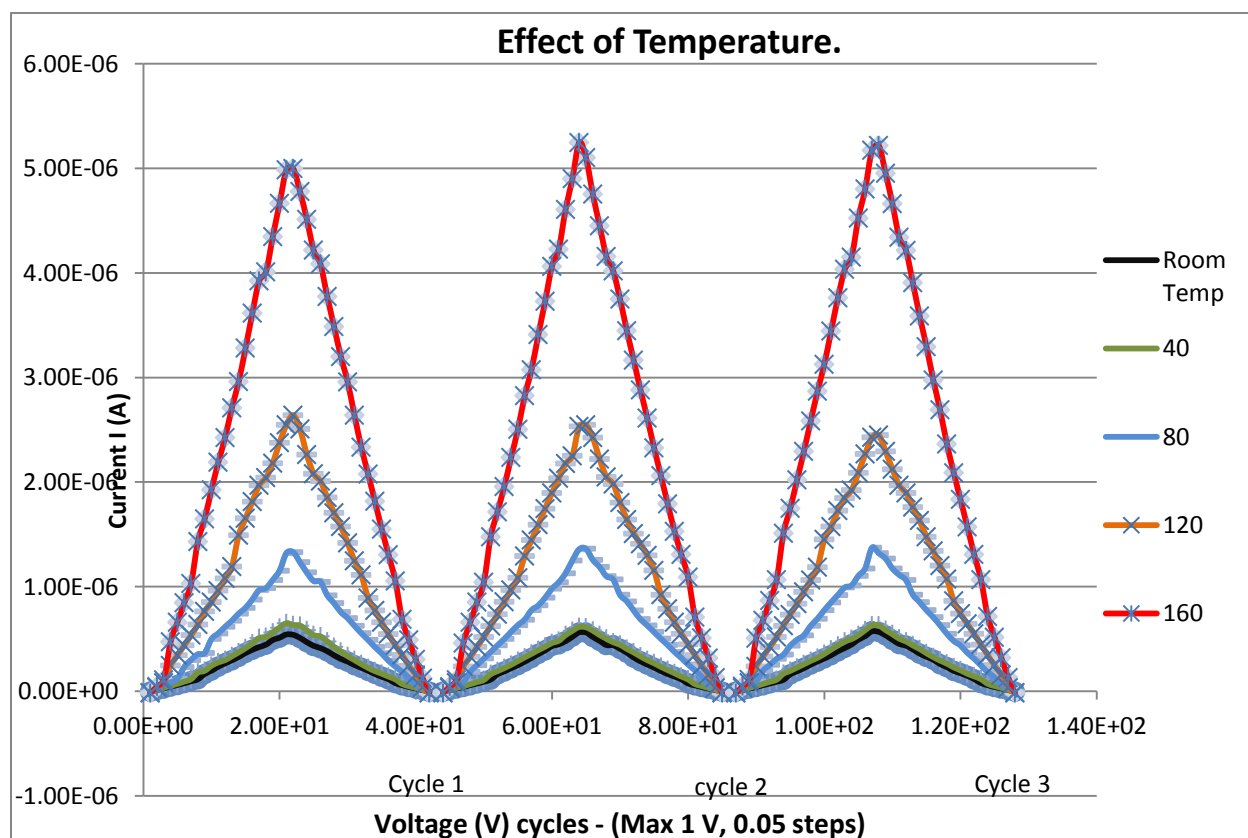
Figure 3-12: I-V curves indicating the dependence of current (I) on the temperature.

Temperature dependence conductance G(T) for the GO sheets can be explained using VRH mechanism and is given by the expression

$$G(T) = G_1 e^{\left(\frac{-B}{T^{1/3}}\right)} + G_o$$

Equation 3-2: Temperature dependent conductance

The first term represents the usual 2D VRH conduction expression and the second term G_o represents purely field-driven conduction without the thermal activation i.e., independent of temperature, and is dependent on the gate voltage (if any) applied to the system.[40]

$$B = \left\{\frac{3}{kN(E_F)L_l^2}\right\}^{1/3}$$

Equation 3-3: Hopping conduction parameter

The hopping parameter B depends on the density of states $N(E_f)$ near the Fermi level and the localization length L_l of the electronic wave functions involved. K is the Boltzmann's constant.

The fitted values of the dependence of current on temperature ($T^{-1/3}, K^{-1/3}$) (the magnitude of the slope of the linear portions) are found to be in consensus with the equation. It was observed by Gomez-Navarro et al., that the resistance in the graphene sheet could be a phenomena involving tunnelling effect (through schottky barriers) at the electrode contact points, resistance of graphene sheets (single, multiple) and asymmetric scattering by charged impurities. We can infer from Figure 3-13 that the common feature of the plot is linear dependence of natural logarithm of current (I) *Ln I* with the temperature $T^{-1/3}$, which is an indicative feature of 2-D VRH.[41] As the temperature increases beyond 80°C, we notice the change in linearity of the curve. When the Au-chip deposited with GO was heated on a hotplate to desired temperatures, the gate voltage across the system (V_g) was kept at zero. The current (I) is observed to increase exponentially at constant temperatures with the increase of applied bias voltage (V). The assembly of grain boundaries in the poly-crystalline GO, the localized dislocations, doping effects and defects play a vital role in deciding the conductivity of a given sample. Recently it has been shown that by tailoring the topology of grain boundaries or the number of layers in FLG, the band gap can be manipulated in a controlled fashion to a very large extent.[42, 43]
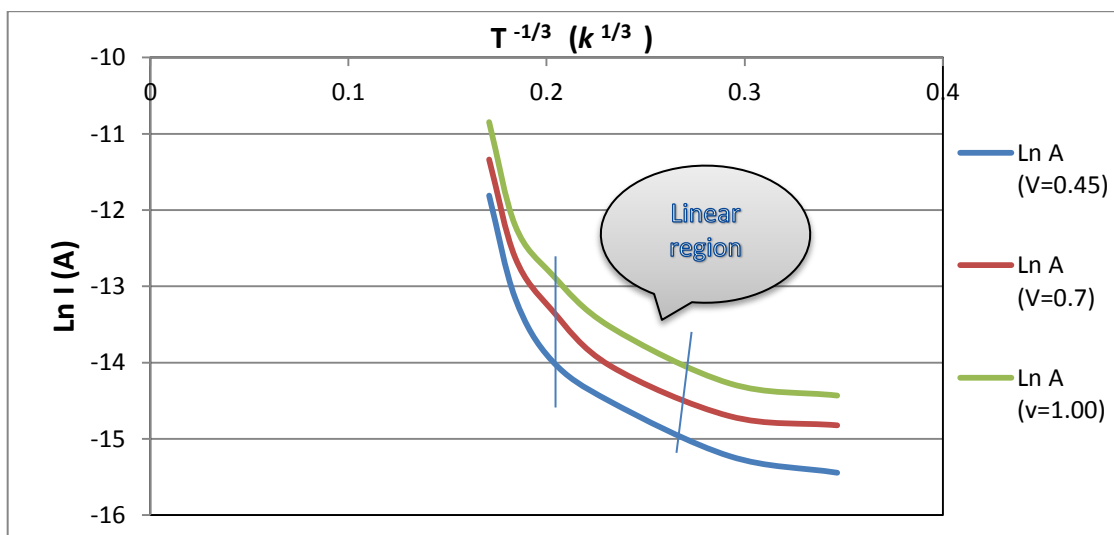
Figure 3-13: Natural logarithm of current I (A) Vs $T^{-1/3}(K)$.

3.4 Reduction of Graphene Oxide

After synthesizing GO and testing the I-V characteristics of it, it was apparent that GO did not exhibit the kind of conductivity as shown by pure graphene sheets that are prepared by methods like CVD or mechanical exfoliation. One of the reasons for the reduced conductivity of GO is due to disrupted sp^2 bonding networks as a consequence of the oxidation or exfoliation that infuse oxygen-rich functional groups, defects or dislocations forming grain boundaries. To enhance the electrical conductivity of disrupted GO, π-network has to be restored to a structure that is fairly similar to that of pristine graphene as obtained by mechanical exfoliation and reduction of GO is one of the important steps towards that.[18, 44] A variety of chemical methods have been employed to reduce colloidally dispersed graphene oxide. The most widely used chemical was hydrazine monohydrate (N_2H_4). Whilst most of the reducing agents are quite reactive in water, hydrazine monohydrate on the other hand is not reactive in water, making it a viable option for the reduction of solution dispersed graphene oxide. The actual reduction mechanism of hydrazine with GO is still unclear but gleaning from actual reduction pathways of hydrazine in organic systems and the characterization of the reduced counterpart (RGO) the reduction of GO by hydrazine is expected to involve the *syn* addition of H_2 to alkenes/epoxides groups and the consequent ejection of oxygen as shown by the Figure 3-14.[45]
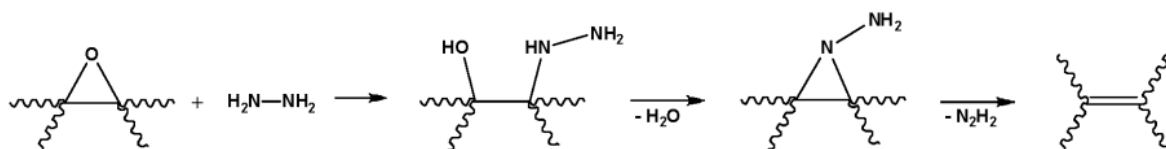
Figure 3-14: Proposed reaction pathway for epoxide reduction by hydrazine.

3.4.1 Experimental Setup for Reduction of GO
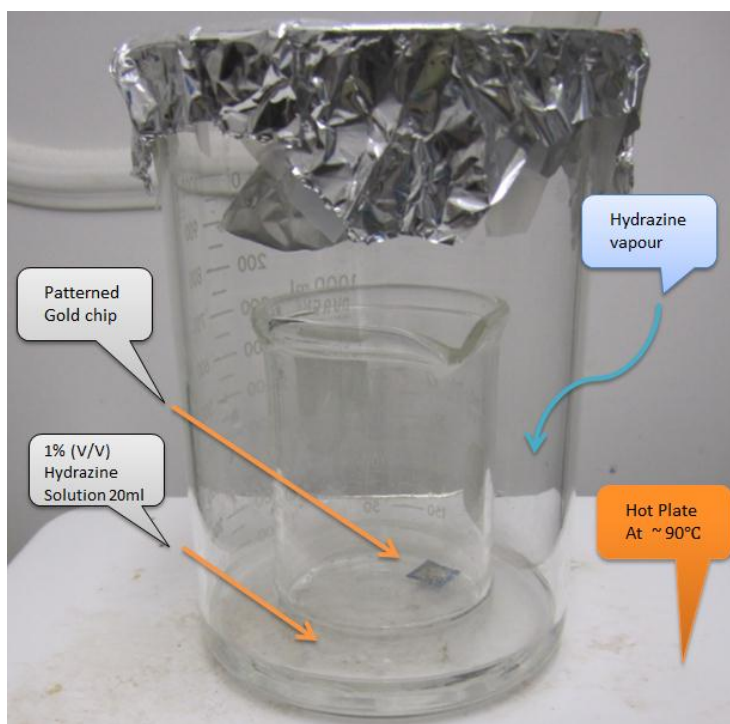
Figure 3-15: Experimental setup for hydrazine reduction

We decided to use hydrazine monohydrate for the reduction of GO. The GO was first deposited on a piranha treated, surface functionalized Au-chip and annealed. Then, the chip with GO was placed inside a small glass beaker which in turn was kept in a larger cylindrical glass beaker that had 10 ml of diluted (1% v/v) of hydrazine monohydrate (98% N_2H_4, Alfa Aesar).

The larger glass beaker was covered with a lid, sealed using paraffin film and covered with aluminum foil to ensure that hydrazine vapors do not escape (see Figure 3-15). The glass setup was placed over a hot plate at 80℃ for 1 hour. [30,46]

The reasoning behind this is to allow hydrazine vapors to impact the GO surface and thereby reducing it to RGO. The chips were then taken out, washed with Millipore™ water to remove any unwanted hydrazine traces, annealed at 120℃ and cooled. The voltage was set to vary from 0.0 V to 2.0 V in steps of 0.05 V for four cycles and the current (I) was recorded. The comparison of the I-V curves is shown in Figure 3-16. The Y-axis of the curve in the Figure 3-16 is plotted on a logarithmic scale.
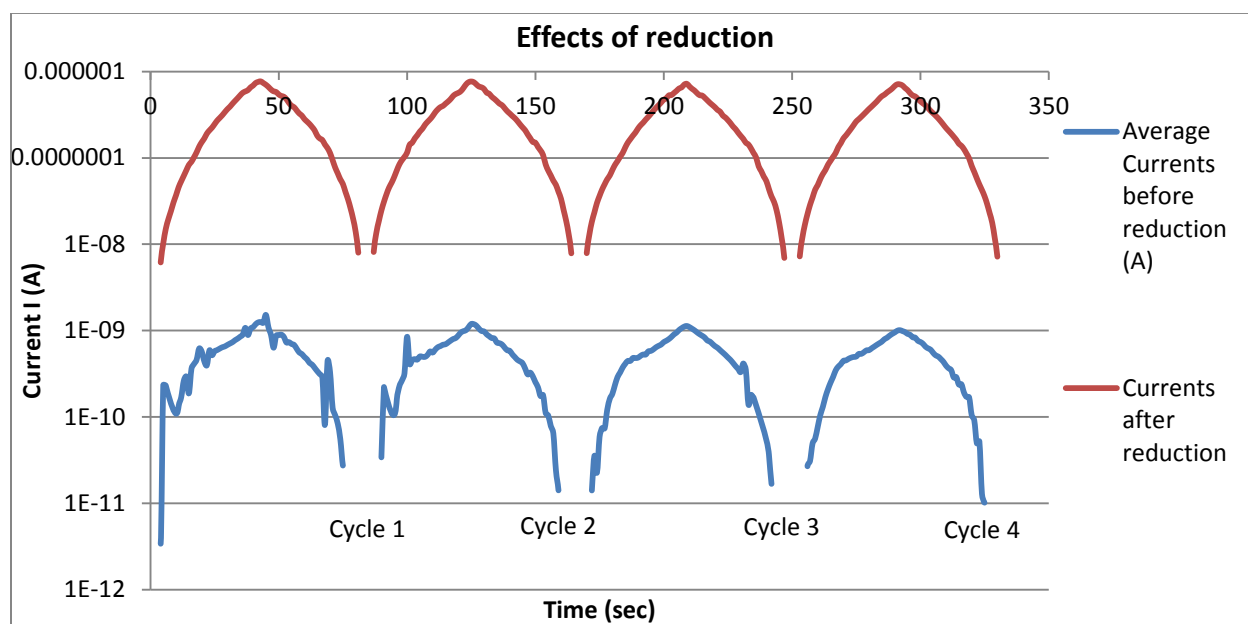
Figure 3-16: I-V curves showing the effect of reduction on GO

The conductivity of the reduced GO was tested and we found that the conductivity was approximately 3 orders of magnitude higher compared to the unreduced GO. This increase in conductivity can be attributed to the elimination of epoxide, hydroxyl groups from the GO surface. In order to evaluate the conduction mechanism in RGO monolayers with respect to VRH, we made use of the equation which relates conductance with applied bias voltage and temperature. To the Equation 3-2 we have added an additional exponential term where r(T) is the mean low-field hopping distance and e is the electronic charge. Inference drawn from the literature surveys shows that quantitative estimation of r(T) have

proved that VRH happens only in part of the sample which means that voltage across the surface is not uniform but fragmented into different compartments of different length over which hopping of charge occurs. Apart from the hopping of charges over the conduction pathways, the contribution of direct tunneling through the barriers between delocalized electron states in the well-ordered regions of GO can be substantial.[47]

$$G(T, E) = G_o + \left(G_1 e^{\left(\frac{-B}{T^{1/3}}\right)} \right) e^{\left(\frac{0.18er(T)}{kT}E\right)}$$

Equation 3-4: Variation of conductance with voltage (V) and Temperature (T)
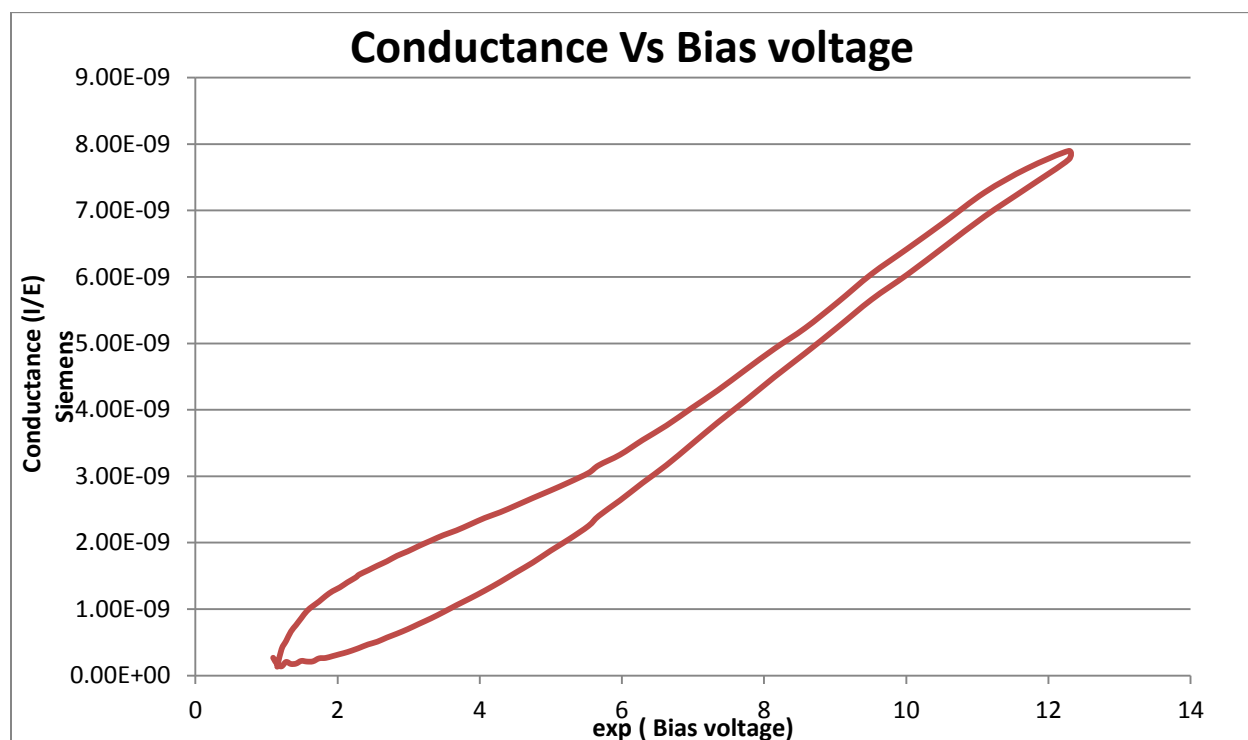
Figure 3-17: Variation of conductance Vs Bias voltage.

The variation of conductance (I/E) with the applied voltage can be inferred from the above graph (Figure 3-17). The linearity of the slope of the curve is an indicative feature of VRH. [47]

Chapter 4

Electromechanical Coupling

4.1 Introduction

The goal of electromechanical coupling at the nano scale is to build devices that are multifunctional, exceptionally small and very highly sensitive. Most of the applications of nano devices rely on their high-aspect ratio providing them particular physical features. The advantage of these devices arises from the size compatibility of the nanomaterials with biological samples. Graphene is the thinnest material, combined with its exceptional properties it is an ideal candidate for nano-scale sensing devices.[48,49]

Fundamentally electromechanical coupling at the nano scale is required to interface biological species with the electrical leads in order to get a true picture of the processes and events that take place inside unmodified living cells such as cell division and energy production involving electrochemical reactions. Due to their small dimensions, high-aspect ratio nanomaterials such as nanofibers (NFs), nanowires (NWs), carbon nanotubes (CNTs) and graphene are ideal for cellular applications since they can rest across the cell membrane without causing significant damage.[50]
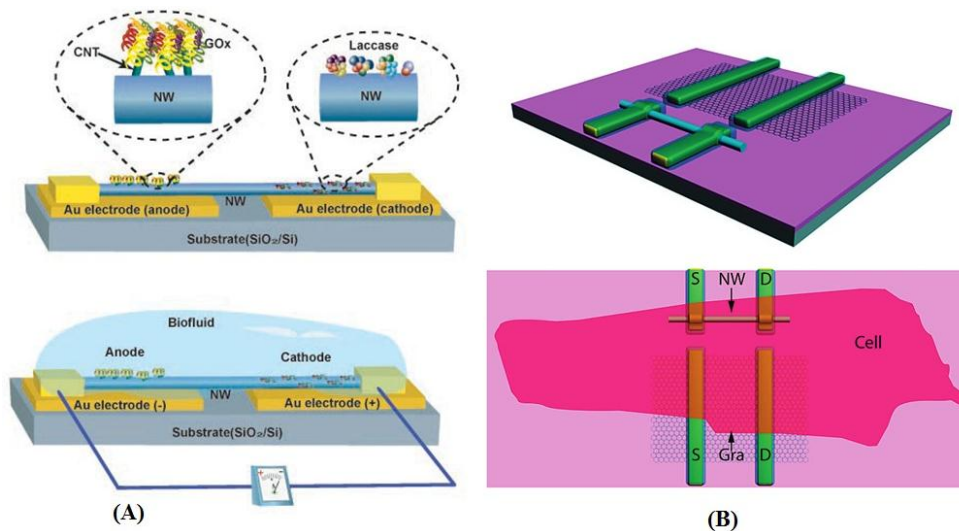
Figure 4-1: (A) NW based sensing device, (B) NW-FET based graphene sensor.[51]

Recently, field effect transistors (FETs) of nanowires, carbon nanotubes, and recently graphene have been used for this purpose. Figure 4-1 shows the devices that are devised recently that make use of NWs and NW-FET coupled with graphene. The cells / biological entity is placed over an FET / electrical lead to form cellular-electrical interface and this could be restraining the contact area between cells and electrical interface considering the fact that graphene or NWs have very high surface area to size ratio.[52]

4.2 Electromechanical Coupling

4.2.1 Coupling Methodology

In our work we wanted to utilize graphene as the electrical interface and we have successfully interfaced it with the Yeast cells. We demonstrated the electromechanical coupling by forming an electrically conductive layer of reduced graphene oxide on yeast cells. Firstly, we used a combination of nanoparticles to couple GO with the yeast cells. Plain GO was then reduced to RGO and RGO was then coupled with the cells in the exact same way. I-V measurements were done to study the electrical behavior of the system. The coupling is termed as "electromechanical" because of the nature of the cellular/graphene interface. Any mechanical stress induced on the surface of the cells will in turn stress the RGO sheets encapsulating them. Straining of RGO sheets can arise out of various parameters like mechanical force, electrical heating, and external chemical ambience etc.[53] Once RGO sheets are deposited on the cell surface, any change that occurs within the cell leading to a change in cell volume or surface stresses will affect the RGO sheet's conductivity and shape. The change in conductivity thus arising out of such cellular modifications can be used as means to study the important cellular processes such as cell growth, cell division and physiological response of cells to external stimulus. UV-Visible spectroscopy (UV-Vis), Field emission scanning electron microscopy (FESEM), Transmission electron microscopy (TEM), AFM and LIVE/DEAD® tests were used as tools to study the experimental samples and characterize the results.

4.2.2 Yeast Cell (SaC)

The biological species used for the purpose of electromechanical coupling was "Yeast cells". Yeast cell or *Saccharomyces cerevisiae's* (SaC) is a tiny form of fungi or microorganism (visible only under microscope) that exist in variety of conditions like water, soil, plants and air etc. Yeasts are unicellular organisms that reproduce asexually by mitosis, and many do so via an asymmetric division

31

process called budding. Over 600 species of SaC have been identified as a part of visible nature. Some of the common forms of edible yeasts are mushrooms, blooms on the grapes; bread (has baker's yeast). It is a model organism for the study of cell biology and has been extensively characterized and used for the development of new tools in biotechnology. The primary reason for choosing to interface graphene with yeast cells is being eukaryotic cells they have functional similarities to human cells and are robust to environmental conditions. The scientific name *Saccharomyces cerevisiae,* means 'a mold which ferments the sugar in cereal to produce alcohol and carbon dioxide'. A very important reaction (Equation 4-1) in this process is the conversion of simple sugars to ethyl alcohol and carbon dioxide.[54]

$$C_6\,H_{12}\,O_6 \;\rightarrow\; 2\,CH_3CH_2OH + 2CO_2$$

Equation 4-1: Fermentation of simple sugars using yeast.

Figure 4-2 illustrates (A) a typical yeast cell, (B) skeletal diagram of yeast and inner sections are mentioned.
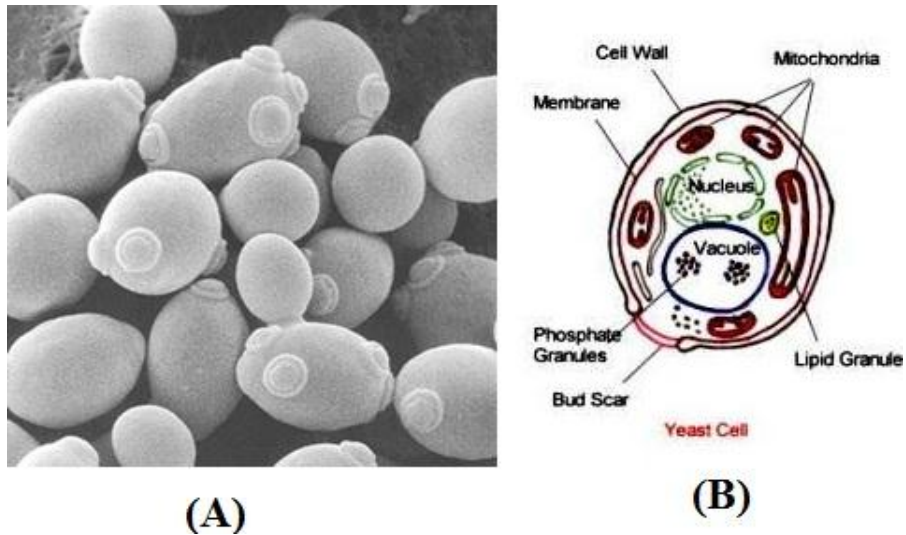
Figure 4-2: (A) Typical yeast cell, (B) Skeletal diagram of yeast cell.[56]

Examination of a yeast cell under a microscope will give a greater understanding of the composition and nature of yeast. The method for viewing a sample of yeast under an optical microscope is to disperse a small amount of yeast in water, causing the water to be slightly clouded, and then drop a spot of the liquid onto a glass slide. The drop is then covered and viewed under a microscope.

Yeast cells thrive on organic compounds to grow and they need sugar, water and warmth to survive. Carbon is mostly obtained from sugars such as glucose and fructose and they reproduce via asymmetric cell budding as mentioned above.[55]

(A)　　　　　　(B)　　　　　　　　(C)
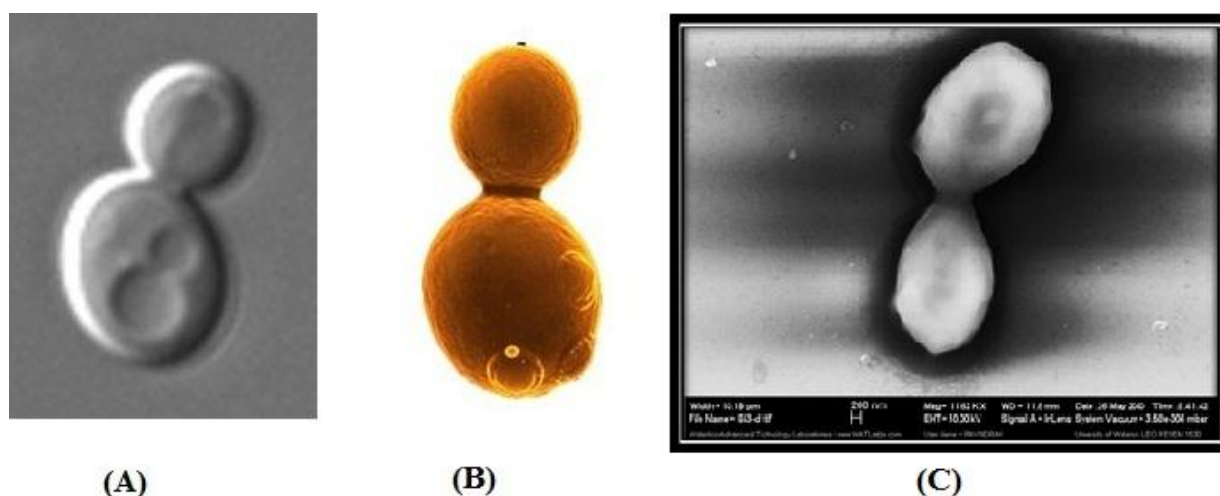
Figure 4-3: Budding yeast cell images (A) DIC, (B) & (C) FESEM.

Figure 4-3 shows the images of yeast cell as imaged by different microscopic techniques i.e., (A): Differential interference microscopy (DIC), (B) & (C): Yeast cell under FESEM imaging mode. The dark spots appearing along the boundaries of the cell wall in the Figure 4-3 (C) is because of the organic entity secreted by the cell.[56]

4.2.3 Harvesting of Saccharomyces Cerevisiae (Yeast cell)

To harvest yeast cells it is necessary to have the supplementing sugar, aqueous environment, and warm temperature. We used Yeast-peptone-dextrose (YPD) broth to grow the yeast cell cultures. 2 grams of YPD broth in powdered form was dissolved into 40 mL of Millipore™ water and autoclaved to get the broth solution. Yeast cells were grown in YPD broth using SaC stain BY4741 at 30°C for eight hours, on a shaker at 200 rpm. After eight hours, when the cells reached a logarithmic growth phase they were centrifuged for 5 minutes at 3500 RPM and subsequently washed with Millipore™ water to remove any YPD residue. Washed cells were re-suspended in 1mL water for further processing with GO.[57, 58]

4.2.4 Coupling Agent

The challenge that was faced during the coupling of GO with yeast cells was both GO sheets in water and yeast cells carry a net negative charge (zeta potential) on their surface and would not bind with each other. We took a three-stage approach to accomplish the coupling. There was a necessity to find a coupling agent that would bind to both GO and yeast cells. Calcium-Gold nanoparticles (Ca-Au) NP sufficed that requisite and Ca-Au NP was used as a binding agent.[59]

Gold nanoparticles (Au NPs) have been used as precursors in the fabrication of nano-scale devices. Necklaces of Au NPs provide a very adaptable route for the production of nanostructures and they have been used in the assembly of DNA chains, block copolymers, nanofibrils and polyelectrolytes. The electric-dipole interactions of Au NPs can be exploited to change the morphology of the resulting structure that can act as both nano-device and an integral part of the circuitry.[60]
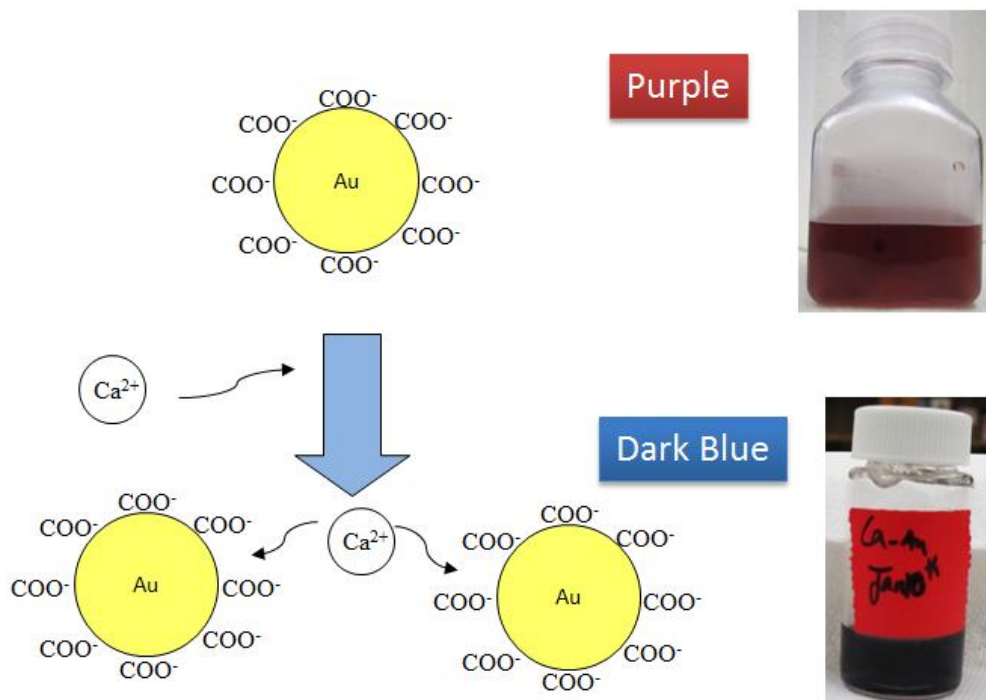
Figure 4-4: Formation of Ca-Au NPs from Au colloid.

The starting point for the preparation of Au NPs was a gold colloid. Au NPs are kept in a colloidal state by attaching citrate ions to them, giving them a net negative surface charge that keeps them repelled

from each other resulting in a purple colored stable colloidal solution. Figure 4-4 illustrates the formation of Ca-Au NPs from Au colloid.[60]

To a 4 mL of such solution, 0.35 mL of Calcium Chloride ($CaCl_2$) was added. Calcium chloride solution was prepared by dissolving 25 mg of anhydrous calcium chloride in 25 mL of Millipore™ water (1mg/1mL solution). Thus prepared calcium chloride solution was mixed with gold colloid (10nm, BBI International) and stirred for 24 hours. $CaCl_2$ being a salt solution with high dissociation constant, dissociates immediately upon being added to water. When the $CaCl_2$ solution is mixed with Au-NPs, dissociated Ca^{+2} ions bond with COO^- ions on the Au NPs to form Calcium citrate-$Ca(RCOO)_2$ and the bivalency of Ca^{+2} ions leads to the formation self-assembled chains of Ca-Au NPs. The change in color from purple to blue indicated the formation of Ca-Au NPs chain.[61, 62]
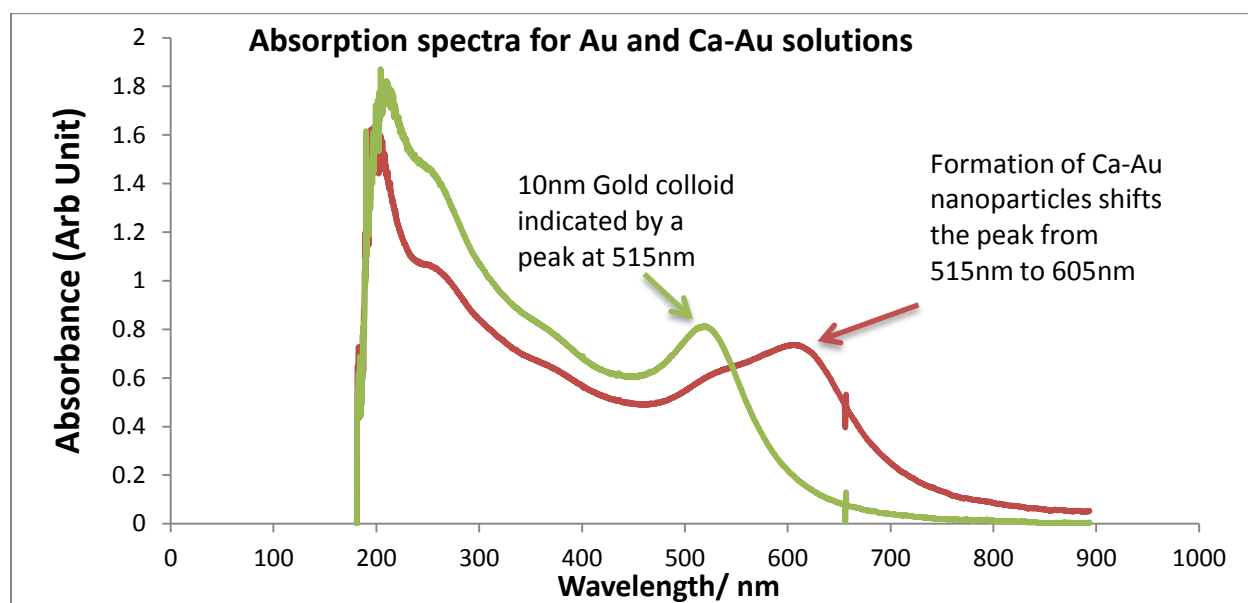
Figure 4-5: UV-Vis plots for Au and Ca-Au NPs.

Figure 4-5 illustrates the formation of Ca-Au NPs as analyzed by UV-Vis spectroscopy. Gold colloid exhibited a standard peak at 515 nm and when $CaCl_2$ solution is added to it, the formation of necklace-like Ca-Au NPs shifts the peak to 605 nm. The change in absorbance peak indicated the increase of diameter of the self-assembled Ca-Au NPs as a consequence of modified plasmon resonance at the surface of Ca-Au NPs. Figure 4-6 shows the TEM image of self-assembled Ca-Au NP chains.
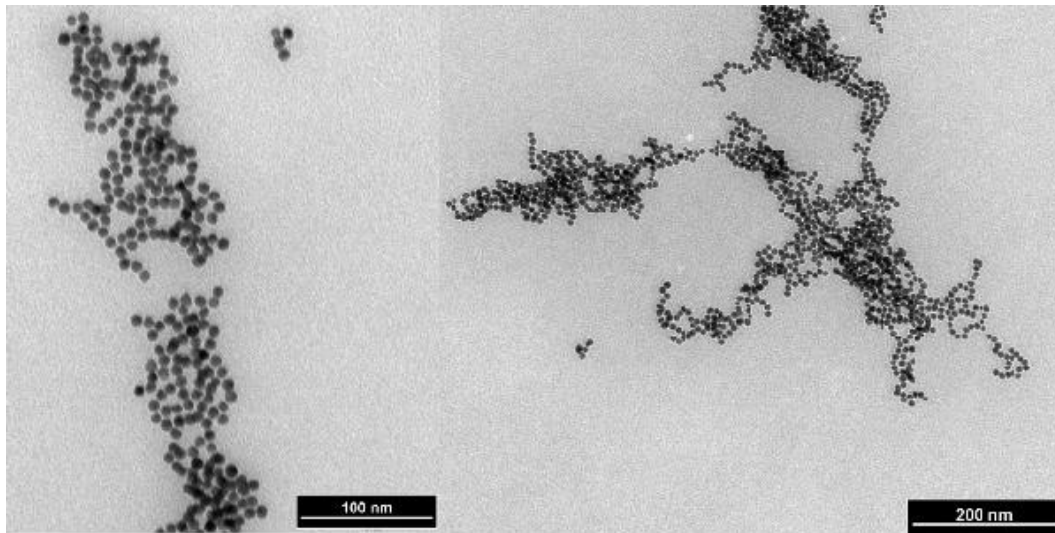
Figure 4-6: TEM image of Ca-Au NP chains

4.2.5 Pairing of GO with Ca-Au and GO with Yeast

The coupling between GO and Ca-AU NP was done simply mixing the solutions of each in a particular ratio.
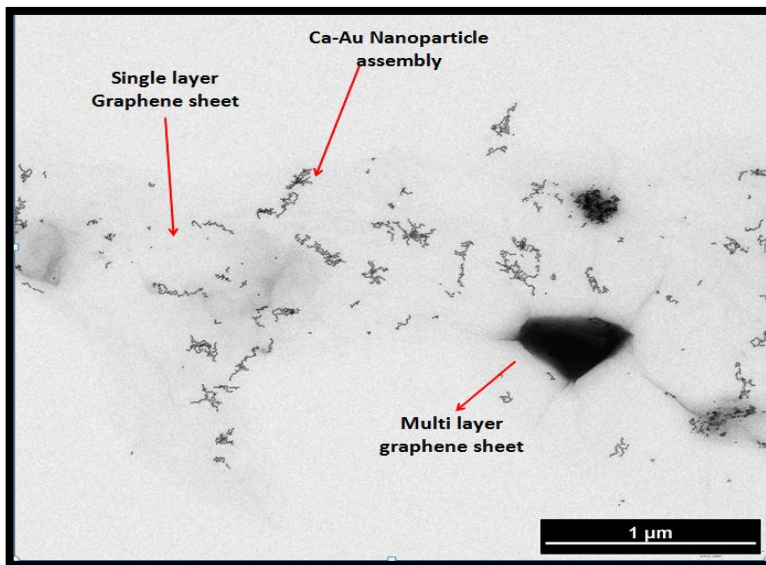
Figure 4-7: TEM image of GO-Ca-Au layer

36

GO solution (0.5mg/mL) was centrifuged at 500 rpm to remove the micron-sized particulates and then added to the preformed Ca-Au solution in the ratio1:20 (GO:Ca-Au). The solution was allowed to mix on a vortex shaker agitating the solution at 500 rpm for 8 hours to get a homogeneous solution of GO-Ca-Au. Figure 4-7 and Figure 4-8 illustrates the result of GO and Ca-Au binding.
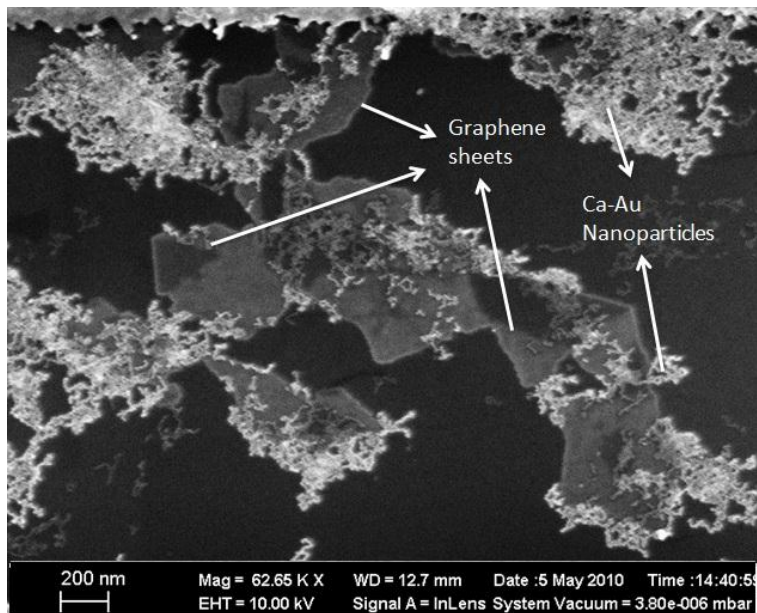
Figure 4-8: FESEM image of GO-Ca-Au layer deposited between electrodes.

We also found that Ca-Au NPs did pair up with plain yeast cells that were harvested at 8 hours of growth in a nutrient broth. FESEM image of Ca-Au-SaC showed adequate coverage of Ca-Au NPs on the surface of SaC's (Figure 4-9). Now that we were sure of the binding nature of Ca-Au with GO and SaC, we employed identical strategy to combine GO-Ca-Au-SaC in the solution form. GO (0.5 mg/mL) was mixed with preformed Ca-Au solution, stirred for eight hours and mixed with freshly harvested and washed SaC that were grown in YPD broth for 8 hours. 100 μL of washed cell suspension was added to 1mL of GO-Ca-Au solution and allowed to mix for an hour on the vibrating shaker set at 500 rpm. The resulting solution containing a refined mixture of GO-Ca-Au-SaC was used for the deposition on patterned chips. Au-chips that were treated and surface functionalized as mentioned in the 3.1.3 were dipped in the as prepared GO-Ca-Au-SaC solution for an hour, taken out to be washed and then dried in ambient air. Dried chips were used for the further studies and electrical characterization using I-V measurements.[63]
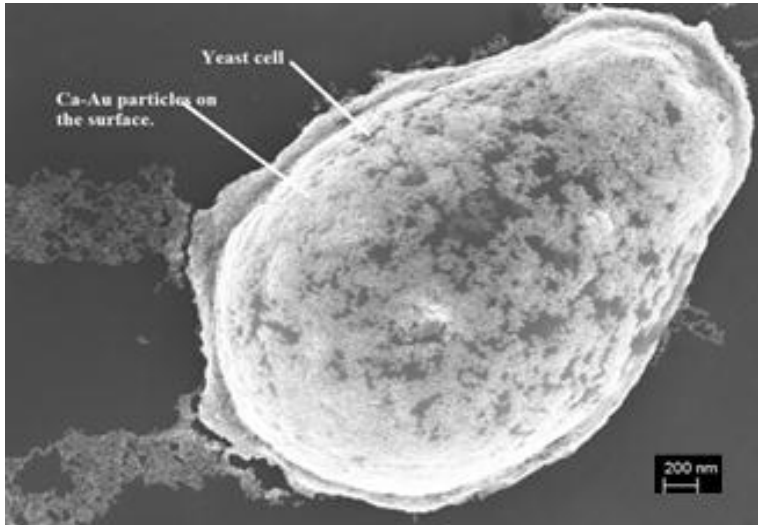
Figure 4-9: FESEM image of Ca-Au-SaC.

The fabricated interface of GO-Ca-Au and SaC that was deposited on a patterned chip shows the device that was used for electromechanical coupling and it is shown in Figure 4-11. Experiments were devised to comprehend the electromechanical behavior of the aforementioned system under various conditions and they were done in the way as illustrated by Figure 4-11. Conductivity measurements yielded the following I-V plots.
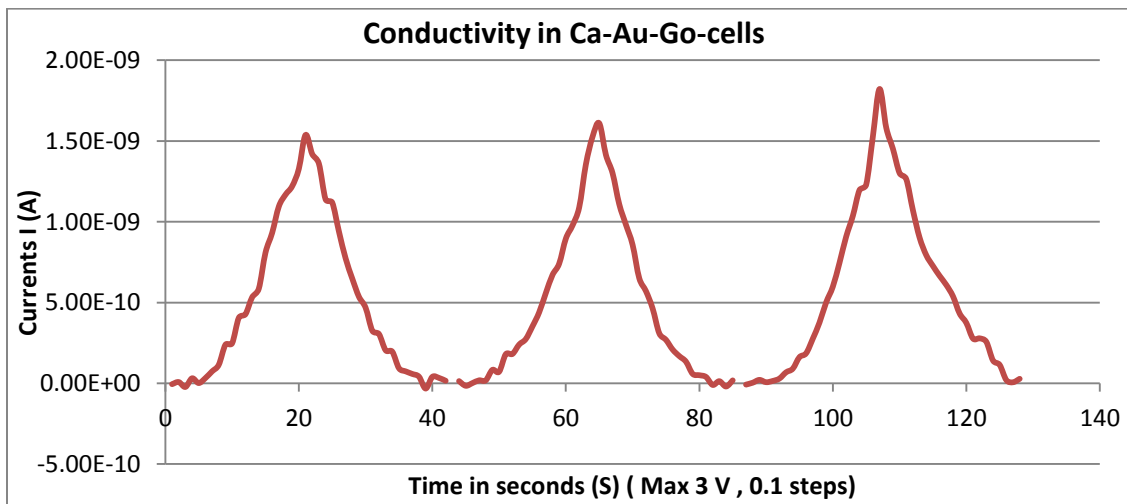
Figure 4-10: Conductivity measurement of GO-Ca-Au-SaC system.

Bias voltage was applied in a cyclic fashion in steps of 0.05 V up to a max of 2.0 V. We found that system does respond with appreciable magnitude of currents that were comparable to the plain GO samples which is an indication that GO in the system is fairly conductive though it is on the cellular surface.
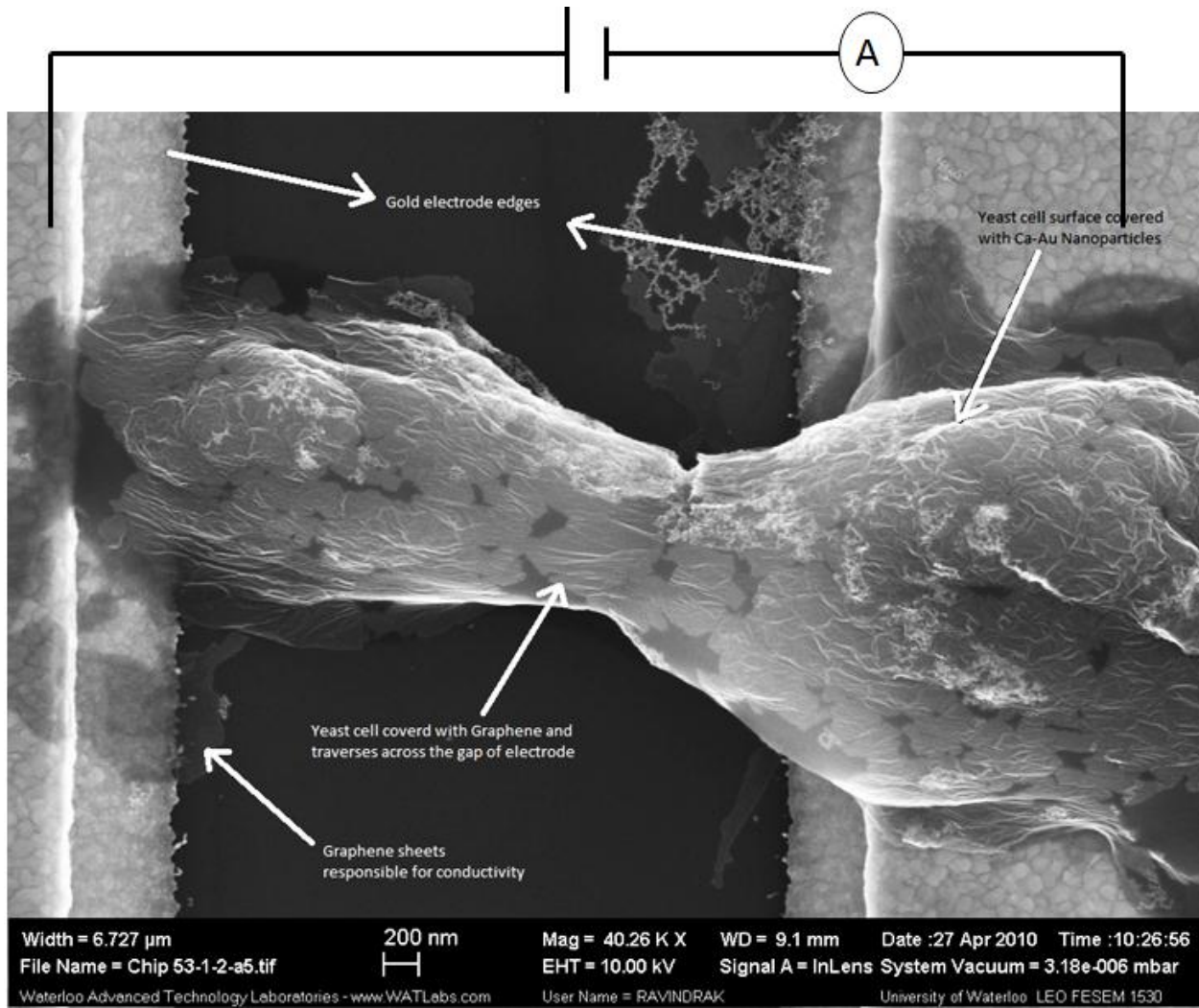
Figure 4-11: GO-Ca-Au coupled with SaC on a patterned Au-chip.

4.2.6 Reduction of GO to RGO

The next step was attempting to reduce GO to RGO thereby minimize the defects on the surface of GO and enhance the conductivity of the system. Initially we used reducing agents like hydrazine, sodium borohydride and finally chose a green process that involved the use of simple sugars like glucose.[64, 65]

Glucose acts as a reducing agent and as well as a solution friendly agent for yeast cells. The oxidized by-products of the reaction were found to act as a capping agent for the reduced GO and thereby stabilizing it. The reaction pathway for the reduction of GO to RGO has been illustrated in Figure 4-12.
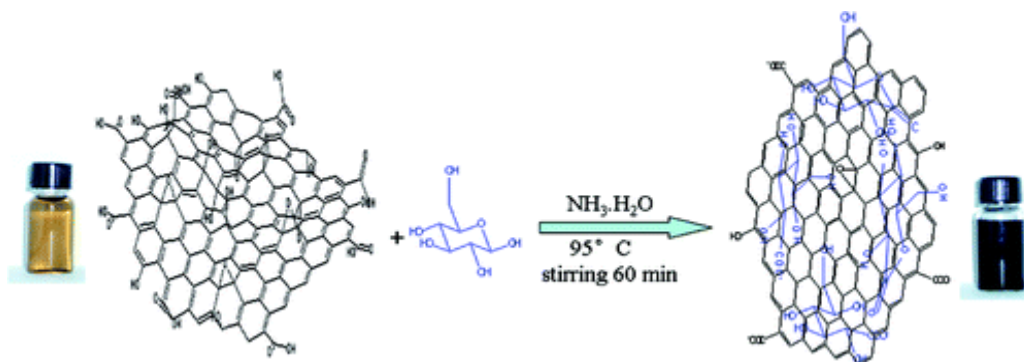
Figure 4-12: Reduction of GO using glucose.

The adopted reduction procedure is as follows, the stock GO solution (0.5mg/mL) was diluted fivefold to make it suitable for reduction (0.1mg/mL). 10 mL of such solution in a glass vial was mixed with 18 mg of glucose ($C_6 H_{12} O_6$) and heated to a temperature of 90°C in an oil bath and stirred magnetically till the mixture was homogeneous. 40 minutes into the reaction, 10 μL of ammonium hydroxide (NH$_4$OH) was added. The stirring was continued for an hour and then the solution was cooled down to the room temperature. NH$_4$OH acts a proton donor to the glucose entities and assist the reduction of epoxide and hydroxyl entities on the surface of GO. The elimination of oxygen-rich functional groups helps in the conjugation of disrupted π-network and is indicated by the change in the color of the solution from brown to pitch dark. To validate the effectiveness of the reduction process, we characterized the samples using UV-Vis and Raman spectroscopy. UV-Vis of the GO had a distinct peak of absorbance at 225 nm and after the reduction the peak shifted to 257 nm and the plot is shown in the Figure 4-13.[65]
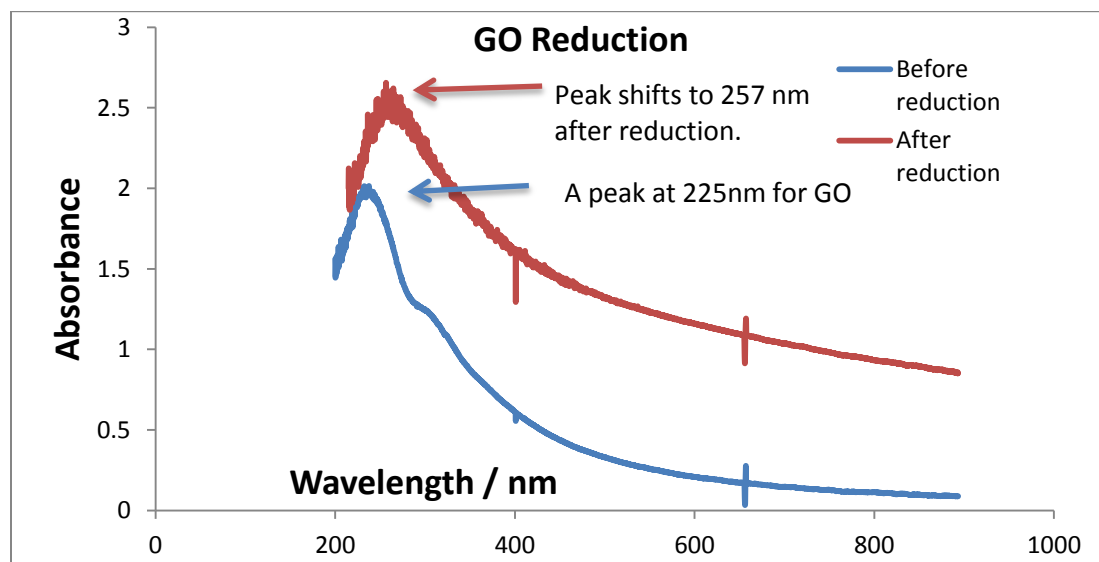
Figure 4-13: UV-Vis spectroscopy results for the reduction of GO.

We also used Raman spectroscopy as a way to validate the reduction process of GO. This is a technique where the material's vibrational, rotational modes (for liquids) and other characteristics can be studied by exciting the materials electronic states using laser. The resulting scattering phenomenon occurring between incident photons and electrons, phonons, likewise particles emit the light that is captured using a monochromator and analyzed using a detector. The previous literature data from Raman spectroscopy suggests that graphitic (derivatives) materials exhibit two distinct bands i.e., the D (associated with the order/disorder of the system) and G (an indicator of the stacking structure) bands are the dominant vibrational modes.[10, 33, 66] Pure graphite will have a very small density of disordered regions and therefore a diminutive D band. The ratio of the intensities of the two bands (D/G) is often used as a means of determining the number of layers in a graphene sample and its overall stacking behavior; high D/G ratios indicate a high degree of exfoliation/disorder. The GO, RGO and HRGO samples were excited with 532 nm laser on a Bruker Senterra Raman spectrometer. The results showed that the value of D/G ratio changed from 0.93 to 0.99 for the glucose reduced GO and in the case of hydrazine reduced GO the ratio set out at 1.20 indicating a higher density of smaller ordered sections formed from the previously disorderly oxidized region. Figure 4-14 illustrates the Raman spectroscopy results for GO, RGO and HRGO samples (maintained at neutral pH).[67] We did not employ the hydrazine reduction process for the electromechanical coupling as it is a chemical and can have adverse effects on the system.
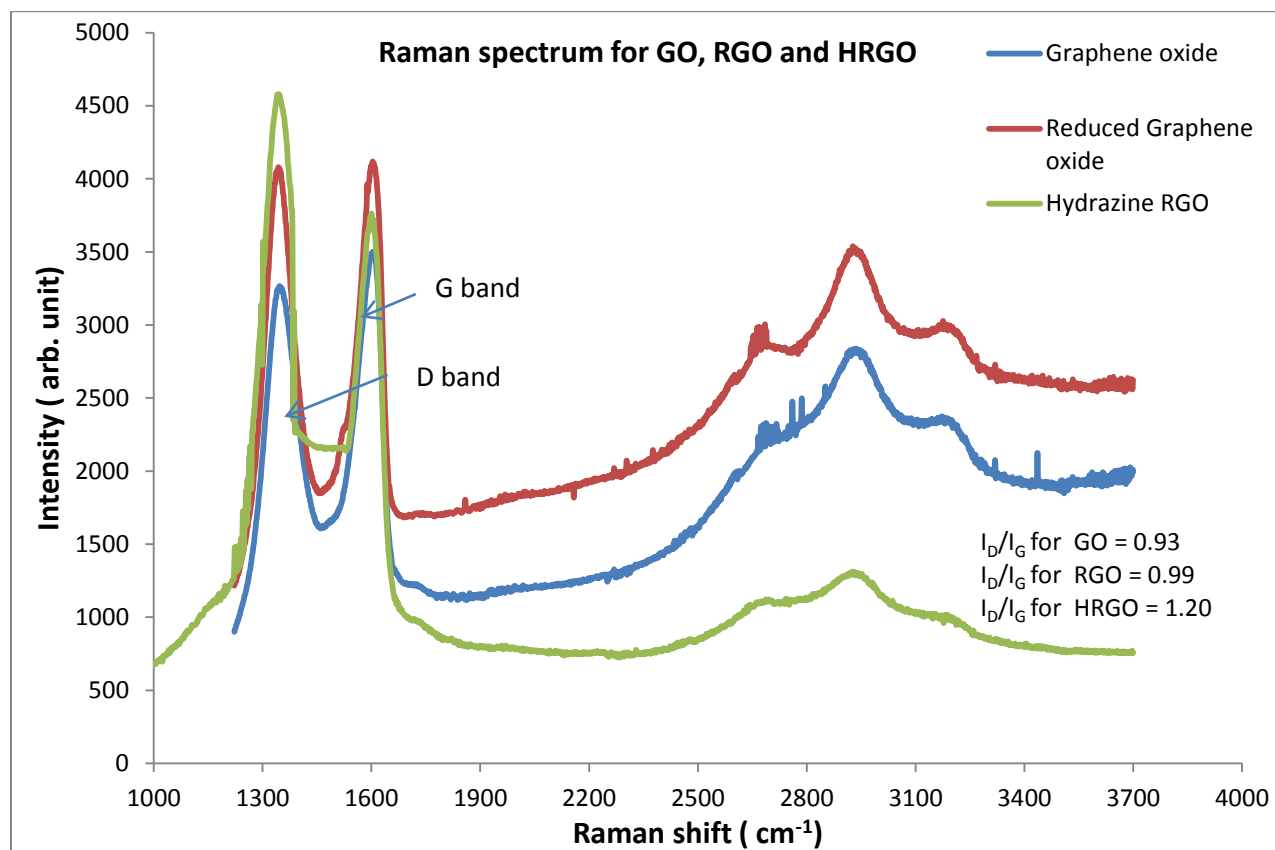
Figure 4-14: Raman spectroscopy for GO, RGO and HRGO.

The amalgamation of RGO-Ca-Au-SaC was accomplished using the same method as mentioned in the section 4.2.5 and deposited on a gold chip that is surface-functionalized as mentioned in the section 3.1.3. The chip was immersed in RGO-Ca-Au-SaC solution and was given an hour to allow the cells to deposit on the surface. The chip was then washed, dried and used for the I-V measurements. I-V plots of this sample showed significant increase in the current (I) by an order of thousand. The voltage was applied in a cyclical fashion and in small steps of 0.05 V to a maximum of 1.0 V. The magnitude of currents observed was in the order of μA.

The rest of the samples prepared in similar manner showed identical trend in the I-V measurements, the magnitude of current (I) varied from a few hundred nA to tens of μA. The increase in current (I) can be attributed to the enhanced conductivity of RGO sheets and optimal coverage of RGO sheets on the SaC forming conductive pathways (Figure 4-15 and Figure 4-16).
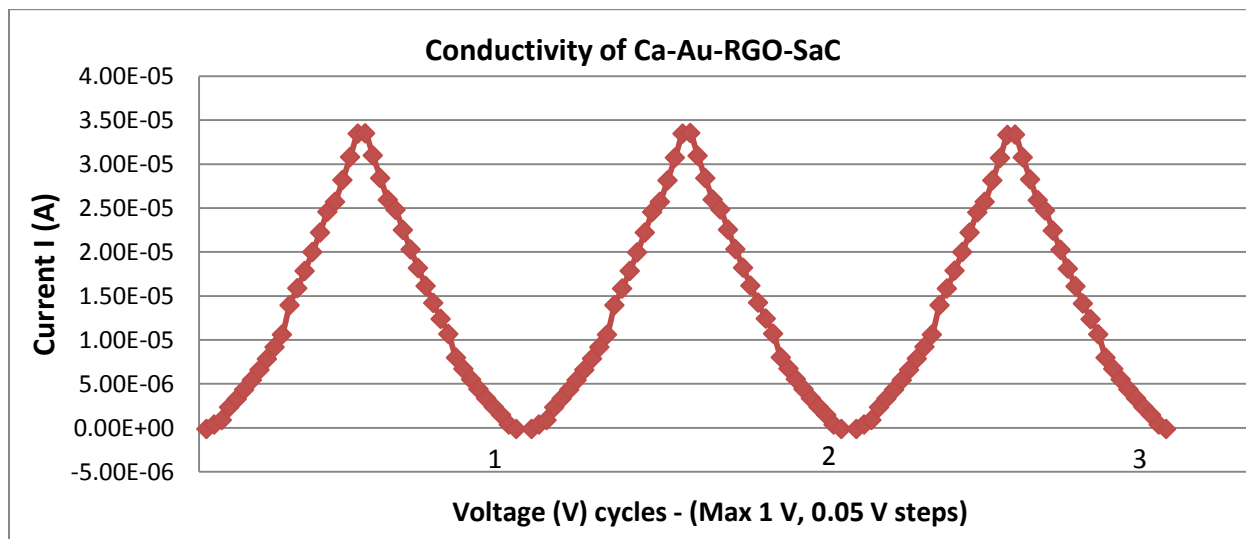
Figure 4-15: I-V plot for RGO-Ca-Au-SaC system.
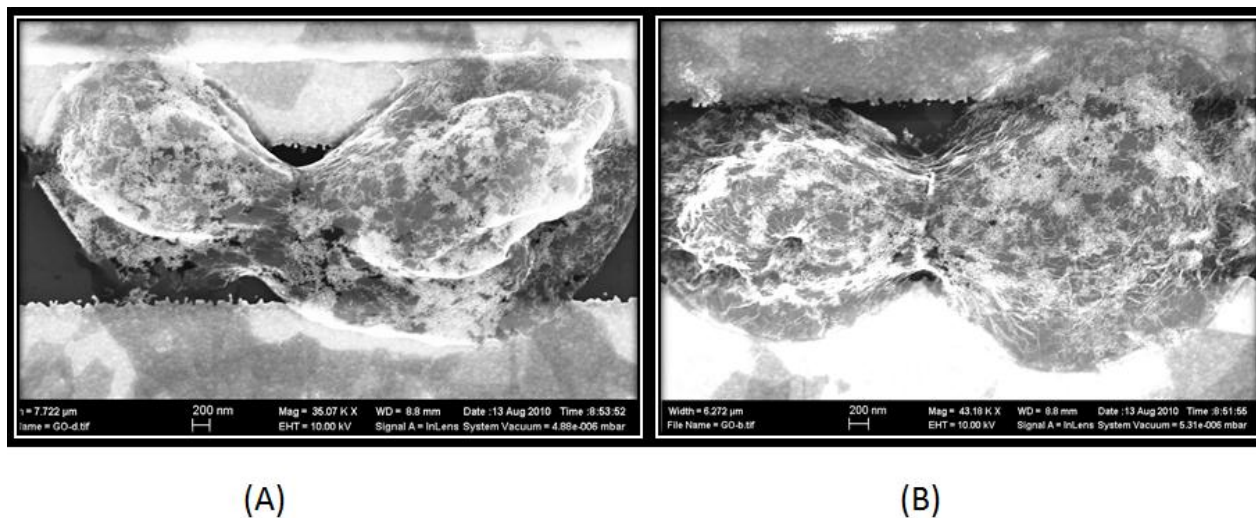
Figure 4-16: Enhanced deposition of RGO-Ca-Au-SaC on Au-chip.

Armed with a stable working system of RGO-Ca-Au-SaC, control experiments were tested to make sure that the currents were exclusively from the electronic interface i.e., RGO and it was verified by the I-V measurements of Ca-Au NPs deposited on a patterned Au-electrode chip compared against the I-V plots of plain SaCs on a patterned Au-electrode.

Plain SaCs did not demonstrate any conductive behavior supporting the fact that current (I) was a result of conduction in RGO (Figure 4-17).
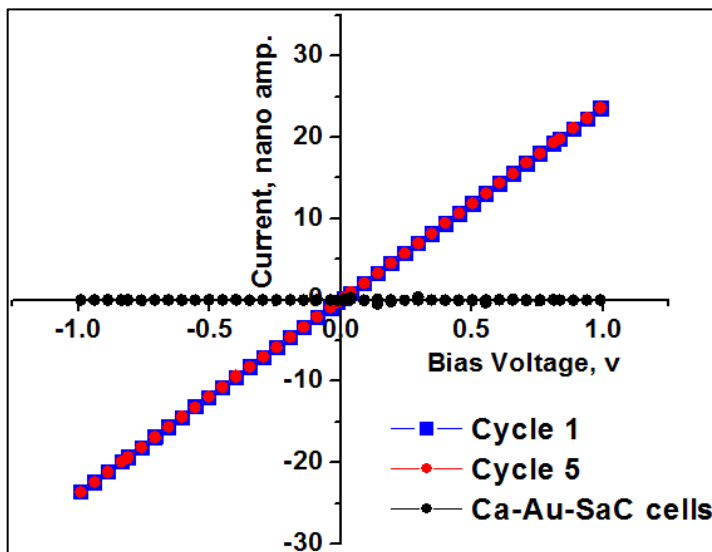
Figure 4-17: I-V characteristics of RGO-Ca-Au-SaC Vs plain SaC.

Negligible conductivity of Ca-Au-SaC can be credited to the insulating cell wall which is primarily made up of carbohydrates and the Ca-Au NPs on the surface do not form micron-long conducting pathways as seen in the Figure 4-18.
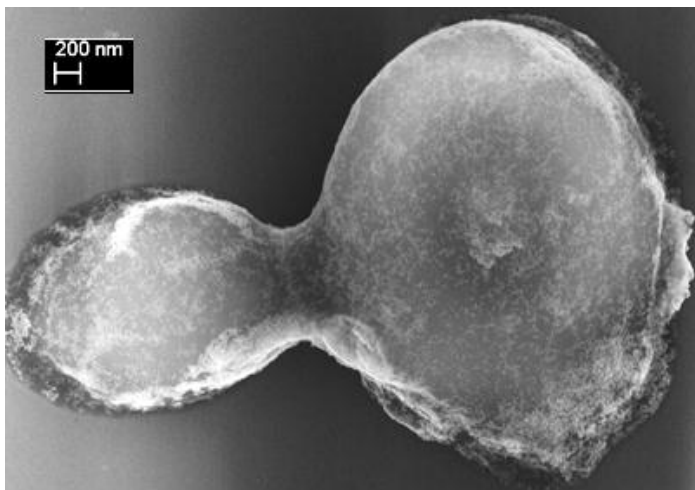
Figure 4-18: Ca-Au on SaC cell.

4.3 Electromechanical Coupling Results and Discussion

Electromechanical coupling was essentially observed when the cells in the RGO-Ca-Au-SaC system were physiologically stressed by exposure to alcohols such as ethanol and 2-propanol. Initially, I-V characteristics of the aforementioned system were studied and a voltage of 100 mV was found to be an optimal bias voltage generating currents with a few tens of nano-amperes (nA) in the system. Cells were exposed to ethanol (20 μL) for 3 minutes (to avoid permanent damage) and it was observed that conductance of the system decreases before regaining the shape and magnitude. This reversible subsiding of currents is chiefly because of the change in the conductivity of the RGO sheets that are affected by the physiological changes of the cells upon which they are encapsulated.[68]

4.3.1 Exposure to Ethanol

SaC cells show a decrease in the cell volume and increase in the cell surface roughness on exposure to alcohols. Since RGO sheets are well coupled to SaC cells, the cellular response i.e., shrinkage in volume and augmentation of surface roughness induces compressive stresses on the RGO sheets thereby inducing folds and ripples on the surface of RGO sheets. Surface corrugation generated by cellular modifications enhances the scattering of charge carriers on the surface and thus the reduced conductivity as illustrated in the Figure 4-19.[69]
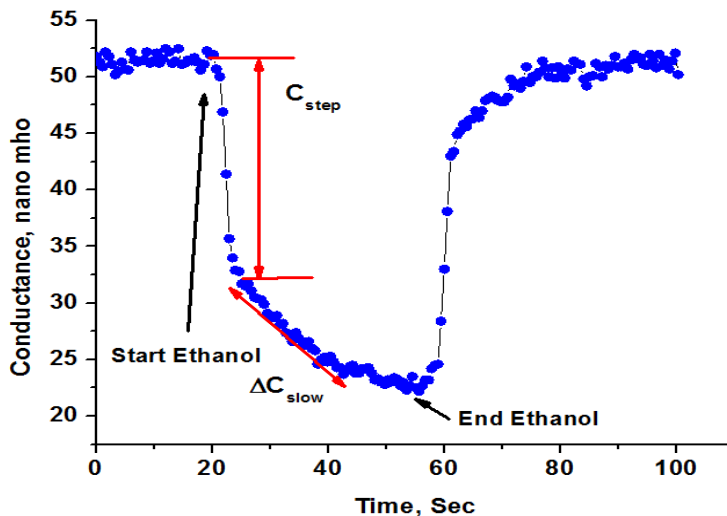
Figure 4-19: Change in conductance on exposure to ethanol.

Change in the conductance of the RGO-Ca-Au-SaC system on exposure to ethanol as described in the Figure 4-19 is a two-step process, first there is an immediate decline (C_{step}, %) in the magnitude of the conductance of RGO sheets and the second step is of a lesser gradient with a gradual rate of decrease of current (ΔC_{slow}, mho/sec). The conductivity of the RGO-Ca-Au-SaC system generally is 2 to 3 orders of magnitude higher than plain GO-Ca-Au-SaC system as described in the Figure 4-20
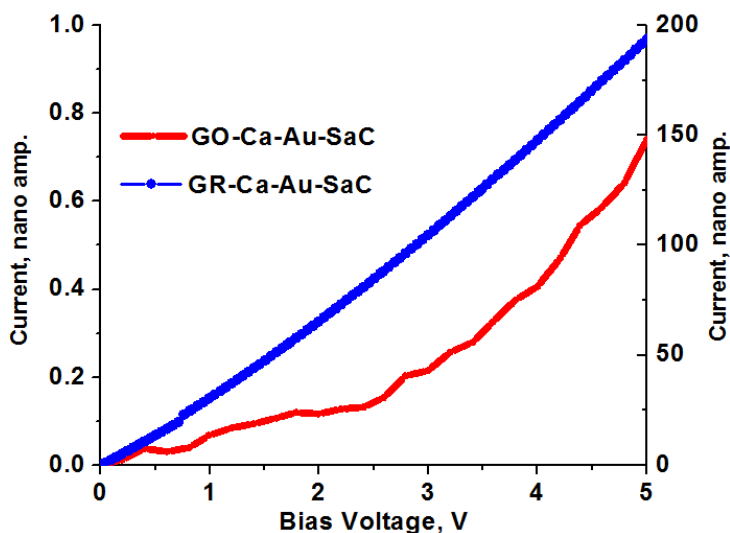
Figure 4-20: Comparison of conductivity: RGO-Ca-Au-SaC and GO-Ca-Au-SaC.

4.3.2 Control Experiments for Electromechanical Coupling

To validate the observed behavior we did test a control sample that had just RGO-Ca-Au on Au-chips by exposing them to ethanol; we observed that RGO-Ca-Au sheets do not show the same two-step gradient trend in their I-V plots, as shown in Figure 4-21. It proves that the effect observed in RGO-Ca-Au-SaC system is not due to the interaction between the graphene and the alcohol.

We also wanted to confirm that the behavior of RGO-Ca-Au-SaC is not due to the dielectric effects of the aqueous medium or the contact resistance of the RGO sheets. To investigate this detail we exposed the RGO-Ca-Au-SaC system to two aqueous solutions of similar dielectric strength. We exposed the RGO-Ca-Au-SaC system to 1M KCl and YPD nutrient broth that have their conductivity in the range of 1550 μS/cm. The hyperosmotic stress induced by 1M KCl causes the conductivity to drop, while the nutrient YPD broth causes the currents to go higher slightly confirming the previously inferred observation.[63]
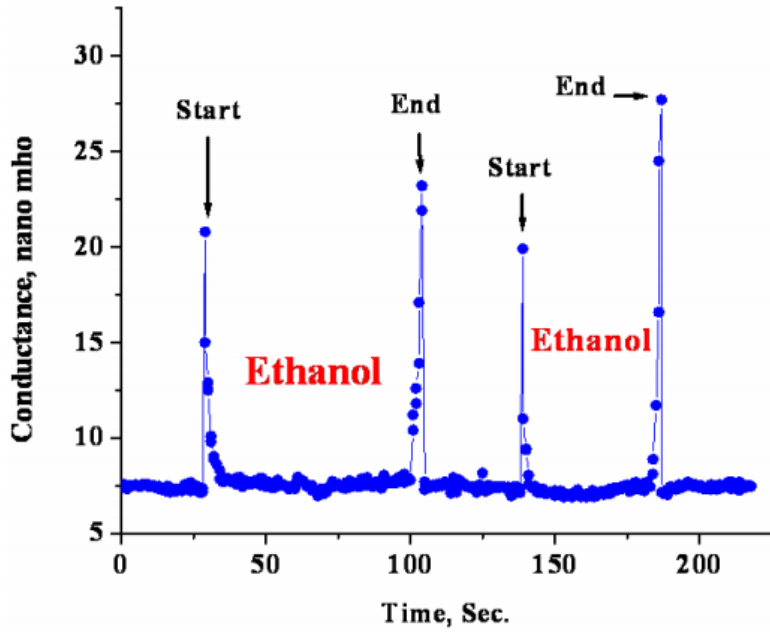
Figure 4-21: Ethanol on RGO-Ca-Au.

The Figure 4-22 shows the effect of 1M KCl and YPD on RGO-Ca-Au-SaC system.
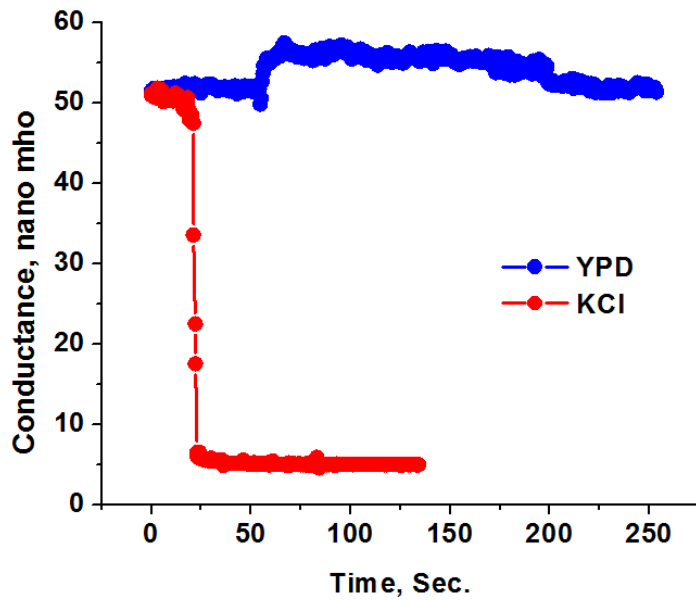
Figure 4-22: Effect of YPD and KCl on RGO-Ca-Au-SaC.

Further examination of RGO-Ca-Au-SaC system was done by exposing it to alcohols of various concentrations (99%, 90%, 80%, 70%, and 60% by volume). We noticed that the observed initial step decrease in conductivity (C_{step}), becomes larger in magnitude with increase in the water content of the alcohols. This effect has been illustrated in the Figure 4-23.
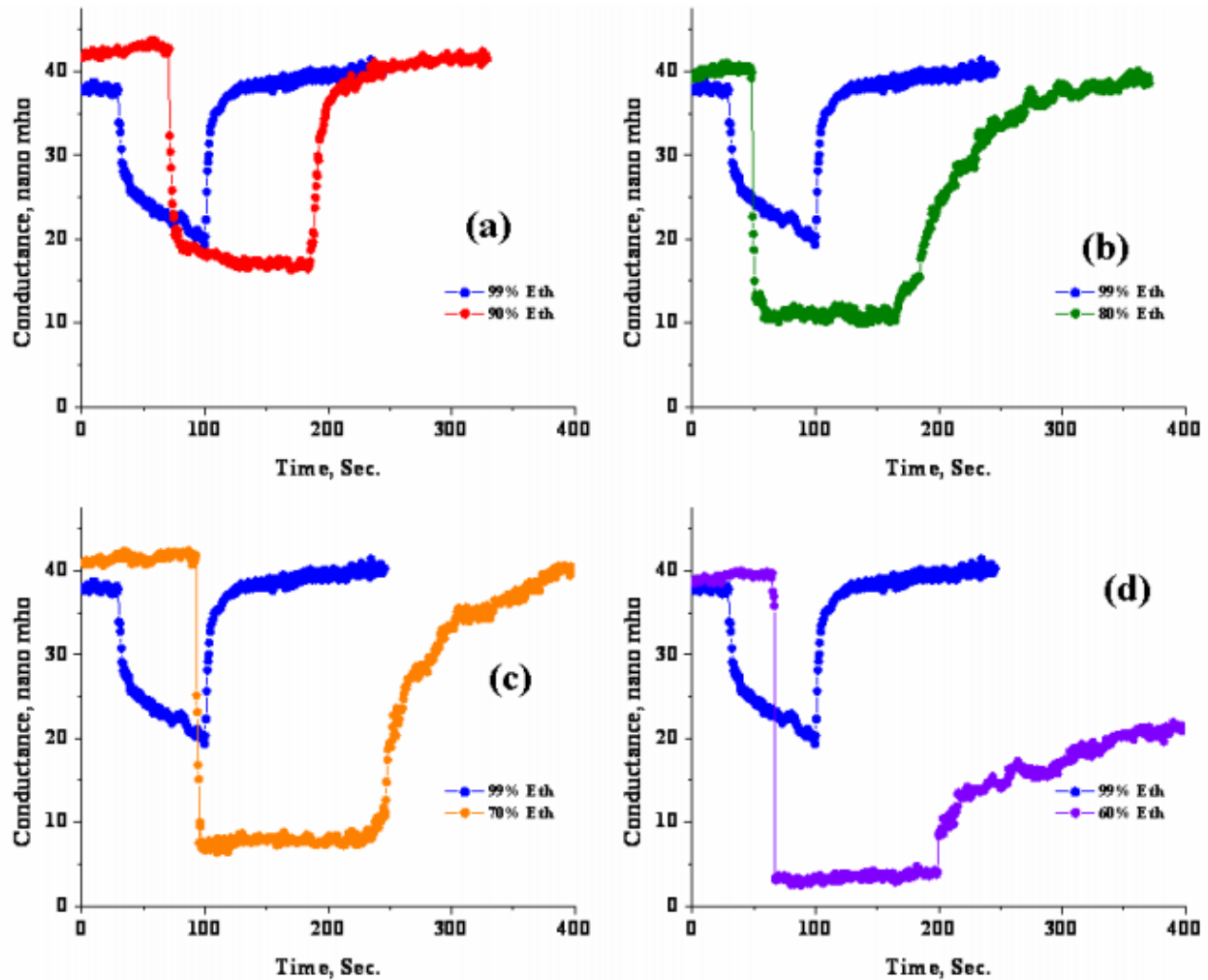
Figure 4-23: Dynamic response of RGO-Ca-Au-SaC on exposure to alcohols of varying concentrations.

Irreversible change in conductivity is observed when the RGO–Ca–Au-SaC cell is exposed to 60% ethanol solution, implying a permanent change to the cell morphology. This signifies that 60% v/v fraction of ethanol is most effective in penetrating the cell (Figure 4-24).

48
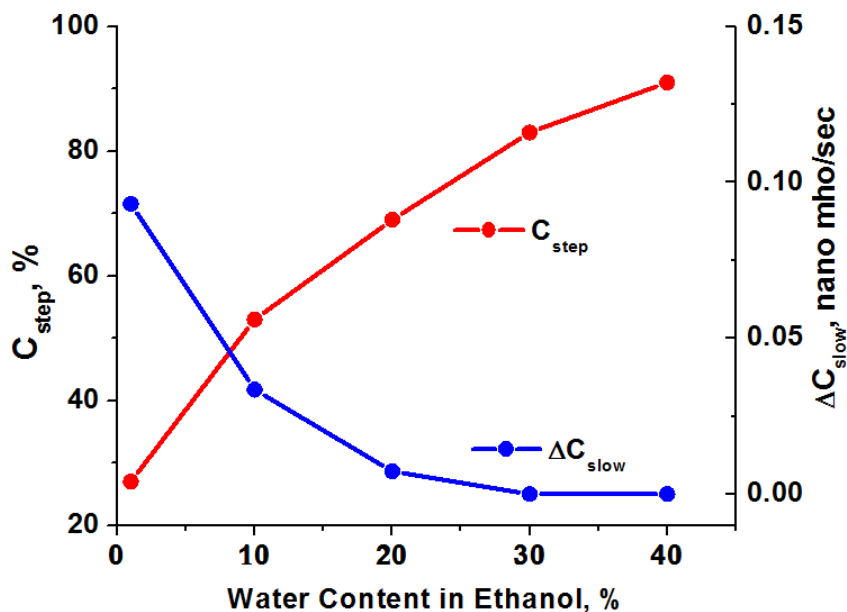
Figure 4-24: Dynamic response on exposure to ethanol as characterized by C_{step} and ΔC_{slow} values.

The initial (C_{step}) observed in the dynamic response could be because of the penetration of alcohol into the cell wall rendering the morphology altered (folds, wrinkles) and the more gradual response (ΔC_{slow}) arises out of the trailed penetration of hydrophobic content of the alcohol into cells. The permanent change in the morphology of the cell surface and immediate penetration into the cells by 60% v/v ethanol corroborates with its common use as antiseptic agent. The surface area of RGO sheets exposed to varied concentrations of ethanol were identical.[70]

4.3.3 Exposure to 2-propanol

The RGO-Ca-Au-SaC system was exposed to 2-propanol to understand the behavior for a different ambient setting around the cells. The amount of 2-propanol exposed to the cells was kept at 20μL and the duration of exposure was set at 3 minutes to restrict the probable damage to the cells. 2-propanol (90%) reduces the initial step decrease in conductivity i.e., C_{step}. The gradual decrease, ΔC_{slow} of the conductivity becomes significant with the increasing hydrophobic nature of the solution (Figure 4-25). As a result, we inferred that increasing the hydrophilic content increases the initial C_{step} and the increase in hydrophobic content of the alcohol increases the slower response i.e., ΔC_{slow}. Figure 4-26 illustrates the inferred reasoning.

49
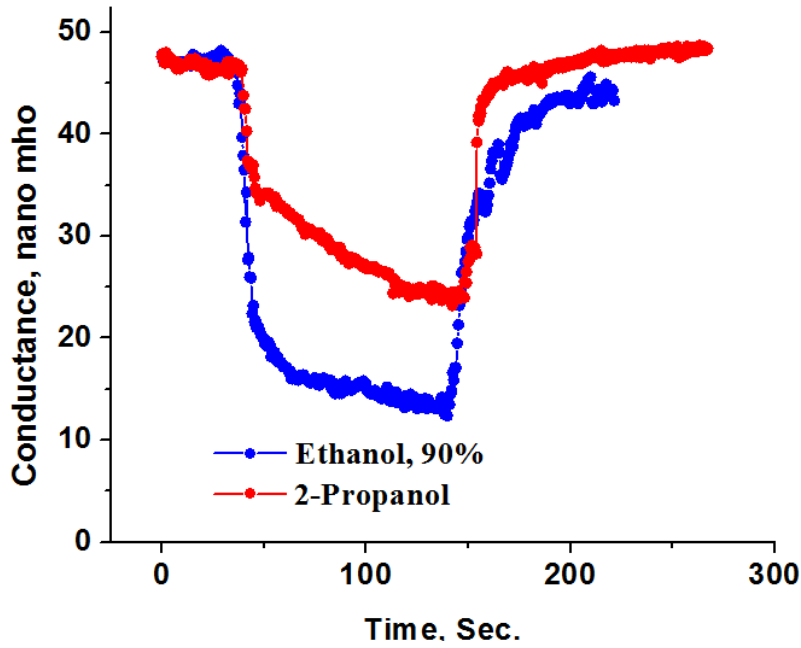
Figure 4-25: Comparison of behavior of the RGO-Ca-Au-SaC system upon exposure to ethanol and 2-propanol.
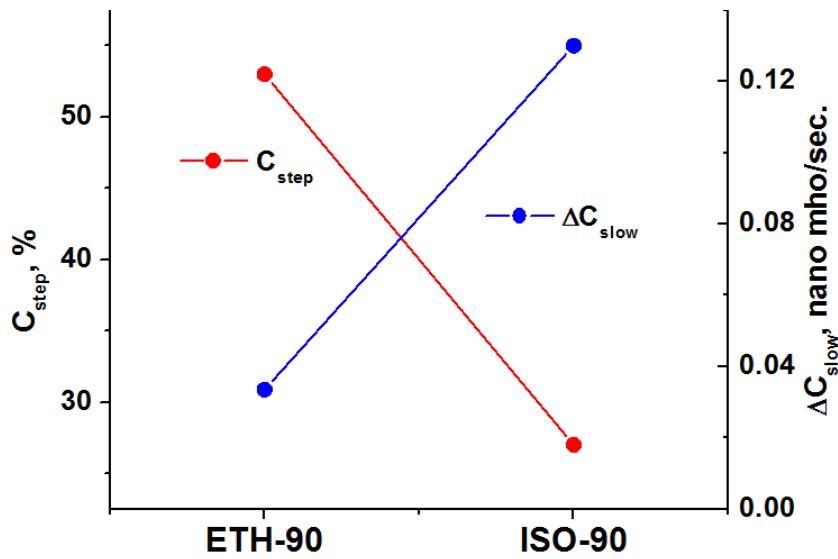
Figure 4-26: Plot indicating the effect of hydrophobic and hydrophilic content of the alcohols on cells.

4.3.4 FESEM and AFM Analysis of Cellular Modifications

The changes on the surface of SaC cells as a consequence of exposure to alcohols were studied using FESEM and characterized using AFM analysis of the data. For the purpose of FESEM analysis, RGO-Ca-Au-SaC deposited on a patterned Au-chip was chosen and the cell with RGO sheets resting across the electrodes was selected for a time-based e-beam exposure study that simulates the same kind of effect on the RGO sheets as done by alcohol exposure of SaC cells.
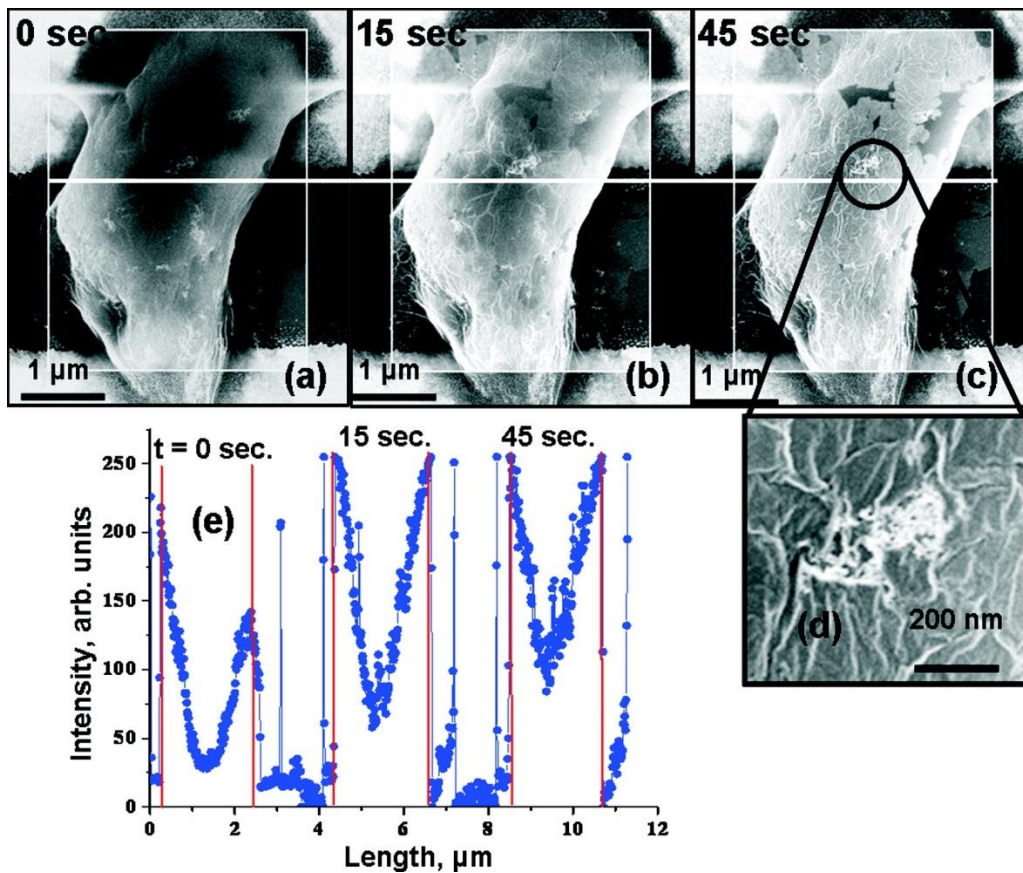
Figure 4-27: Shrinkage in the cell volume as a result of e-beam exposure.

Exposure to the electron beam in FESEM, similar to a heat shock, leads to a decrease in cell volume wrinkling the RGO sheets on the yeast cells. Snapshots of the RGO–Ca–Au-SaC at progressive exposure times are presented in Figure 4-27, 0 s (a), 15 s (b), and 45 s (c), clearly show the effect. (d) A magnified view of the cell surface shows the wrinkles in the RGO sheet. (e) The intensity plot of the line in panels a, b, and c shows that the lateral cell dimension decreases due to e-beam exposure.

51

The cell volume shrinks with exposure, and the RGO sheets on the surface start to wrinkle. The cell shrinkage as calculated from the line scan shown in Figure 4-27 leads to lateral strains of 4.4% and 7.8% after 15 and 45 s exposure. This lays the basis for the observed decrease in the current on exposing the RGO–Ca–Au-SaC to alcohol. Also optical images of SaC cells before and after exposure to 70% v/v ethanol for 10 minutes show the decrease in cells volume.[71]
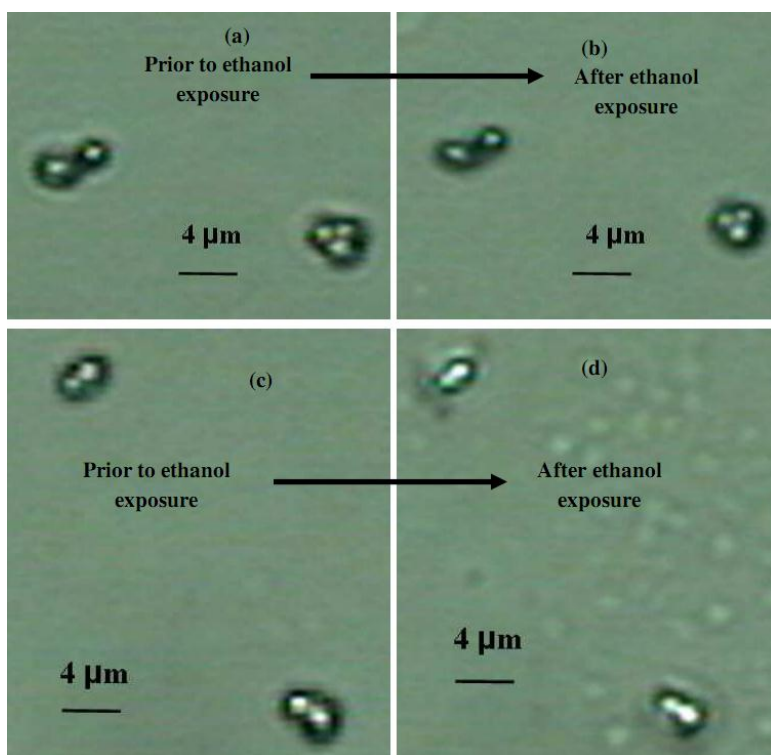
Figure 4-28: (a) and (c) Prior to ethanol exposure, (b) and (d) after exposing to 70% v/v ethanol for 10 minutes.

An extensive AFM analysis was done to study the surface morphology of cells exposed to ethanol and AFM images clearly showed the wrinkles on the surface confirming the deformation of RGO sheets due to stress generated by the electromechanical coupling with the cellular surface. Unexposed cells have a smooth surface with surface roughness of less than 2 nm. Figure 4-29 shows an AFM image of RGO-Ca-Au-SaC cells on a patterned gold electrode. It is a 2-bud cell resting across the electrodes, an inset elucidates on the magnified surface features like wrinkling and folds.
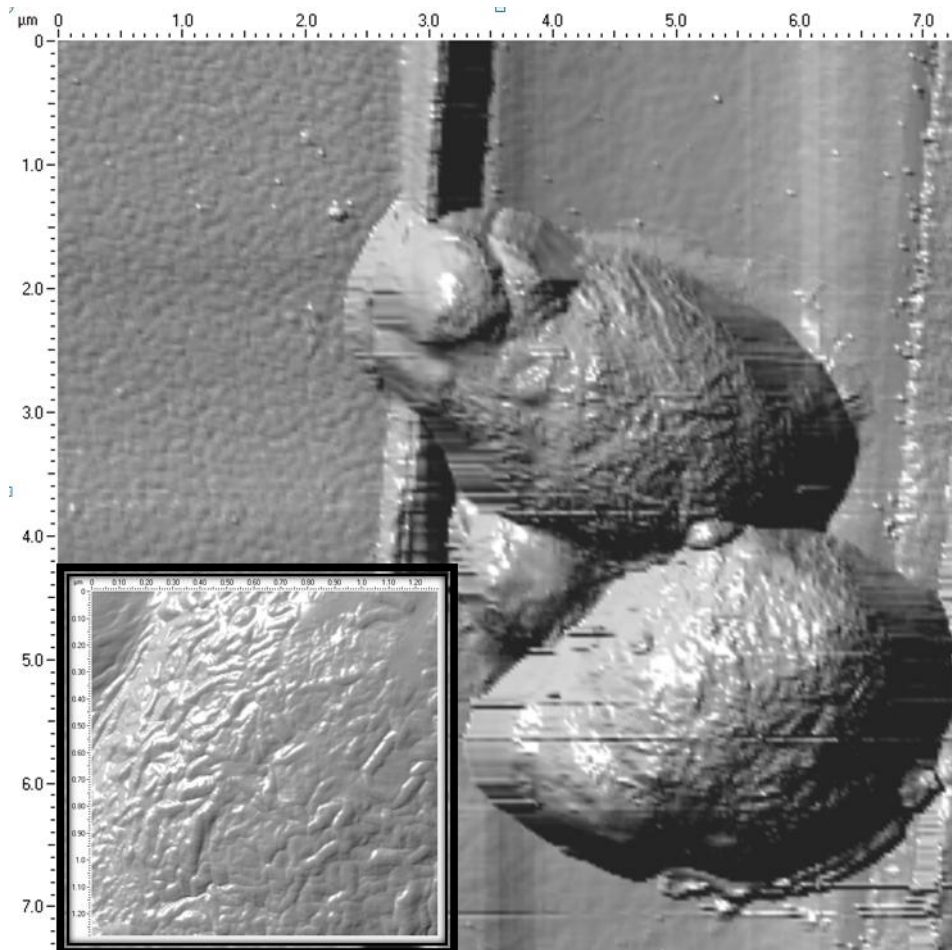
Figure 4-29: AFM image of RGO-Ca-Au-SaC on Au-electrode.

The RGO sheets can be compared to graphene sheets in terms thickness (a few nanometers) and elastic modulus (~1 TPa). Due to their nano-scale thickness, they buckle under compressive stresses leading to the formation of surface undulations. A 15% decrease in the cell volume due to 5% strain in the lateral dimensions will lead to stresses on the order of 22.5 MPa (bulk modulus of cell wall is taken as 150 MPa). The height of the wrinkles is ~14 nm as calculated to these stresses by taking the sheets as 500 nm squares with a thickness of 1.5 nm (see Appendix B). This value matches with the observed size of deformation on the cell surfaces by AFM analysis $\approx$ 10-25 nm. The detailed AFM-Height image of surface undulations (images are 1.3 μm square) on the cell surface is shown in the Figure 4-30, (A) Phase image, (B) height image of the curvature of the cell on the electrodes with the vertical scale measuring

53

760 nm and the horizontal scale measuring 1.6 μm. (C) and (D) illustrates the magnified profile along the lines drawn as shown in (A) revealing the height of surface undulations (10-25 nm). The horizontal scales for (C) and (D) are 27 nm and 33 nm while the vertical scales are 290 nm and 350 nm. [71, 72]
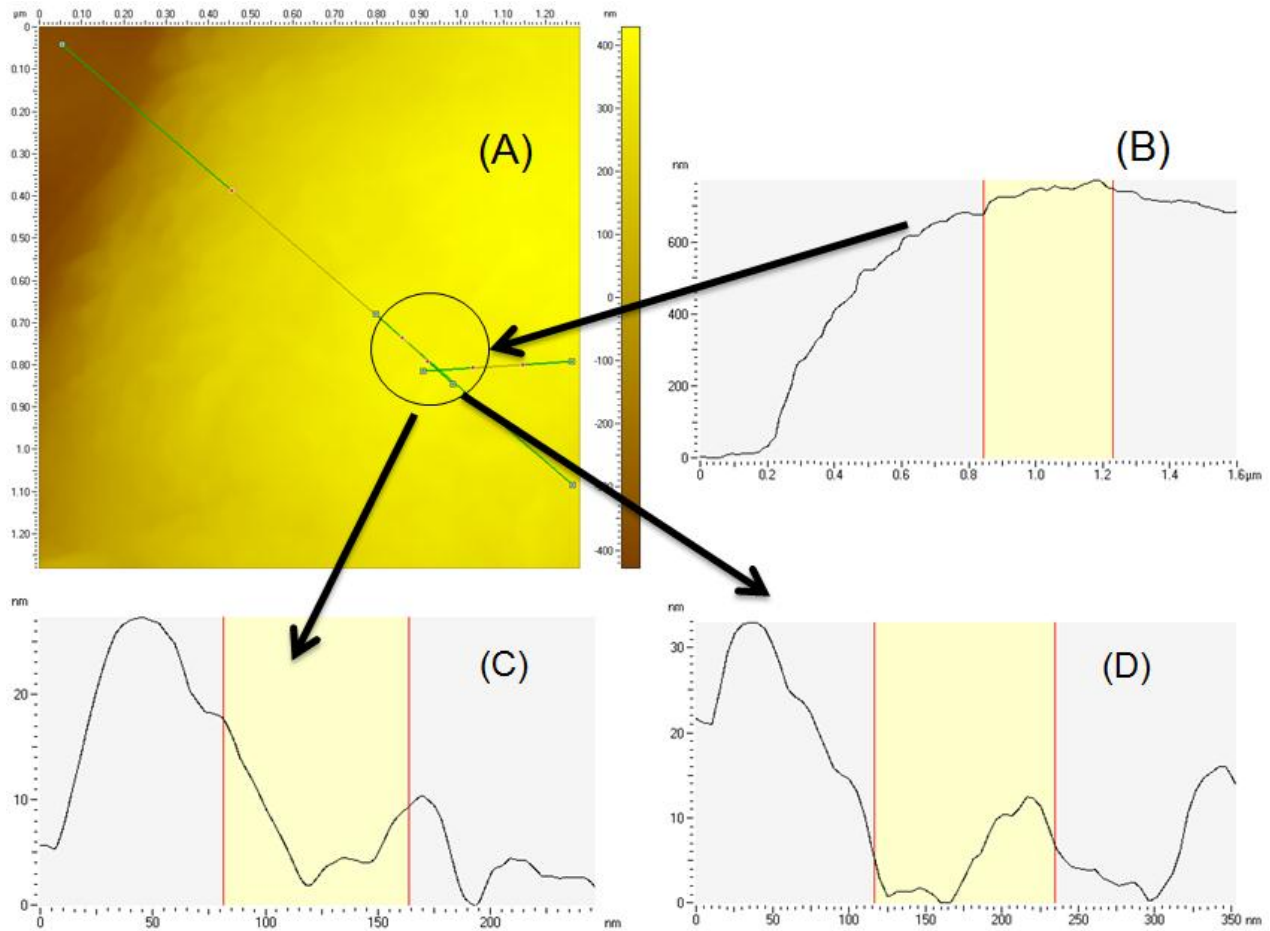
Figure 4-30: AFM- Phase and Height imagse of the surface undulations.

Electromechanical coupling was thus demonstrated on the RGO-Ca-Au-SaC system using the above-mentioned characterization techniques and it was imperative to study the condition of the SaC cells after the coupling has been done; Live/Dead test was performed to interpret biological vitality of these cells.

4.3.5 Live/Dead Test

The viability of the yeast cells after the deposition with RGO-Ca-Au was studied using a Molecular probes® L-7009 LIVE/DEAD® Yeast Viability Kit (Invitrogen™). The kit consists of two-colored fluorescent probes, FUN® 1 which stains the cell body, and with a fluorescent fungal surface labeling reagent Calcofluor™ White M2R. We mixed 260.3 mg of HEPES powder in 100 mL of Millipore™ water to get 10 mM of Na-HEPES buffer; 2 g of glucose was added to HEPES buffer and the resultant solution was used as the medium (GH solution) for staining the cells with the dye reagent. 3 mL of 10 μM and 2 mL of 60 μm FUN 1 reagent solutions were prepared by mixing the stock 10 mM dimethylsulfoxide (DMSO) cell stain into sterile GH solution. Saccharomyces Cerevisiae (yeast cells) were grown in YPD broth for 8 hours, centrifuged and washed 2 times before mixing it with the RGO-Ca-Au solution that was prepared as described in the previous section 4.2.5. After incubating for an hour, the solution was centrifuged and re-suspended in GH solution. RGO-Ca-Au-SaC cells in GH solution were finally stained with FUN 1 reagent solutions (10 μM and 60 μM) by mixing it in the ratio 50:50. 5 μL of 25 μm Calcofluor solution prepared from its 5μm stock solution was added and the fluorescence emission spectrums (500-700 nm) from each of FUN 1 dye-stained yeast suspension were recorded using excitation wavelength at ~470 nm on a confocal microscope. The ratio of color change from green to red signifies the aliveness of yeast cells. Similar procedure was used on a plain yeast suspension that was used as a control solution and RGO sheets coupled with Ca-Au.
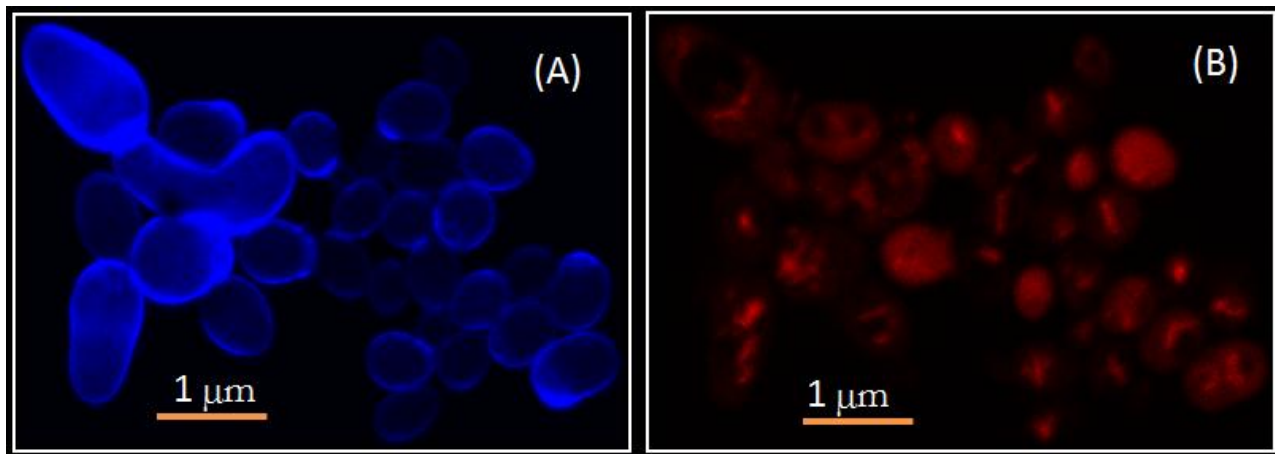
Figure 4-31: Fluorescence from the cells upon staining with FUN 1.

Staining of the RGO-Ca-Au-SaC with FUN 1 and Calcofluor dye results in blue fluorescence from the cell wall (due to Calcofluor) and a red emission from FUN 1 that is localized in vacuoles inside the cells. Figure 4-31 shows 3-D stacked confocal microscopy images of cells incubated with FUN 1dye. A blue color show that the cells are metabolically active with plasma membrane intact and the red color shows the permeated FUN 1 dye inside vacuoles. To eliminate the plausible effect of RGO sheets in fluorescence, we extended a few control experiments where plain RGO-Ca-Au solution was stained with FUN 1 dye and the fluorescence emission was recorded. We found that there is a minimal change in the fluorescence spectrum of the FUN 1 dye after incubating it with RGO-Ca-Au (Figure 4-32).
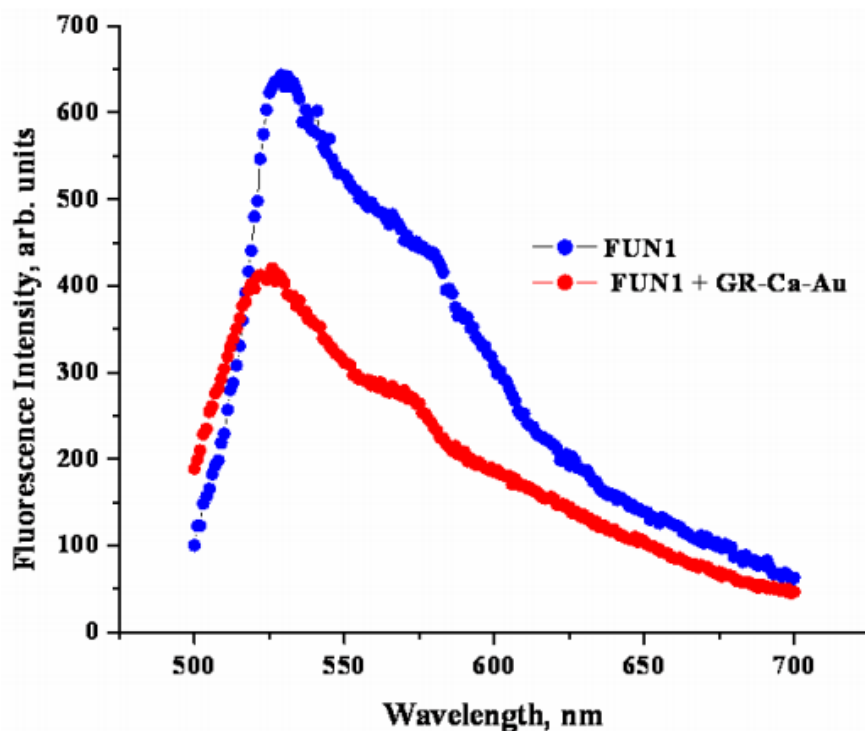
Figure 4-32: Fluorescence emission of plain FUN 1 dye and FUN 1 incubated with RGO-Ca-Au.

Both plain FUN 1 dye solution and FUN 1 incubated RGO-Ca-Au solution shows the characteristic emission at $\sim$ 520 nm (green) and a shoulder at $\sim$ 570 nm. No shift in fluorescence is observed for the dye on incubation with RGO-Ca-Au solution. The primary effect is only in the reduction of fluorescence intensity. This is a common phenomenon observed in graphene sheets where the absorbance of dye molecules on the sheets leads to quenching.[73]

4.3.6 Graphene as a Protective Skin

Cell wall is an organic layer encapsulating the bacteria or yeast cells and is permeable to allow exchange of substance with the surroundings. Cell wall plays a vital role in the protection of the innards of the cell and acts as scaffolding for the structure to hold together. However, it does little towards guarding the cells against harsh environments. Encapsulation of the cell with inorganic mineral shell has been found to enhance the robustness of the cell and improve the performance of cell based sensors in harsh environments. Shells of silica, calcium phosphate and polyelectrolytes as encapsulating material have shown to enhance the cell stability. However, these materials do not offer intrinsic electrical properties that would be useful for making functional nano-devices. We demonstrate that encapsulating SaC with graphene sheets (Figure 4-33). The RGO sheets cover over and across the cell surface and this affords electrical conductivity across the cell surface as described previously and shown in FESEM results.

1. The partial coverage of the RGO sheets allows the cells to maintain their dynamic exchange of substance with the surroundings.

2. The high mechanical modulus of the RGO sheets leads to enhanced protection of the cells against osmotic stresses thereby improving their stability.
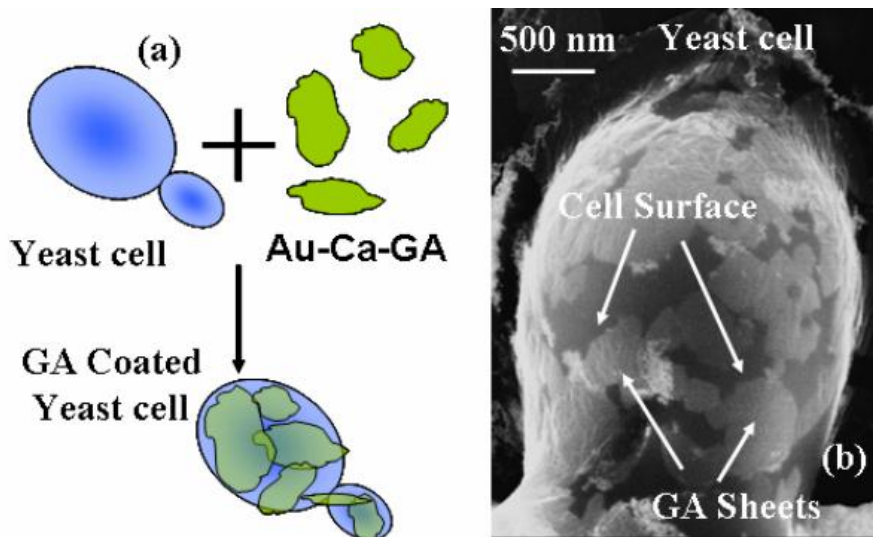
Figure 4-33: (a)Encapsulating graphene sheets with cells , (b) FESEM image of graphene sheets on the cell.

The advantage of encapsulating RGO sheets on GO is that cells can be imaged using FESEM without any charging effect as they have conductive pathways on the surface that are electron rich. In contrast, plain SaC cells appear as dark spots in FESEM as they are made up of organic matter. Further irradiation of e-beam in FESEM under high vacuum ($1.5\,E-05\,mbar$), the SaC cells shriveled, leading to the wrinkling of encapsulating RGO sheets. The line scan of the cells in Figure 4-34 (b) and (c) shown in (d) illustrates the formation of the wrinkles on the sheets. The wrinkles appear brighter upon e-beam radiation as they scatter more electrons. The persistent gaps seen in the Figure 4-34 (c) also confirms the sponginess of the RGO sheets allowing dynamic mass exchange.[74]
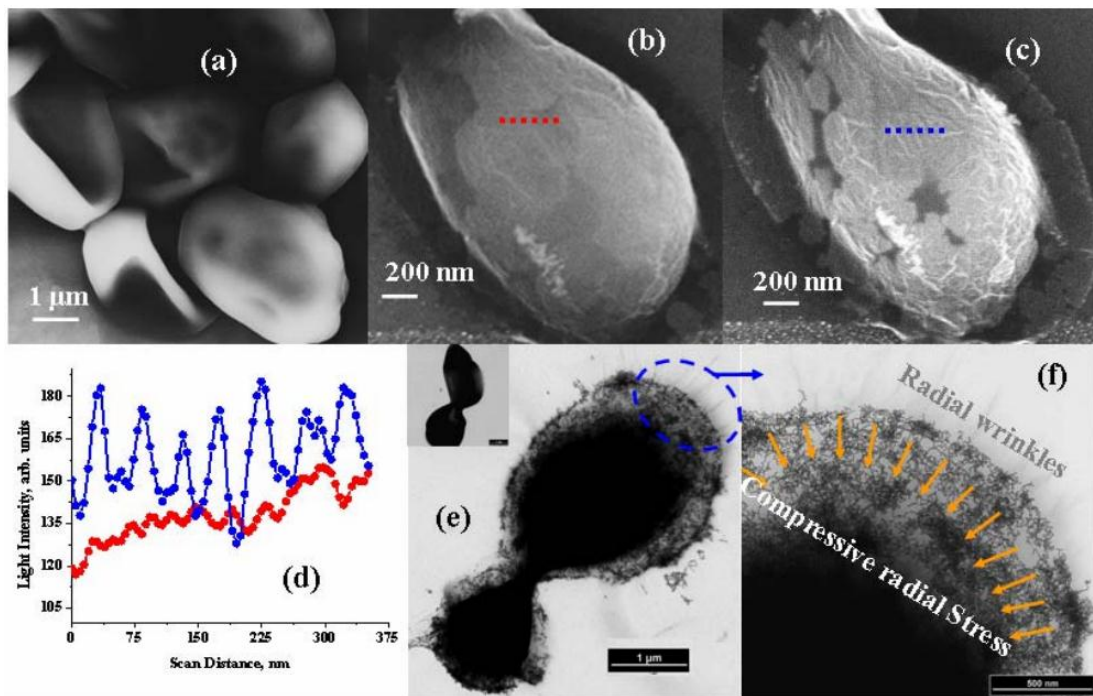
Figure 4-34: (a) Plain SaC cells appear shriveled and without any surface features in FESEM. (b) SaC cell with RGO sheets as seen in FESEM. (c) After 3 min in FESEM limited shrinkage is observed in the SaC cells, leading to wrinkles on the RGO sheets. (d) The line scan on the surface of the cells marked in b&c shows that the wavelength of the wrinkles is ~ 40-70nm. (e) The RGO-SaC cell can also be imaged under TEM. The inset shows a plain SaC cell that shrivels in the high vacuum and energy of the e-beam. (f) Due to limited shrinkage of the cell, the GA sheets at the interface of the cell and the substrate show radial wrinkles.

From the line scan shown in Figure 4-34 (d), the wavelength of the wrinkles is calculated as ~ 40-70 nm. Further from the TEM image (Figure 4-34 (f)) it is observed that at the boundary of the cell the wrinkles in the RGO sheets are radial (orthogonal to free boundary) due to reduction in cell volume. This is similar to wrinkling of the apple skin on drying, where the thin high modulus apple skin covers the softer apple fruit substrate. The viability of the SaC cells after encapsulation by the RGO-Ca sheets is illustrated by Live/dead test as described in the section 4.3.5.
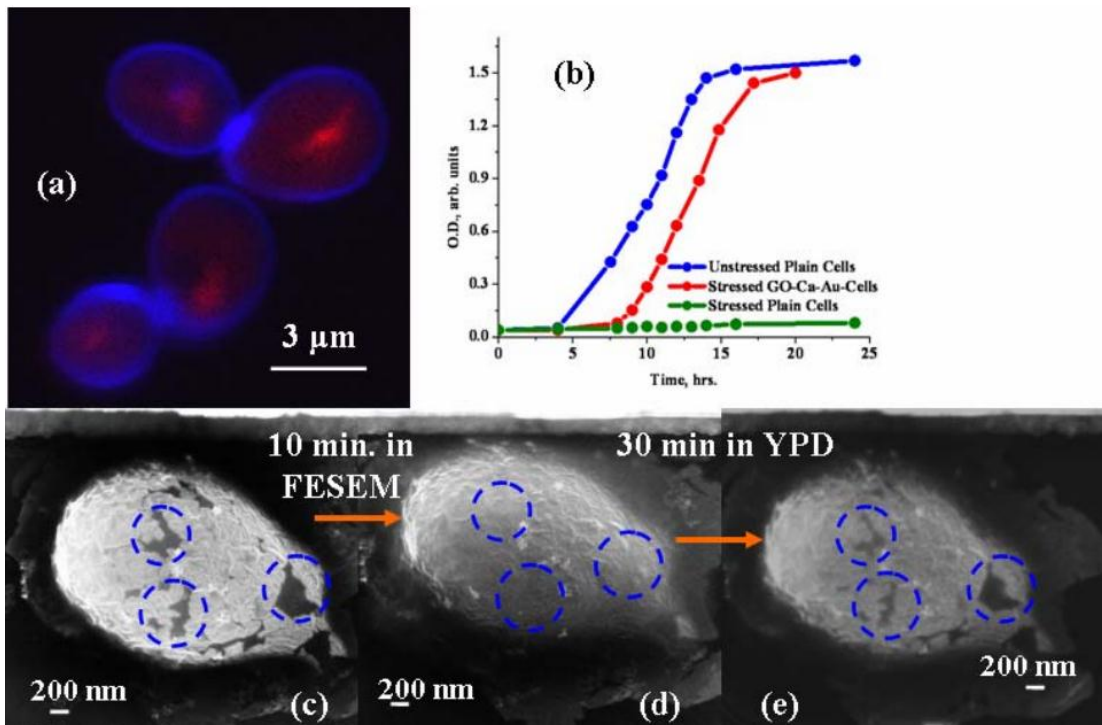
Figure 4-35: (a) and (b) Metabolic activity of the cells, (c), (d) and (e) relaxation of RGO sheets on Cell surface.

As seen in Figure 4-35 (a), the RGO-Ca-SaC cells show red fluorescence, hence they remain metabolically active. It also illustrates that the dye is able to diffuse into the cell, indicating mass transfer with the surroundings. If the RGO sheets augment the mechanical strength of the cell, it should lead to increased cell stability on exposure to osmotic stresses which cause a change in cell volume. To confirm this both plain SaC cells and RGO-Ca-SaC were stressed by suspending them in pure water for 7 days at 10℃. {Figure 4-35 (b)} shows the growth curve of the SaC cells. Plain, unstressed SaC cells have a lag

phase of ~ 2-4 hrs, after which they proliferate rapidly. In comparison, the RGO-Ca-cells show an increased lag phase of ~ 8hrs, after which they proliferate rapidly. The stressed plain SaC cells fail to grow even after 24 hours. This demonstrates an increased stability of the RGO-Ca-cells to osmotic stresses. The decrease in cell volume on exposure to the extreme conditions in FESEM leads to straining of the RGO sheets. Also due to the decrease in the volume the sheets become more closely spaced on the cell surface, Figure 4-35 (c) and (d). Initially after 3 minutes in FESEM the RGO-Ca-cell shows open spaces between the RGO sheets on the cell surface {Figure 4-35(c)}. After, another 10 minutes in the high vacuum of FESEM (10^{-6} mbar) the reduction in the cell volume leads to shrinking of the gaps between the sheets {Figure 4-35 (d)}. The effect is reversed on placing the cell in the nutrient broth YPD for 30 minutes. As observed in the FESEM image of Figure 4-35 (e), the RGO sheets relax and the open spaces between the sheets reappear. The nutrient broth YPD replenishes the cell volume as both water and the nutrients in the broth are able to easily penetrate into the cell through the cell wall and the plasma membrane. This illustrates that the effect on RGO sheets is reversible and is linked to the state of the cell. The cell volume changes under both kind of osmotic stresses (hyper and hypo) and this will induce strain in the RGO sheets on the cell surface. Hence the cells are constrained by the RGO sheets that restrict their change in volume and increase their stability.

Chapter 5

Anticipated Future Work

The occurrence of magnetism in carbon-based materials possessing the sp^2 network has been a subject of debate and is still not resolved. Exceptional electronic and mechanical properties combined with noticeable ferromagnetism at room temperature of graphene provide a challenging and potential platform for future applications. Fe, Co and Fe based alloys show superior magnetic properties with high saturation magnetization, their fine particles are easily oxidized preventing them from further processing. Iron nanoparticles (superparamagnetic iron oxide nanoparticles, SPIONS) as potential magnetic carriers have been studied extensively. Synthesizing the Fe nanoparticles on ultra-thin layers of graphene not only enables superior magnetism, wide energy gap opening and electrical conductivity; they can be coupled with suitable bio-compatible coatings that can be used in magnetic resonance imaging (MRI), tissue engineering, and drug delivery.[75] Here we synthesize iron oxide nanoparticles (Fe_3O_4) using wet chemical methods and encapsulate them in graphene oxide (GO) sheets and we found that these sheets are magnetic in solution.[76]

5.1 Synthesis of Iron Oxide Nanoparticles on GO

The first step towards encapsulating Fe_3O_4 on GO was to synthesize a stable solution of Fe_3O_4. This was carried out via controlled chemical coprecipitation method under basic aqueous conditions. Experimental setup consisted of a round bottomed flask that had 15 mL of GO (0.5m/mL) solution to which ferrous chloride tetrahydrate ($FeCl_2$ $4H_2O$, 198.81g/mol; sigma aldrich) and ferric chloride hexahydrate ($FeCl_3$ $6H_2O$, Mw 270.3 g/mol; sigma aldrich) mixed in 1:2 molar ratio. The flask was heated to 80℃ and the solution was stirred vigorously for 15 minutes. Ammonium hydroxide 25% (v/v) was added to the solution in the flask to precipitate Fe_3O_4. The solution was cooled and neutralized to attain a pH of ~7. The resulting solution was then deposited on a surface functionalized chip. We also found that the iron oxide particles are magnetic and they aggregate upon applying magnetic field (Figure 5-1). The solution was deposited on a surface functionalized silicon chip and FESEM analysis showed that Fe_3O_4 particles have sizes ~ 10-20 nm and well encapsulated on GO sheets. Figure 5-2 shows Fe_3O_4 particles as bright spots while the dark background is GO sheets.[77, 78]
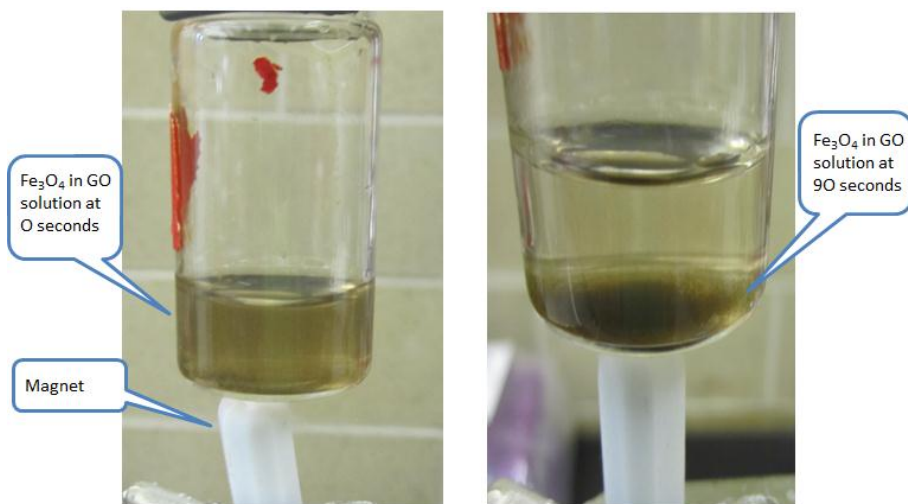
Figure 5-1: Synthesized Fe₃O₄ particles in Go solution show magnetic behavior.
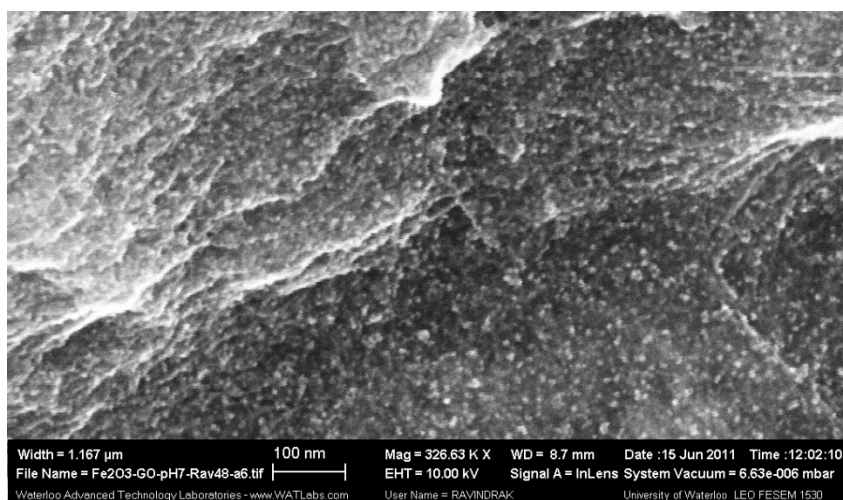
Figure 5-2: FESEM image of Fe₃O₄ on GO sheets.

Using the SaC cells as templating material for the deposition of Fe_3O_4 can be explored in greater detail. It is also possible to synthesize SPIONS on the surface of SaC cells and track the movement of cells in a solution or to tailor the movement of cells to a desired location. If the formation of SPIONS on cells can be successfully then it is possible to use them as a backpack for the targeted medicinal drug delivery.

Width = 2.681 µm 200 nm Mag = 142.18 K X WD = 8.3 mm Date :6 Jul 2011 Time :9:52:55
File Name = Ravi-Feo-chip56-a2.tif EHT = 10.00 kV Signal A = InLens System Vacuum = 4.86e-006 mbar
Waterloo Advanced Technology Laboratories - www.WATLabs.com User Name = SHEHAN University of Waterloo LEO FESEM 1530
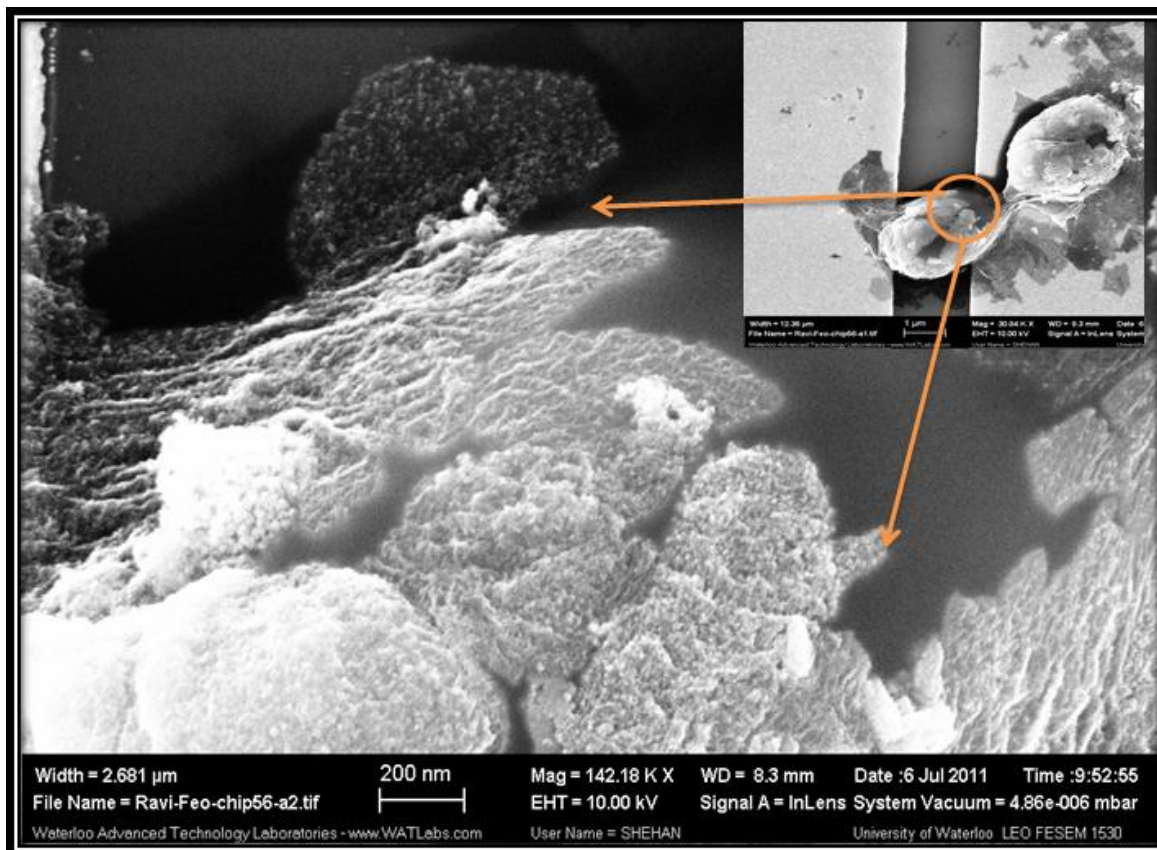
Figure 5-3: Magnified FESEM image of Fe3O4- GO on SaC surface, inset shows the whole cell.

The conductivity of RGO is chiefly influenced by the interaction between the substrate and the deposited sheets. SaC cells provide a neutral and versatile platform the deposition that can be manipulated.

We have also fabricated a new microfluidic cell that can house a patterned chip and it is being used to study the cellular processes like cell division, effect of pH on the conductivity and to study the feasibility of using yeast cells as a template for magnetic nanoparticle deposition.

Chapter 6

Conclusions

6.1 Conclusions

Several significant conclusions can be drawn from this work:

- Graphene oxide was easily synthesized using wet chemistry methods and the solution is stable over a wide range of temperatures. The GO monolayers were found to be 1.0 ± 0.5 nm thick.

- The conductivity in graphene oxide follows a variable range hopping model, it increases with temperature and highly dependent on the graphene-substrate interface.

- Hydrazine reduction of GO is effective, increase in conductivity can be of the order of 10^2-10^4 times but the reduction process can render the GO heavily doped and slightly toxic.

- Since RGO sheets are impermeable membranes, for cells lacking the cell wall, the degree of deposition can be controlled by use of sheets with well-defined size and concentration.

- Ca-Au self-assembled nanoparticles can bind with GO and yeast cells very well.

- GO can bind to SaC with the assistance of Ca-Au forming conductive sheets on the surface. The changes that happen to the cell can be perceived with the change in conductivity of the system.

- Electromechanical coupling of SaC cells with GO sheets was observed when the cells were exposed to alcohols. The cells experience osmotic shock and begin to shrink in volume. The surface morphology changes forcing the encapsulating GO layers to wrinkle and thereby changing the conductivity of the GO sheets.

- 5% lateral strain or 15% shrinkage in the volume of the cells due to osmotic shock can generate stresses in the range ~22.5 MPa.

- High mechanical modulus of RGO-Ca sheets on SaC cells can act as a protective skin enhancing the robustness of the cells yet leaving them viable for dynamic exchange of matter with the surroundings.

- The application of GO as a protective covering or electrical interface can be replicated for other mammalian cells or nano-bio material.

Safety Considerations

All safety precautions will be taken when performing the experiments outlined in this proposal. Good laboratory practice will be followed, and appropriate safety goggles, gloves, and clothing will be worn as required. Prior to the use and handling of chemicals, MSDS sheets will be reviewed. Chemicals will be disposed of in a proper manner. Extra caution will be taken when working with hydrazine. According to the hydrazine MSDS, this chemical may be fatal if swallowed, inhaled or absorbed through the skin. This chemical will therefore be handled in a well-ventilated fume hood, using appropriate eye and skin protection gear.

Caution will also be taken when working with sulphuric acid, sodium hydroxide and hydrochloric acid. These three chemicals are poisonous and corrosive. Therefore, they will be handled in a fume hood, using appropriate eye and skin protection. And finally, considerable caution will be taken while dealing with yeast cells. In particular, much caution will be required when working with piranha solution. This material is highly corrosive, dangerous to skin, and highly toxic by inhalation. As such, hydrazine and sulphuric acid will be carefully handled in a fume hood using appropriate protective equipment.

References

1. Wallace, P. R. *Phys. Rev.* **71**, 476 (1947).

2. Geim, A. K. & Novoselov, K. S. The rise of graphene. *Nature Materials* **6**, 183-191 (2007).

3. Landau, L. D. & Lifshitz, E. M. *Statistical Physics, Part 2* (1980).

4. Novoselov, K. S. *et al*. Electric field in atomically thin carbon films. *Science* **306**, 666-669 (2004).

5. Campos-Delgado, J. *et al*. Bulk production of a new form of sp2 carbon: Crystalline graphene nanoribbons. *Nano Letters* **8**, 2773-2778 (2008).

6. Slonczewski, J. C. & Weiss, P. R. *Phys. Rev.* **109**, 272 (1958).

7. Morozov, S. V., Novoselov, K. S. & Geim, A. K. Electron transport in graphene. *Physics-Uspekhi* **51** (2008).

8. Castro Neto, A. H., Guinea, F., Peres, N. M. R., Novoselov, K. S. & Geim, A. K. The electronic properties of graphene. *Rev. Mod. Phys.* **81**, 109 (2009).

9. Novoselov, K. S. *et al*. *Nature* **438**, 197 (2005).

10. Allen, M. J., Tung, V. C. & Kaner, R. B. Honeycomb Carbon: A Review of Graphene. *Chem. Rev.* **110**, 132-145 (2010).

11. Geim, A. K. *Science* **324**, 1531-1534 (2009).

12. Bolotin, K. I. *et al*. Ultrahigh electron mobility in suspended graphene. *Solid State Commun* **146**, 351-355 (2008).

13. Kedzierski, J. *et al*. Graphene-on-Insulator Transistors Made Using C on Ni Chemical-Vapor Deposition. *Electron Device Letters, IEEE* **30**, 745-747 (2009).

14. Castro Neto, A. H., Guinea, F., Peres, N. M. R., Novoselov, K. S. & Geim, A. K. The electronic properties of graphene. *Rev. Mod. Phys.* **81**, 109 (2009).

15. Mkhoyan, K. A. *et al*. Atomic and Electronic Structure of Graphene-Oxide. *Nano Letters* **9**, 1058-1063 (2009).

16. Gamez-Navarro, C. *et al*. Electronic Transport Properties of Individual Chemically Reduced Graphene Oxide Sheets. *Nano Letters* **7**, 3499-3503 (2007).

17. Dideykin, A. *et al*. Monolayer graphene from graphite oxide. *Diamond and Related Materials* **20**, 105-108 (2011).

References

18. Dreyer, D. R., Park, S., Bielawski, C. W. & Ruoff, R. S. The chemistry of graphene oxide. *Chem. Soc. Rev.* **39**, 228-240 (2010).

19. Schniepp, H. C. *et al*. Functionalized Single Graphene Sheets Derived from Splitting Graphite Oxide. *The Journal of Physical Chemistry B* **110**, 8535-8539 (2006).

20. Lerf, A., He, H., Forster, M. & Klinowski, J. Structure of Graphite Oxide Revisitedâ€–. *The Journal of Physical Chemistry B* **102**, 4477-4482 (1998).

21. He, H. Y., Riedl, T., Lerf, A. & Klinowski, J. *J. Phys. Chem.* **100**, 19954 (1996).

22. Kudin, K. N., Scuseria, G. E. & Yakobson, B. I. C2F, BN, and C nanoshell elasticity from ab initio computations. *Phys. Rev. B* **64**, 235406 (2001).

23. Seol, J. H., Moore, A. L., Shi, L., Jo, I. & Yao, Z. Thermal conductivity measurement of graphene exfoliated on silicon dioxide. *Journal of Heat Transfer* **133** (2011).

24. Calizo, I., Balandin, A. A., Bao, W., Miao, F. & Lau, C. N. *Nano Lett.* **7**, 2645 (2007).

25. Balapanuru, J. *et al*. A graphene oxide-organic dye ionic complex with DNA-sensing and optical-limiting properties. *Angewandte Chemie - International Edition* **49**, 6549-6553 (2010).

26. Wang, H. *et al*. Mn3O4-graphene hybrid as a high-capacity anode material for lithium ion batteries. *J. Am. Chem. Soc.* **132**, 13978-13980 (2010).

27. Bae, S. *et al*. Roll-to-roll production of 30-inch graphene films for transparent electrodes. *Nat Nano* **5**, 574-578 (2010).

28. Hummers, W. S. & Offeman, R. E. *J. Am. Chem. Soc.* **80**, 1339 (1958).

29. Kovtyukhova, N. I. Layer-by-layer assembly of ultrathin composite films from micron-sized graphite oxide sheets and polycations. *Chemistry of Materials* **11**, 771-778 (1999).

30. Stankovich, S. *et al*. Synthesis of graphene-based nanosheets via chemical reduction of exfoliated graphite oxide. *Carbon* **45**, 1558-1565 (2007).

31. Lin, Y., Jin, J. & Song, M. Preparation and characterisation of covalent polymer functionalized graphene oxide. *J. Mater. Chem.* **21**, 3455-3461 (2011)

32. Meyer, J. C. *et al*. The structure of suspended graphene sheets. *Nature* **446**, 60-63 (2007).

33. Balandin, A. A. *et al*. Superior thermal conductivity of single-layer graphene. *Nano Letters* **8**, 902-907 (2008).

34. Cote, L. J., Kim, F. & Huang, J. Langmuirâˆ'Blodgett Assembly of Graphite Oxide Single Layers. *J. Am. Chem. Soc.* **131**, 1043-1049 (2009).

35. Zhou, X. *et al*. A method for fabrication of graphene oxide nanoribbons from graphene oxide wrinkles. *Journal of Physical Chemistry C* **113**, 19119-19122 (2009).

36. Marcano, D. C. *et al*. Improved synthesis of graphene oxide. *ACS Nano* **4**, 4806-4814 (2010).

37. Balandin, A. A., Ghosh, S., Nika, D. L. & Pokatilov, E. P. *Thermal conductivity of graphene: The first measurements and theoretical analysis* (Proceedings of the 30th International Thermal Conductivity Conference and the 18th International Thermal Expansion Symposium, Thermal Conductivity 30/Thermal Expansion 18, 2010).

38. Balandin, A. A. *et al*. Superior thermal conductivity of single-layer graphene. *Nano Letters* **8**, 902-907 (2008).

39. Novikov, D. S. Numbers of donors and acceptors from transport measurements in graphene. *Appl. Phys. Lett.* **91**, 102102 (2007).

40. Kaiser, A. B., Cristina, G. N., Sundaram, R. S., Burghard, M. & Kern, K. Electrical conduction mechanism in chemically derived graphene monolayers. *Nano Letters* **9**, 1787-1792 (2009).

41. Kaiser, A. B. & Skákalová, V. Electronic conduction in polymers, carbon nanotubes and graphene. *Chem. Soc. Rev.* **40**, 3786-3801 (2011).

42. Ohta, T., Bostwick, A., Seyller, T., Horn, K. & Rotenberg, E. Controlling the electronic structure of bilayer graphene. *Science* **313**, 951-954 (2006).

43. Brar, V. W. *et al*. *Appl. Phys. Lett.* **91**, 122102 (2007).

44. Park, S. & Ruoff, R. S. Chemical methods for the production of graphenes. *Nat Nano* **4**, 217-224 (2009).

45. GoÌ•mez-Navarro, C. *et al*. Atomic Structure of Reduced Graphene Oxide. *Nano Letters* **10**, 1144-1148 (2010).

46. Gao, W., Alemany, L. B., Ci, L. & Ajayan, P. M. New insights into the structure and reduction of graphite oxide. *Nat Chem* **1**, 403-408 (2009).

47. Kaiser, A. B., Cristina, G. N., Sundaram, R. S., Burghard, M. & Kern, K. Electrical conduction mechanism in chemically derived graphene monolayers. *Nano Letters* **9**, 1787-1792 (2009).

48. Berthing, T. *et al*. Intact mammalian cell Function on semiconductor nanowire arrays: New perspectives for cell-based biosensing. *Small* **7**, 640-647 (2011).

49. Sun, X. *et al*. Nano-Graphene Oxide for Cellular Imaging and Drug Delivery. *Nano Res.* **1**, 203-212 (2008).

50. Gruner, G. Carbon nanotube transistors for biosensing applications. *Anal. Bioanal. Chem.* **384**, 322-335 (2006).

51. Cohen-Karni, T., Qing, Q., Li, Q., Fang, Y. & Lieber, C. M. Graphene and nanowire transistors for cellular interfaces and electrical recording. *Nano Letters* **10**, 1098-1102 (2010).

52. Gao, X. P. A., Zheng, G. & Lieber, C. M. Subthreshold regime has the optimal sensitivity for nanowire FET biosensors. *Nano Letters* **10**, 547-552 (2010).

53. Suk, J. W., Piner, R. D., An, J. & Ruoff, R. S. Mechanical properties of monolayer graphene oxide. *ACS Nano* **4**, 6557-6564 (2010).

54. Hermann, G. J. & Shaw, J. M. MITOCHONDRIAL DYNAMICS IN YEAST. *Annu. Rev. Cell Dev. Biol.* **14**, 265-303 (1998).

55. Lesage, G. & Bussey, H. Cell wall assembly in Saccharomyces cerevisiae. *Microbiology and Molecular Biology Reviews* **70**, 317-343 (2006).

56. http://home.earthlink.net/~ggda/biology_of_yeast_cells_simplified.htm.

57. Liu, C. -., Lin, Y. -. & Bai, F. -. A kinetic growth model for Saccharomyces cerevisiae grown under redox potential-controlled very-high-gravity environment. *Biochem. Eng. J.* **56**, 63-68 (2011).

58. http://www.bio101.com/protocols/yeast/p-spheroplast.html.

59. Kundu, S., Maheshwari, V. & Saraf, R. F. Photolytic Metallization of Au Nanoclusters and Electrically Conducting Micrometer Long Nanostructures on a DNA Scaffold. *Langmuir* **24**, 551-555 (2008).

60. Jain, P. K., Lee, K. S., El-Sayed, I. & El-Sayed, M. Calculated Absorption and Scattering Properties of Gold Nanoparticles of Different Size, Shape, and Composition: Applications in Biological Imaging and Biomedicine. *The Journal of Physical Chemistry B* **110**, 7238-7248 (2006).

61. Maheshwari, V., Kane, J. & Saraf, R. F. Self-assembly of a micrometers-long one-dimensional network of cemented Au nanoparticles. *Adv Mater* **20**, 284-286 (2008).

References

62. Link, S. & El-Sayed, M. Size and Temperature Dependence of the Plasmon Absorption of Colloidal Gold Nanoparticles. *The Journal of Physical Chemistry B* **103**, 4212-4217 (1999).

63. Kempaiah, R., Chung, A. & Maheshwari, V. Graphene as Cellular Interface: Electromechanical Coupling with Cells. *ACS Nano* **5,** 6025-6031 (2011).

64. Guo, H., Wang, X., Qian, Q., Wang, F. & Xia, X. A Green Approach to the Synthesis of Graphene Nanosheets. *ACS Nano* **3**, 2653-2659 (2009).

65. Zhu, C., Guo, S., Fang, Y. & Dong, S. Reducing Sugar: New Functional Molecules for the Green Synthesis of Graphene Nanosheets. *ACS Nano* **4**, 2429-2437 (2010).

66. Schedin, F. *et al.* Surface-enhanced Raman spectroscopy of graphene. *ACS Nano* **4**, 5617-5626 (2010).

67. Nguyen, K. T., Abdula, D., Tsai, C. -. & Shim, M. Temperature and gate voltage dependent raman spectra of single-layer graphene. *ACS Nano* **5**, 5273-5279 (2011).

68. Nisoli, C., Lammert, P. E., Mockensturm, E. & Crespi, V. H. Carbon nanostructures as an electromechanical bicontinuum. *Phys. Rev. Lett.* **99** (2007).

69. Salvadó, Z., Arroyo-López, F. N., Barrio, E., Querol, A. & Guillamón, J. M. Quantifying the individual effects of ethanol and temperature on the fitness advantage of Saccharomyces cerevisiae. *Food Microbiol.* **28**, 1155-1161 (2011).

70. Klipp, E., Nordlander, B., Krüger, R., Gennemark, P. & Hohmann, S. Erratum: Integrative model of the response of yeast to osmotic shock (Nature Biotechnology (2005) 23 (975-982)). *Nat. Biotechnol.* **24**, 1293 (2006).

71. Dinh, T. N., Nagahisa, K., Hirasawa, T., Furusawa, C. & Shimizu, H. Adaptation of *Saccharomyces cerevisiae* Cells to High Ethanol Concentration and Changes in Fatty Acid Composition of Membrane and Cell Size. *PLoS ONE* **3**, e2623 (2008).

72. A J Gil, e. a. The formation of wrinkles in single-layer graphene sheets under nanoindentation. *Journal of Physics: Condensed Matter* **22**, 145302 (2010).

73. Kim, J., Cote, L. J., Kim, F. & Huang, J. Visualizing graphene based sheets by fluorescence quenching microscopy. *J. Am. Chem. Soc.* **132**, 260-267 (2010).

74. Wang, C. Y., Mylvaganam, K. & Zhang, L. C. Wrinkling of monolayer graphene: A study by molecular dynamics and continuum plate theory. *Physical Review B - Condensed Matter and Materials Physics* **80** (2009).

70

75. Carpenter, E. E. Iron nanoparticles as potential magnetic carriers. *J Magn Magn Mater* **225**, 17-20 (2001).

76. Tokoro, H., Fujii, S. & Oku, T. Iron nanoparticles coated with graphite nanolayers and carbon nanotubes. *Diamond and Related Materials* **13**, 1270-1273 (2004).

77. Cong, H. -., He, J. -., Lu, Y. & Yu, S. -. Water-soluble magnetic-functionalized reduced graphene oxide sheets: In situ synthesis and magnetic resonance imaging applications. *Small* **6**, 169-173 (2010).

78. Kumar, S., Ravikumar, C. & Bandyopadhyaya, R. State of dispersion of magnetic nanoparticles in an aqueous medium: Experiments and monte carlo simulation. *Langmuir* **26**, 18320-18330 (2010).
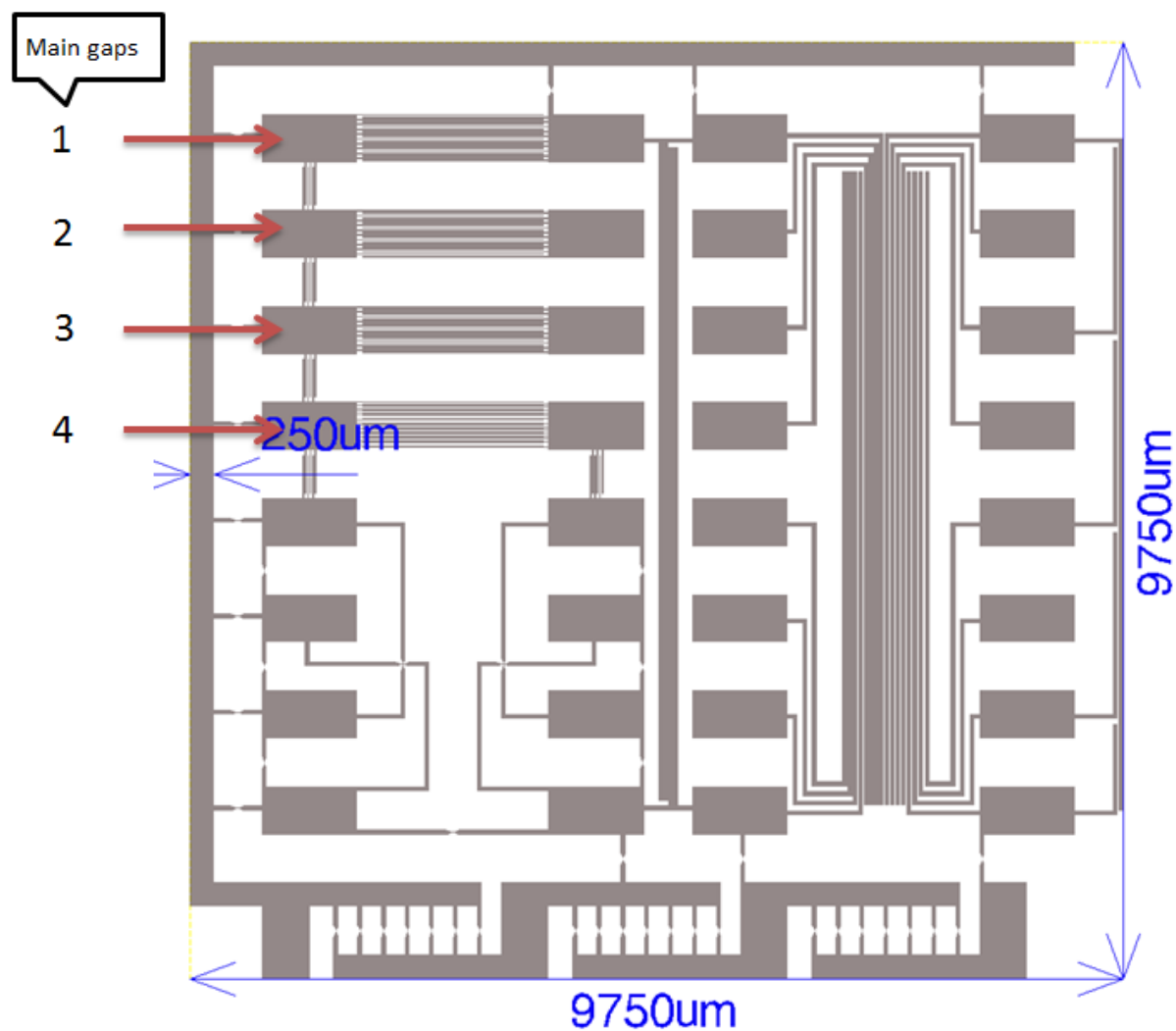
Figure 0-1: Detailed diagram of the patterned electrode chip

The grey shaded regions are made of gold and this pattern is deposited onto a silicon wafer. The primary gaps are labeled 1 to 4 on the diagram as well. The pads to the left and right have small electrodes running parallel to each other and none of them connect. This is why sheets of graphene must fill the gap between the parallel electrodes for current to show.

Appendix B
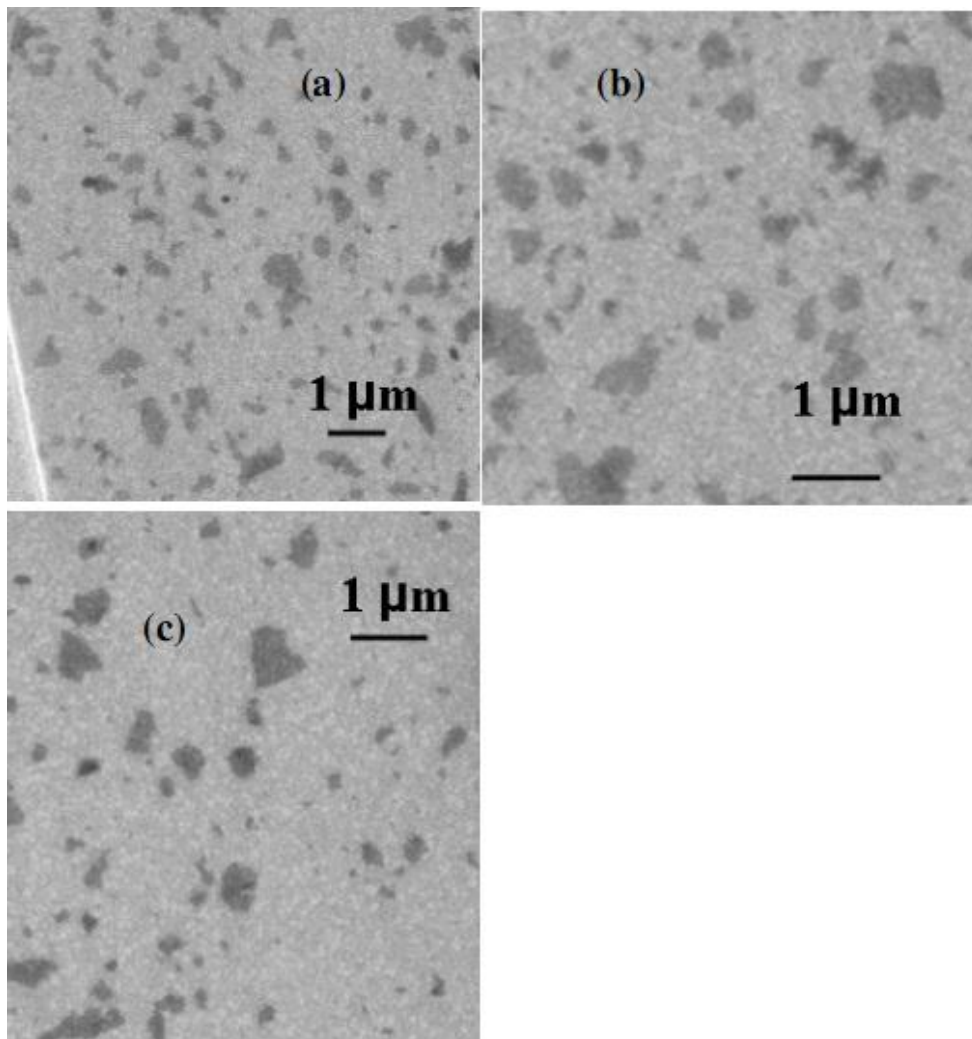
GO Sheets on Si Substrate

Figure 0-1: FESEM images of GO sheets. Images (a), (b) and (c) show that size of the GO sheets is ~ 400 - 600 nm.